Conceptual probabilistic treatment planning approaches to deal with microscopic disease as an alternative to the Clinical Target Volume

by

W.S. Niekolaas

to obtain the degree of Master of Science in Biomedical Engineering
at the Delft University of Technology,
to be defended publicly on Wednesday October 27, 2021 at 15:00 PM.

Student number:	4366085	
Project duration:	November 2020 - October 2021	
Thesis committee:	Dr. F. M. Vos,	TU Delft, chair
	Dr. Z. Perkó,	TU Delft, supervisor
	Dr. ir. D. Lathouwers,	TU Delft

An electronic version of this thesis is available at `http://repository.tudelft.nl/`.

TUDelft

Abstract

Radiotherapy is one of the main treatment modalities available to treat cancer. Radiotherapy treatment plans are created based on CT scans of the patient. In such scans the macroscopic tumor is visible, but microscopic disease present in the surrounding tissue cannot be observed. To achieve an optimal clinical outcome, both the macroscopic and the microscopic disease must be treated. Currently, the macroscopic tumor is extended by a margin into the Clinical Target Volume (CTV) to include the microscopic disease in the treated volume. The same margin is used for all patients, although the extent of microscopic disease is patient-specific and can vary largely among patients.

In this study, probabilistic treatment planning was investigated as a method to replace the margin concept. Probabilistic models were created by explicitly modeling uncertainties in the microscopic disease into an objective function used in the treatment plan optimization. By optimizing either the expected Tumor Control Probability (ETCP) or the expected Logarithmic Tumor Control Probability (ELTCP), optimal dose distributions could be obtained. Two different one-dimensional models for probabilistic treatment planning were investigated.

In the first model, the uncertainty in the extent of the microscopic disease was modeled into an objective function. This was done using a function that describes the probability of finding microscopic disease at a certain distance from the macroscopic disease. In the second model, the uncertainty in the tumor cell density in the microscopic disease area was modeled into an objective function. The uncertainty was modeled by defining the tumor cell density field as a random field and generating different realizations of the tumor cell density field using a Karhunen-Loève (KL) expansion.

For the first model, both the ETCP and the ELTCP were used as objective functions and in the second model, only the ETCP was used as an objective function. Furthermore, a penalized ETCP objective function was investigated for both models. In this penalized objective function a penalty on the dose was used to allow for controlling the balance between tumor control and sparing of normal tissue.

Using the first model, two different types of dose distributions were found. When the ETCP was optimized, the maximum dose was given to as large a volume as possible and no dose was given in the rest of the investigated volume. When the ELTCP was optimized, dose was given throughout the volume, so that the whole volume received as much dose as possible. Optimization of both objectives resulted in good tumor control. When the penalized ETCP was optimized, dose was given to a much smaller part of the volume than with the unpenalized objective, while the tumor control was still good.

Using the second model, it was shown that the KL-expansion is a promising method to model the uncertainty in tumor cell density. Different shapes of the input mean tumor cell density field were investigated. Optimizing the ETCP resulted in realistic dose distributions. Good tumor control was obtained for the different shapes of the input mean tumor cell density field. Furthermore, using the penalized ETCP, good tumor control was retained, while the dose deposited in the volume was decreased.

In conclusion, probabilistic treatment planning promises to be a good alternative to the current margin concept. It was shown that good tumor control could be achieved in the microscopic disease area using probabilistic objective functions. Both models showed promising results and the penalized objectives showed that it is possible to balance between tumor control in the microscopic disease area and sparing of normal tissue. Additional research is necessary to extend the one-dimensional KL-model into a more detailed three-dimensional model. Furthermore, the objectives need to be implemented in treatment planning systems to create real patient plans. Such studies should be performed in cooperation with clinicians and radiologists.

Preface

In this thesis, I proudly present the results of my graduation research. This thesis concludes my master program in Biomedical Engineering and thus is the last part of my studies at the Delft University of Technology. It has certainly been a journey. Graduating during the COVID-19 pandemic was tough. I thrive on daily contact with others and here I was, locked in my house without physical contact. Almost all the contact was through video meetings, but fortunately I could work at the office once a week.

I would like to thank my supervisor, Dr. Z. Perkó for all the continued support and guidance. I really appreciate your supervision and all the useful tips on how to manage such a big project and how to optimize working at home. This year has been a real learning curve for me and you provided me with a listening ear and helpful insights.

Furthermore, I would like to thank my parents for all the love and support and providing me with an alternative workplace when I needed a change of scenery. I would also like to thank my boyfriend for always being there to support me throughout the year. Together we managed to get through a tough year with covid restrictions and graduate from our masters. Finally, I would like to thank all my friends for their support, advice and listening ears throughout the year.

Contents

1

Introduction

Cancer is a disease which is characterized by tumor growth, the uncontrolled reproduction of cells to form a tumor mass. According to the National Cancer Institute, approximately 40% of men and women in the USA will be diagnosed with cancer at some point in their life [1]. Furthermore, it is still one of the major causes of death [2], with an estimated 1.93 million cancer-related deaths in Europe in 2018 [3].

Cancer is often diagnosed using imaging modalities such as computed tomography (CT) or magnetic resonance imaging (MRI). To visualize tumors with these imaging modalities, sometimes contrast fluid also needs to be injected which builds up in the tumor. The tumor then becomes visible as an enhancing mass on the scan. This visible tumor is called the macroscopic disease or the Gross Tumor Volume (GTV). It is well known that there is a possibility for the spread of tumor cells in the area surrounding the GTV [4], which is called microscopic disease. This microscopic disease consists of small groups of tumor cells that are too small to be visualized on the scans, despite technological advances [4, 5]. How far this microscopic disease can extend from the GTV into the surrounding tissue is both patient-specific and tumor-specific.

There are several treatments available to treat a patient for cancer; the main treatment modalities are surgery, radiotherapy and chemotherapy. In this work, we focus on radiotherapy, which is a treatment modality that uses high doses of radiation to kill tumor cells. Specifically, we focus on the most common form of radiotherapy, photon radiation therapy, in which x-rays are used to irradiate the cancer. Photon radiation therapy is used to treat many types of cancer throughout the body.

To obtain an optimal clinical outcome with radiotherapy, it is important that both the macroscopic and microscopic disease are irradiated sufficiently. To irradiate potential microscopic disease, a margin is applied to the GTV. This margin expands the GTV to the Clinical Target Volume (CTV), which should include both the macroscopic and the microscopic disease. The CTV is defined on patient scans with a fixed margin. Such an approach to defining the CTV, however, has downsides. As the microscopic disease is patient-specific and invisible in the patient scans, there are large uncertainties in the extent of the microscopic disease and in the tumor cell density in the tissue surrounding the GTV. Furthermore, the CTV margin is currently a binary decision. A volume either belongs to the target volume and the full dose is prescribed to it, or it does not belong to the target volume and then no dose is prescribed. Consequently, treatment planning tries to have maximum dose in the target volume and a steep drop-off in the distribution to preferably no dose outside the target volume. The uncertainties in the extent of the microscopic disease and the tumor cell density are not taken into account with such a fixed, binary margin.

Recent studies have investigated probabilistic treatment planning to replace the CTV margin. In 2018, Susharina et al. [6] introduced a probabilistic concept of the CTV, called the Clinical Target Distribution (CTD). This CTD is a three-dimensional, discrete distribution that describes the probability of voxels (a volume element in a 3D-grid) in the vicinity of the GTV to contain tumor cells. To deal with the uncertainties in the microscopic disease, this CTD can be implemented into an objective function in treatment plan optimization algorithms. Such an implementation was further investigated by Bortfeld et al. [7].

Furthermore, two other studies performed at the Medical Physics & Technology department at the Delft University of Technology [8, 9] investigated probabilistic treatment planning for microscopic disease control using a continuous probability distribution which describes the probability of finding microscopic disease at a certain distance from the GTV. This probability distribution can again be implemented into a probabilistic objective function for treatment planning.

The goal of this master project is to further investigate probabilistic treatment planning as a method to deal with the microscopic disease uncertainties. First, the probabilistic objective function derived in [8] will be studied for different tumor sites. Subsequently, a new probabilistic objective function will be derived. This objective function is based on the uncertainty in the tumor cell density field in the tissue surrounding the GTV, instead of the uncertainty in the maximum extent of the microscopic disease. The uncertainty in the microscopic disease is actually not just an uncertainty of the extent of the microscopic disease, but an uncertainty of the shape of the tumor cell density field. Basing the objective directly on the uncertainty in the tumor cell density field can thus allow for creating a more accurate model.

In Chapter 2, an introduction to radiotherapy and treatment planning is provided. In Chapter 3, probabilistic treatment planning is introduced. Subsequently, the probabilistic objective functions are derived in Chapter 4. The results of the investigated models are presented in Chapter 5. Finally, in Chapter 6 the results are discussed, and overall conclusions are presented.

2

Radiotherapy

In this chapter, radiotherapy will be introduced. First, some background information will be provided in Section 2.1. Subsequently, radiobiological models will be discussed in Section 2.2 and the clinical volumes that are used for treatment planning are discussed in Section 2.3. Finally, an introduction to treatment planning will be given in Section 2.4.

2.1. Radiotherapy

Radiotherapy is one of the main treatments for tumors. The goal of radiotherapy is to cause biological damage and subsequent cell death in the tumor cells using radiation. Radiation can be applied to the tumor area in different ways, using external beams of ionizing radiation aimed at the tumor (external radiotherapy) or by implantation of a radiation source in the vicinity of the tumor (internal radiotherapy). What type of radiation treatment a patient receives mainly depends on the location, type and size of the tumor.

Because it is important in radiotherapy to irradiate the tumor sufficiently while minimizing the damage to the healthy tissue, the effect of radiation on both tumor cells and on the healthy tissue should be known. Fractionation is used to manage the balance between tumor damage and normal tissue damage. This means that the radiation dose is administered in multiple sessions (fractions). This fractionation allows healthy tissue cells to recover from possible damage. Tumor cells can also repopulate in between fractions, but normal tissue tends to recover from radiation damage more quickly than tumor cells. Different fractionation schemes can be used [10]. In conventional external beam radiotherapy, each fraction consists of a small dose of about 1.8 to 2 Gy, so for example a prescribed total dose of 60 Gy can be spread out over 30 fractions of 2 Gy each. Other options are hyperfractionation, in which more fractions with smaller doses are administered, and hypofractionation, where the total dose is divided into fewer fractions with a higher dose. An example of hypofractionation is stereotactic body radiotherapy (SBRT).

Radiobiological models can be used to evaluate the effects of different fractionation schemes. Such models allow converting physical quantities, such as the dose and the total number of fractions, into clinically relevant quantities, such as the Biologically Effective Dose (BED), Tumor Control Probability (TCP) and the Normal Tissue Complication Probability (NTCP) [11].

2.2. Radiobiological models

Linear-Quadratic model

Cell survival can be modeled using the Linear-Quadratic (LQ) model. In the basic LQ model, the surviving fraction SF of tumor cells after receiving a single fraction of dose is:

$$SF_d = \mathrm{e}^{-(\alpha d + \beta d^2)}, \tag{2.1}$$

where α and β are parameters related to the radiation sensitivity of the cell and d is the fraction dose. The ratio α/β is determined by the sensitivity of the cells to radiation and is therefore tissue-specific.

For fractionated treatment with N_f fractions of dose d, the surviving fraction is:

$$SF_{N_f d} = (SF_d)^{N_f} \tag{2.2}$$

$$= e^{-N_f(\alpha d + \beta d^2)}. \tag{2.3}$$

The surviving fraction can then be rewritten by substituting the total dose $D = N_f d$ into Equation 2.3, leading to

$$SF_{N_f d} = e^{-(\alpha D + \beta D^2/N_f)}. \tag{2.4}$$

The relationship between the surviving fraction $SF_{N_f d}$ and the Biologically Effective Dose BED is as follows:

$$SF_{N_f d} = e^{-\alpha BED}, \tag{2.5}$$

where the BED is given by:

$$BED = D\left(1 + \frac{d}{\alpha/\beta}\right). \tag{2.6}$$

The Biologically Effective Dose BED is a measure of the biological effect that is induced in the tissue with a specific α/β ratio by the radiation.

Tumor Control Probability
The Tumor Control Probability (TCP) is the probability of local tumor control, which means that the TCP equals 1 when all tumor cells have been eradicated. The TCP is therefore dependent on the number of surviving tumor cells μ of an initial number of tumor cells N_0, which is given by

$$\mu = N_0 \cdot SF_{N_f d} = N_0 \cdot e^{-(\alpha D + \beta D^2/N_f)}. \tag{2.7}$$

The most generally used model for the TCP is based on the Poisson distribution, so the TCP for multiple fractions is described by

$$TCP = e^{-\mu} = \exp\left(-N_0 \cdot e^{-(\alpha D + \beta D^2/N_f)}\right). \tag{2.8}$$

The TCP model can be used as a measure for treatment plan optimization or for treatment plan evaluation.

Normal Tissue Complication Probability
The Normal Tissue Complication Probability (NTCP) is the probability for a certain dose to cause complications in the normal tissue. The most well-known model to predict the NTCP is the Lyman-Kutcher-Burman model [12–15]. The NTCP can also be used for treatment plan optimization or evaluation and in all treatments a balance between maximizing the TCP and minimizing the NTCP must be found.

2.3. Clinical volumes used for treatment planning
Treatment plans for radiotherapy are created based on a planning CT scan. On this CT scan, the treatment planning volumes and organs at risk (OARs) are delineated. This delineation will be used to steer the treatment plan. The treatment planning volumes are defined by ICRU Report 50 [16] as the Gross Tumor Volume (GTV), Clinical Target Volume (CTV) and Planning Target Volume (PTV). A schematic representation of these volumes is shown in Figure 2.1.

Gross Tumor Volume
The macroscopic tumor visible on the planning CT scan is delineated to obtain the Gross Tumor Volume (GTV).

Clinical Target Volume
The tumor cells are often not limited to the GTV and microscopic disease extension (MDE) is present outside the GTV. As this MDE is not visible in the planning CT scan, a Clinical Target Volume (CTV) is defined. The CTV is obtained by expanding the GTV by a margin to include microscopic disease surrounding the GTV. This margin varies per tumor site and is based on histopathological studies investigating the MDE [4, 5].
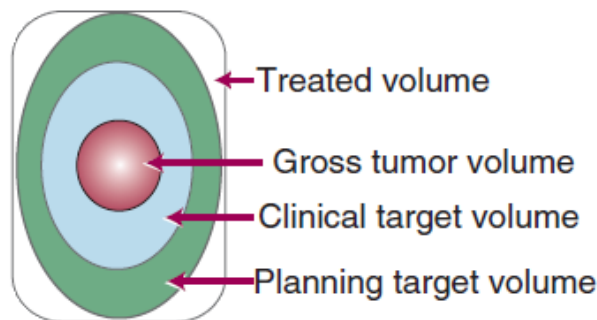
Figure 2.1: Schematic representation of the gross tumor volume, clinical tumor volume and planning target volume. Adapted from [10].

Planning Target Volume

Geometrical uncertainties in the location of the dose delivery are always present due to set-up errors. These errors consist of a systematic error and random errors. The systematic error is a fixed error, that occurs for every fraction. The random errors are variations in the location of the tumor relative to the isocenter of the treatment plan that change from day to day, for example due to organ motion and patient positioning. To deal with these errors, the CTV is extended into the Planning Target Volume (PTV) using the PTV margin. A commonly used method to define the PTV margin is the margin recipe proposed by Van Herk et al. [17]. The Planning Target Volume is the volume that needs to be treated with the prescribed dose, to ensure full dose coverage of the clinical target volume.

Organs at Risk

The Organs at Risk (OAR) should also be delineated on the planning CT. OARs are organs in the vicinity of the tumor that are at risk for radiation damage. OARs need to be taken into account during treatment planning as they are considered essential to the patient's well-being and excessive radiation to these organs must therefore be avoided.

2.4. Treatment planning

Treatment planning process

Radiotherapy treatments can only be given following an extensive treatment planning process, which consists of several steps. First, a planning CT scan is made. Using this scan, all the clinical volumes as discussed in Section 2.3 are delineated. Subsequently, a treatment plan is made. For this, a treatment planning system (TPS) is used. Such systems allow for multi-criteria optimization of the dose distribution, taking into account requirements for the dose optimization, such as the minimum required dose in the PTV and constraints on the maximum dose in OARs. The final step of the treatment planning workflow is to evaluate the treatment plan. If the plan is unsatisfactory, adjustments are made to create improved treatment plans.

Multi-criteria optimization

During multi-criteria optimization of the dose distribution, several objectives are used to create a treatment plan. An example of the objective for the PTV is the maximization of the minimum dose in the PTV. On this objective, there is typically a constraint that specifies that at least 95% of the volume needs to receive the prescribed dose. Similarly, for an OAR the objective could be to minimize the maximum dose that is administered to the OAR with a hard constraint on the maximum allowed dose in that OAR. The exact used objectives are dependent on the type of tumor and location of the tumor.

Dealing with uncertainties

As briefly discussed in Section 2.3, the GTV is expanded by two different margins to account for the different uncertainties that are present. First, the GTV is expanded into the CTV to include potential microscopic disease into the treated volume. Subsequently, the CTV is expanded into the PTV to deal with the geometrical uncertainties in the location of dose delivery.

To create the CTV, a clinician delineates the CTV on the planning CT scan, using a fixed margin that is used for all patients with the same tumor type. Such a margin is obtained from histopathological

studies that investigate the extent of microscopic disease. In addition to this fixed margin, clinicians take into account anatomical barriers when they delineate the CTV. These anatomical barriers restrain the spread of tumors and therefore clinicians can be certain that no tumor cells will be found beyond these barriers. The resulting CTV is then a volume with a margin that is the same in all directions, except when it is restricted by anatomical barriers.

The goal of the PTV is to ensure that the dose is delivered at the planned location (the CTV). For this, the margin recipe proposed by Van Herk et al. [17] is commonly used. This recipe can be used to compute the margin M based on the systematic and random errors that are present:

$$M = 2.5\Sigma + 0.7\sigma, \tag{2.9}$$

where Σ and σ are the standard deviations of the systematic and random errors, respectively. These standard deviations can be obtained from studies investigating the accuracy of radiotherapy treatments in a patient population.

3

Probabilistic treatment planning

In this chapter, probabilistic treatment planning will be discussed. First the background of probabilistic treatment planning will be discussed in Section 3.1 and subsequently it will be introduced how probabilistic treatment planning can be used for dealing with uncertainties in microscopic disease in Section 3.2.

3.1. Background

In probabilistic treatment planning, uncertainties in the target volumes are directly included into the treatment plan optimization, thereby replacing the explicit target volume margin [18]. This means that for the uncertainties in the microscopic disease area, the Clinical Target Volume (CTV) margin would be replaced by optimizing the dose distribution in the microscopic disease area while taking into account the uncertainties present in this area. For the geometrical uncertainties, the Planning Target Volume (PTV) margin would be replaced by optimizing the dose distribution while taking the geometrical uncertainties in the location of the dose delivery into account.

3.1.1. Probabilistic treatment planning to replace CTV-PTV margin

To familiarize with the concept of how probabilistic treatment planning can be used for photon radiotherapy, a few studies investigating probabilistic treatment planning to replace the CTV-PTV margin will be discussed here. Probabilistic treatment planning offers an alternative to the traditional CTV-PTV margin based on the margin recipe [17], by allowing the explicit implementation of the geometrical uncertainties into the treatment plan optimization.

In 2007, Witte et al. [19] introduced a probabilistic planning method where the geometrical uncertainties were incorporated into the TCP and NTCP cost functions of the treatment planning. Both systematic and random errors were implemented into the cost functions by shifting the target volume with respect to the dose distribution and blurring of the dose distribution, respectively. The expected TCP was derived by assuming a three-dimensional Gaussian distribution for both the systematic and random errors. The expected NTCP was derived in a similar manner. The treatment plan was then optimized for the expected TCP and NTCP functions. It was shown that the probabilistic treatment plan resulted in a better balance between the expected TCP and the expected NTCP than a conventional margin-based treatment plan.

Bohoslavsky et al. [20] improved on the probabilistic planning method from Witte et al. [19] by introducing rotational uncertainties. Witte et al. only took into account translational uncertainties for the systematic error by shifting the target volume with respect to the dose distribution. Bohoslavsky et al. implemented the rotational uncertainties by rotating the target volume around all three axes at regular angular intervals. Again, the treatment plans were optimized for the expected TCP and NTCP, and it was shown that the probabilistic treatment plans achieved better dose distributions regarding the expected TCP and NTCP than conventional margin-based treatment plans.

Tilly et al. [21] investigated a different probabilistic approach to replace the CTV-PTV margin. They implemented the geometrical uncertainties into a cost function that optimizes for a percentile dosage. This percentile dosage is defined as the probability for a prescribed dose coverage, which is in turn

the minimum dose that a partial volume in a region of interest must receive. In this study only systematic errors were implemented. These systematic errors were modelled by generating randomly displaced geometrical states of the patient anatomy using statistical shape models and calculating the dose distributions for both the original patient anatomy and the different randomized geometrical states. The expected percentile dosage was derived from these dose distributions and treatment plans were optimized using the expected percentile dosage as a constraint. This constraint was set such that for 90% of the randomized geometrical states 98% of the target volume received the minimum dose determined by the prescribed dose coverage. The probabilistic treatment plans were compared to conventional margin-based treatment plans. It was shown that the probabilistic plans showed an increase in the dose in the CTV and a decrease in the dose in nearby OARs, compared to the conventional plans.

In these studies on probabilistic treatment planning to replace the CTV-PTV margin, the geometrical uncertainties were incorporated into a cost function that can be implemented in a treatment planning system. Subsequently, expected value optimization for the TCP and NTCP or percentile dosage was used.

3.1.2. Probabilistic treatment planning for proton therapy

Although the focus of this work is on photon radiotherapy, a short discussion of probabilistic treatment planning for proton therapy is included here. For proton therapy, the same uncertainties as for photon therapy are present, but additionally there are some proton therapy specific challenges. Proton therapy allows for a much more localized dose deposition than photon therapy due to the finite range of protons. There are however uncertainties in the exact location the protons will be deposited in the patient, mainly because CT images are not an ideal input for the proton dose calculations. Furthermore, the impact of setup errors and organ motion on the dose deposition is bigger in proton therapy than it is in photon therapy, this is again related to the finite range of protons and the resulting the localized dose deposition. As small displacements can lead to an entirely different (and incorrect) dose distribution than was planned, probabilistic treatment planning can be especially helpful for proton therapy, to deal with both the conventional geometrical uncertainties and the additional proton therapy specific uncertainties.

3.2. Probabilistic treatment planning to replace GTV-CTV margin

The goal of using probabilistic treatment planning to replace the GTV-CTV margin is to achieve an optimal dose distribution for tumor control in the CTV while taking the uncertainties in the microscopic disease into account. In order to do this, a probabilistic model based on the probability of finding microscopic disease at a certain distance needs to be created. As shortly discussed in Chapter 1, a few studies investigating such models have been performed before.

3.2.1. Previous studies

Susharina et al. [6] introduced a probabilistic concept of the CTV, called the Clinical Target Distribution (CTD). This CTD is a three-dimensional discrete distribution that contains the probability p_i at voxel i that this voxel contains tumor cells. These voxel probabilities range from 1 (near the GTV) to 0 (far away from the GTV). This is in stark contrast with how the CTV works where the binary decision of including voxels into the CTV or not results in voxel i having a probability of either 1 or 0. To construct the CTD, the authors proposed that a physician draws a number of margins around the GTV and assigns a probability to each margin that tumor can be found outside this margin (at distances further from the GTV). This distribution can be used to compute the probability p_i, which can be used in an objective function. In this study, the quadratic underdose penalty (which penalizes underdosage in the target volume) was used as the objective function. Bortfeld et al. [7] further investigated the use of this CTD for probabilistic definition of the CTV. In this study, the margins with assigned probabilities are replaced by volume shells which are prescribed a probability of being tumorous. Furthermore, the quadratic underdose objective function is replaced by an objective function based on the TCP. This objective function is used to maximize the tumor control within the volume shells while taking the probability of the shells to be tumorous into account.

Both these studies showed promising results for the use of probabilistic treatment planning to replace the GTV-CTV margin. However, neither study provides a manner of deriving the CTD other than having physicians manually delineate the margins or volume shells and assigning probabilities

to these structures. To improve on the CTD concept, Briggeman [8] therefore introduced a simplified one-dimensional model based on the expected TCP. This model includes the uncertainties in the microscopic disease area using probability density functions for the maximum distance where MDE can be found and the quantity of the tumor cell density. By maximizing the expected TCP, dose distributions can be obtained that maximize the tumor control by taking the uncertainties in the microscopic disease into account. A three-dimensional extension of this model was investigated by Swart [9], where the location of a number of small groups of microscopic disease is modelled using stochastic variables.

3.2.2. Introduction of the investigated models

For probabilistic treatment planning, we need an objective function that maximizes tumor control by optimizing the dose distribution in the uncertain microscopic disease area. The Tumor Control Probability (as introduced in Section 2.2) is used to compute the probability of local tumor control and is thus suitable as a basis for our objective function:

$$TCP = \exp\left[-N_0 \cdot \exp\left(-\left(\alpha D + \frac{\beta D^2}{N_f}\right)\right)\right]. \tag{3.1}$$

Here, N_0 is the initial number of tumor cells, α and β are the radiosensitivity parameters of the tumor tissue and N_f is the number of treatment fractions. The initial number of tumor cells equals $N_0 = \rho \cdot V_{tumor}$, where ρ is the tumor cell density and V_{tumor} the tumor volume. As we desire to optimize the spatial dose distribution in the CTV, the dose D is replaced by a spatially dependent dose distribution $D(\mathbf{r})$. An integral over the entire volume can then be used to obtain the TCP for a tumor with a spatially dependent tumor cell density $\rho(\mathbf{r})$ that receives a dose $D(\mathbf{r})$:

$$TCP(D, \rho) = \exp\left[-\int_V \rho(\mathbf{r}) \exp\left(-\left(\alpha D(\mathbf{r}) + \frac{\beta D(\mathbf{r})^2}{N_f}\right)\right) d\mathbf{r}^3\right]. \tag{3.2}$$

An alternative to the TCP is the logarithmic Tumor Control Probability (LTCP), which is computationally more efficient than the TCP,

$$LTCP(D, \rho) = -\int_V \rho(\mathbf{r}) \exp\left(-\left(\alpha D(\mathbf{r}) + \frac{\beta D(\mathbf{r})^2}{N_f}\right)\right) d\mathbf{r}^3. \tag{3.3}$$

The goal of optimizing the TCP is to obtain the highest possible tumor control in the volume, whereas the goal of optimizing the LTCP would be to avoid underdosing any part of the volume. Whenever any part of the volume receives a too low dose, the LTCP becomes very large. This drives the optimizer to avoid any cases of underdosage.

The uncertainties in the microscopic disease area are essentially uncertainties in the tumor cell density field $\rho(\mathrm{r})$: both the extension of the tumor cell density field from the gross tumor volume and the quantity of the tumor cell density are uncertain. In this thesis, two different models of the uncertainty in the microscopic disease are investigated.

First, we will further investigate the model that was introduced by Briggeman [8], where the uncertainties in the microscopic disease area are defined using probability density functions. A probability density function is needed for both the microscopic disease extension and the value of the tumor cell density. A probability density function for the MDE describes the probability of finding microscopic disease at a certain distance from the GTV. Such a function can be obtained from histopathologic studies that investigate the maximum MDE from a tumor (see Appendix A). Beyond the maximum MDE, the tumor cell density will be 0, so the spatial distribution of the tumor cell density $\rho(\mathbf{r})$ is dependent on the maximum MDE and therefore on the uncertainty of the MDE. Additionally, the value of the tumor cell density is uncertain, so a probability density function for the tumor cell density needs to be defined as well. It is assumed that the quantity of ρ is uniformly distributed among patients. This model will be derived in Section 4.1.

Subsequently, a model will be investigated that models the tumor cell density field explicitly. Such a model makes sense as the uncertainty in the microscopic disease area is essentially just an uncertainty of the actual tumor cell density field in this area. For this model, a Karhunen-Loève (KL) expansion is used to generate different realizations of the tumor cell density field to simulate different patients. The Karhunen-Loève expansion is a method which can be used to parameterize a random field into a

linear combination of functions that describes the variation in the random field. To create this model, we need to define the mean tumor cell density in the area and a correlation function that describes the correlation of the tumor cell density. The KL-model is presented in Section 4.6.

$$4$$

Models

In this chapter, the different models that are investigated for probabilistic treatment planning to account for uncertainties in the CTV are introduced. Section 4.1 shows the derivation of two objective functions, based on the expected TCP and expected LTCP (logarithmic TCP), in Section 4.2 these objective functions are discretized and in Section 4.3 a penalized version of the objective function based on the ETCP is derived. In Section 4.4, the optimization constraints are described and the tumor and model parameters used are detailed in Section 4.5. Finally, in Section 4.6 a Karhunen-Loève model is introduced in which the tumor cell density field is parameterized using a Karhunen-Loève expansion, which is then used to derive an objective function based on this KL expansion.

4.1. Derivation of the objective function

For the probabilistic optimization, we assume a symmetric, spherical tumor with a radius R and a spherical CTV shell of thickness Δ surrounding the tumor. This geometry is visualized in Figure 4.1.
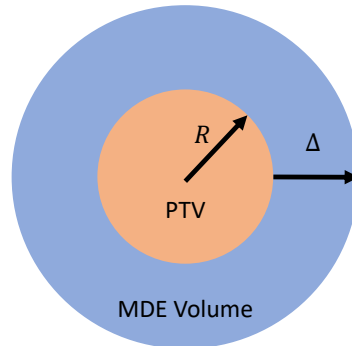
Figure 4.1: Conceptual geometry for a symmetric, spherical tumor with radius R, surrounded by a spherical CTV shell with a thickness Δ. Adapted from [8]

Due to the assumption of a symmetric, spherical tumor geometry, the volume integral in the TCP (Equation 3.2) can be replaced by an integral over r from the tumor radius R up to $R + \Delta$. The TCP is then as follows:

$$TCP(D, \rho) = \exp\left[-\int_R^{R+\Delta} \rho(\mathrm{r}) \cdot 4\pi r^2 \cdot \exp\left(-\left(\alpha D(\mathrm{r}) + \frac{\beta D(\mathrm{r})^2}{N_f}\right)\right) \mathrm{dr}\right]. \qquad (4.1)$$

The same can be done for the volume integral in the LTCP (Equation 3.3):

$$LTCP(D, \rho) = \log(TCP(D, \rho)) = -\int_R^{R+\Delta} \rho(\mathrm{r}) \cdot 4\pi r^2 \cdot \exp\left(-\left(\alpha D(\mathrm{r}) + \frac{\beta D(\mathrm{r})^2}{N_f}\right)\right) \mathrm{dr}. \qquad (4.2)$$

The uncertainty in the CTV is actually an uncertainty in how far the tumor cell density field $\rho(\mathrm{r})$ extends from the GTV and an uncertainty in the value of the tumor cell density. We assume that the tumor cell

density within the CTV shell is constant and drops to 0 after a distance Δ:

$$\rho(r, \Delta) = \rho \cdot H(R + \Delta - r), \tag{4.3}$$

where H is the Heaviside function and $r > R$ as only the CTV is investigated. The uncertainty in the extent of CTV volume is in the thickness of the CTV Δ, so we need a probability density function $P_\Delta(\Delta)$. $P_\Delta(\Delta)$ is derived from a cumulative distribution function $F_\Delta(\Delta)$:

$$F_\Delta(\Delta) = 1 - e^{-\frac{\Delta}{L}}, \tag{4.4}$$

where L is a constant that is obtained by fitting this exponential function to data on the maximum MDE obtained from histopathologic studies (Appendix A). The corresponding probability density function $P_\Delta(\Delta)$ is:

$$P_\Delta(\Delta) = \frac{1}{L} e^{-\frac{\Delta}{L}}. \tag{4.5}$$

The corresponding maximum MDE distance Δ_{max} can be computed from L. We assume that Δ_{max} corresponds to a probability level of $p = 0.99$:

$$p = 1 - e^{-\frac{\Delta_{max}}{L}} = 0.99. \tag{4.6}$$

We take 0.99 as the probability level as clinically it is impossible to irradiate the entire body of the patient, so it is assumed that 99% of all tumor cells is within the investigated volume. Δ_{max} can then be computed as follows:

$$\Delta_{max} = -L \cdot log(1 - p). \tag{4.7}$$

To account for the uncertainty in the value of the tumor cell density, we assume that the tumor cell density is uniformly distributed among patients, which gives a probability density function $P_\rho(\rho)$:

$$P_\rho(\rho) = \frac{1}{\rho_1 - \rho_0}, \tag{4.8}$$

where ρ_0 is the minimum tumor cell density and ρ_1 the maximum tumor cell density.

To account for the uncertainties, we will optimize either the expected value of the TCP:

$$
\begin{aligned}
\mathbb{E}(TCP(D, \rho)) &= \int_{\rho_0}^{\rho_1} \int_0^\infty TCP(D, \rho) P_\rho(\rho) P_\Delta(\Delta) d\Delta d\rho \\
&= \int_{\rho_0}^{\rho_1} \int_0^\infty \exp\left[-\int_R^{R+\Delta} \rho(r) \cdot 4\pi r^2 \cdot \exp\left(-\left(\alpha D(r) + \frac{\beta D(r)^2}{N_f} \right) \right) dr \right] P_\rho(\rho) P_\Delta(\Delta) \, d\Delta \, d\rho,
\end{aligned}
\tag{4.9}
$$

or the expected value of the LTCP

$$
\begin{aligned}
\mathbb{E}(LTCP(D, \rho)) &= \int_{\rho_0}^{\rho_1} \int_0^\infty LTCP(D, \rho) P_\rho(\rho) P_\Delta(\Delta) d\Delta d\rho \\
&= \int_{\rho_0}^{\rho_1} \int_0^\infty -\int_R^{R+\Delta} \rho(r) \cdot 4\pi r^2 \cdot \exp\left(-\left(\alpha D(r) + \frac{\beta D(r)^2}{N_f} \right) \right) dr \, P_\rho(\rho) P_\Delta(\Delta) \, d\Delta \, d\rho.
\end{aligned}
\tag{4.10}
$$

4.2. Discretization

To implement Equation 4.9 and Equation 4.10 as objective functions, they need to be discretized. The integrals for the probability density functions can be approximated using quadrature rules. To integrate over Δ, a Gauss-Laguerre quadrature is applied with N_{quad} points at Δ_j with corresponding weights w_j^Δ. The integral over $\rho(r)$ is approximated using a Gauss-Legendre quadrature with N_{quad} points at ρ_i with corresponding weights w_i^ρ. The exact implementation of the quadratures can be found in Appendix C. Additionally, the spatial integral is approximated by discretizing the radius into radii r_s, $s = 1, ..., S + 1$ such that the investigated volume is divided into S concentric spherical shells of equal volume. Shells

of equal volume are chosen to avoid the outer shells of the volume containing larger numbers of tumor cells than the inner shells. The maximum distance r_{s+1} is set equal to $R + 2 \cdot \Delta_{max}$. We assume that the dose within a shell is a constant D_s. This leads to the following discretizations of the $\mathbb{E}(TCP(D,\rho))$ and $\mathbb{E}(LTCP(D,\rho))$:

$$ETCP(D) = \sum_{i=1}^{N_{quad}} \sum_{j=1}^{N_{quad}} w_i^\rho w_j^\Delta \exp\left[-\sum_{s:r_s<R+\Delta_j} \rho_i V_{s,j} \exp\left(-\left(\alpha D_s + \frac{\beta D_s^2}{N_f}\right)\right) \right] \qquad (4.11)$$

$$ELTCP(D) = -\sum_{i=1}^{N_{quad}} \sum_{j=1}^{N_{quad}} w_i^\rho w_j^\Delta \sum_{s:r_s<R+\Delta_j} \rho_i V_{s,j} \exp\left(-\left(\alpha D_s + \frac{\beta D_s^2}{N_f}\right)\right), \qquad (4.12)$$

where $V_{s,j}$ is the volume of the shells, which is dependent on Δ_j. As the sum over the volumes should only go up to Δ_j, the volume of the shell that contains Δ_j (with $r_s < R + \Delta_j$ and $r_{s+1} > R + \Delta_j$) needs to be modified, as it only partially contains tumor cells. The volumes of the shells are computed as follows:

$$V_{s,j} = \begin{cases} 0 & \text{if } r_s > R + \Delta_j \\ 4/3\pi \left(r_{s+1}^3 - r_s^3\right) & \text{if } r_{s+1} < R + \Delta_j \\ 4/3\pi \left((R + \Delta_j)^3 - r_s^3\right) & \text{if } r_s < R + \Delta_j \text{ and } r_{s+1} > R + \Delta_j. \end{cases} \qquad (4.13)$$

For the optimization, the gradient and Hessian of the objective functions are necessary. Both can be analytically calculated and thus implemented into the optimization. The gradient and Hessian of the $ETCP(D)$ are:

$$\frac{dETCP(D)}{dD_l} = \sum_{i=1}^{N_{quad}} \sum_{j=1}^{N_{quad}} w_i^\rho w_j^\Delta \exp\left[-\sum_{s:r_s<R+\Delta_j} \rho_i V_{s,j} \exp\left(-\left(\alpha D_s + \frac{\beta D_s^2}{N_f}\right)\right) \right] \cdot$$
$$\left[\rho_i V_{l,j} \exp\left(-\left(\alpha D_l + \frac{\beta D_l^2}{N_f}\right)\right) \right] \cdot \left(\alpha + \frac{2\beta D_l}{N_f}\right) \qquad (4.14)$$

and

$$\frac{d^2 ETCP(D)}{dD_l \, dD_m} = \sum_{i=1}^{N_{quad}} \sum_{j=1}^{N_{quad}} w_i^\rho w_j^\Delta \exp\left[-\sum_{s:r_s<R+\Delta_j} \rho_i V_{s,j} \exp\left(-\left(\alpha D_s + \frac{\beta D_s^2}{N_f}\right)\right) \right] \cdot$$
$$\left\{ \left[\rho_i V_{l,j} \exp\left(-\left(\alpha D_l + \frac{\beta D_l^2}{N_f}\right)\right) \right] \cdot \left(\alpha + \frac{2\beta D_l}{N_f}\right) \left[\rho_i V_{m,j} \exp\left(-\left(\alpha D_m + \frac{\beta D_m^2}{N_f}\right)\right) \right] \cdot \left(\alpha + \frac{2\beta D_m}{N_f}\right) + \right.$$
$$\left. \delta_{l,m} \left[\rho_i V_{l,j} \exp\left(-\left(\alpha D_l + \frac{\beta D_l^2}{N_f}\right)\right) \right] \left[-\left(\alpha + \frac{2\beta D_l}{N_f}\right)^2 + \frac{2\beta}{N_f} \right] \right\}, \qquad (4.15)$$

where δ_l, m is the Kronecker delta. The gradient and the Hessian of the $ELTCP(D)$ are:

$$\frac{dELTCP(D)}{dD_l} = -\sum_{i=1}^{N_{quad}} \sum_{j=1}^{N_{quad}} w_i^\rho w_j^\Delta \rho_i V_{l,j} \exp\left(-\left(\alpha D_l + \frac{\beta D_l^2}{N_f}\right)\right) \cdot \left[-\left(\alpha + \frac{2\beta D_l}{N_f}\right) \right] \qquad (4.16)$$

and

$$\frac{d^2 ELTCP(D)}{dD_l \, dD_m} = -\sum_{i=1}^{N_{quad}} \sum_{j=1}^{N_{quad}} w_i^\rho w_j^\Delta \delta_{l,m} \rho_i V_{l,j} \exp\left(-\left(\alpha D_l + \frac{\beta D_l^2}{N_f}\right)\right) \left[\left(\alpha + \frac{2\beta D_l}{N_f}\right)^2 - \frac{2\beta}{N_f} \right]. \qquad (4.17)$$

4.3. Derivation of penalized objective

The basic ETCP model takes only the maximization of the tumor control into account. To allow for a better balance between the TCP of a treatment plan and the organ dosage of healthy tissue, a penalized objective could be used. An example of a simple penalty that can be imposed on the ETCP, is the normalized squared overdose d_{norm}^+:

$$d_{norm}^+ = \frac{\int_V D(\mathrm{r})^2 \, \mathrm{d}\mathrm{r}}{\int_V D_{max}^2 \, \mathrm{d}\mathrm{r}}. \tag{4.18}$$

Just like the ETCP, d_{norm}^+ has a value between 0 and 1 and can therefore be used to create a new objective $\mathrm{pen\_obj} = \mathbb{E}(TCP(D, \rho)) - d_{norm}^+$ in which the ETCP is penalized for a too high integral dosage in the volume. A weight $w_{pen} \in [0, 2]$ can be used to balance the influence of the ETCP and the penalty on the optimization. The interval $[0, 2]$ is chosen, so a weight of 1 corresponds to an equal balance between the ETCP and the penalty, a weight of 0 corresponds to optimizing only the ETCP and a weight of 2 corresponds to optimizing only the penalty. The resulting penalized model is

$$\mathrm{pen\_obj} = (2 - w_{pen}) \cdot \mathbb{E}(TCP(D, \rho)) - w_{pen} \cdot \frac{\int_V D(r)^2 \, \mathrm{d}\mathrm{r}}{\int_V D_{max}^2 \, \mathrm{d}\mathrm{r}} \tag{4.19}$$

and by applying the same spatial discretization as was used for the $ETCP(D)$, we obtain the discretized penalized model,

$$\mathrm{pen\_obj} = (2 - w_{pen}) \cdot ETCP(D) - w_{pen} \cdot \frac{\sum_s D_s^2 \cdot V_s}{\sum_s D_{max}^2 \cdot V_s}, \tag{4.20}$$

where $V_s = 4/3\pi \left(\mathrm{r}_{s+1}^3 - \mathrm{r}_s^3 \right)$.

For the optimization, the gradient and Hessian are also required. The gradient is given by

$$\frac{\mathrm{d}(\mathrm{pen\_obj})}{\mathrm{d}D_l} = (2 - w_{pen}) \cdot \frac{\mathrm{d}ETCP(D)}{\mathrm{d}D_l} - w_{pen} \cdot \frac{2D_l \cdot V_l}{\sum_s D_{max}^2 \cdot V_s} \tag{4.21}$$

and the Hessian is given by

$$\frac{\mathrm{d}^2(\mathrm{pen\_obj})}{\mathrm{d}D_l \, \mathrm{d}D_m} = (2 - w_{pen}) \cdot \frac{\mathrm{d}^2 ETCP(D)}{\mathrm{d}D_l \, \mathrm{d}D_m} - \delta_{l,m} \cdot w_{pen} \cdot \frac{2V_l}{\sum_s D_{max}^2 \cdot V_s}. \tag{4.22}$$

4.4. Optimization settings

The objectives are maximized in Python, using the trust-constr method of the SciPy optimize.minimize function [22] which uses a trust region algorithm which is well suited for solving non-linear constrained optimization problems.

Two constraints are used for the optimization of the dose distribution. First, a bound constraint $0 \leq D_s \leq D_{max}$ is set on the dose, to ensure that the dose in the shells cannot be negative and does not exceed a maximum dose D_{max}. Secondly, a linear total energy constraint

$$\sum_s V_s D_s \leq C \sum_s V_s D_{max} \tag{4.23}$$

is imposed on the optimization. C is a constant, which can be varied to take any value between 0 and 1. The total energy constraint ensures that the integral dose deposited in the volume is constrained. Without such a constraint, the optimization would result in maximum dose throughout the investigated volume.

Furthermore, a scaling factor scale_fac can be provided to the optimization, which scales the objective, gradient and Hessian as follows:

$$\mathrm{scaled \ objective} = \mathrm{scale\_fac} \cdot \mathrm{obj},$$

$$\mathrm{scaled \ gradient} = \mathrm{scale\_fac} \cdot \frac{\mathrm{d}(\mathrm{obj})}{\mathrm{d}D_l},$$

$$\mathrm{scaled \ Hessian} = \mathrm{scale\_fac} \cdot \frac{\mathrm{d}^2(\mathrm{obj})}{\mathrm{d}D_l \, \mathrm{d}D_m}.$$

Instead of the original functions, these scaled functions are provided to the optimizer. As the TCP is a sigmoidal function, the gradient values in dose areas where the TCP is almost 0 or almost 1 can approach 0, which would prevent the optimization from further optimizing the dose values in these dose areas. By using the scaled functions, the gradient values do not approach 0 as quickly and thus the optimization can be pushed further towards the optimum.

4.5. Tumor and model parameters

4.5.1. Parameters for Section 5.1: Comparison to previous results

The first section of the results will focus on comparing the current model to previous results from Briggeman [8]. For this, parameters similar to the ones used in that study will be used. The tumor site of interest is prostate and the tumor and model parameters can be found in Table 4.1.

Table 4.1: Tumor and model parameters for the comparison to previous results.

Parameter	Value
Tumor radius R (mm)	3
Constant L (mm)	[1.1, 1.7, 2.6]
Max. CTV thickness Δ_{max} (mm)	[5.0, 8.0, 12.0]
Maximum dose D_{max} (Gy)	38.0
Number of treatment fractions N_f	4
α (Gy^{-1})	0.15
β (Gy^{-2})	0.103
Minimum tumor cell density ρ_0 (mm^{-3})	1×10^2
Maximum tumor cell density ρ_1 (mm^{-3})	4×10^5
Energy constant C	0.5
Number of shells S	150
Number of quadrature points N_{quad}	50

4.5.2. Parameters for Section 5.2: Different tumor sites

The second part of the results will focus on the use both the ETCP/ELTCP (Section 4.2) and penalized ETCP (Section 4.3) as objectives to optimize dose distributions for the CTV for four tumor sites; brain, breast, lung and prostate. An overview of all the used parameters is tabulated in Table 4.2. In Appendix B, the determination of constant L and corresponding Δ_{max} by fitting Equation 4.4 to cumulative data obtained from histopathologic studies on the extension of microscopic disease (Appendix A) are demonstrated. For all tumor sites, the maximum tumor cell density ρ_1 is obtained from literature and the minimum tumor cell density ρ_0 is assumed to be significantly lower than ρ_1 as the tumor cell density is expected to be lower in the CTV than in the tumor [23].

Brain parameters

The average tumor volume for brain tumors is 44 cm^3 [24]. As a spherical tumor geometry is assumed, the tumor radius R is set to 22 mm. The used treatment scheme gives a maximum dose of 74.8 Gy in 34 fractions. This number of fractions N_f and maximum dose D_{max} are proposed by Pedicini et al. [25] as a treatment scheme that yielded a much higher TCP (≈ 0.85) than conventional schemes (≈ 0.3) in their study. Furthermore, the estimate of α, β and maximum tumor cell density ρ_1 are also obtained from Pedicini et al. [25]. The values are 0.12 Gy^{-1}, 0.015 Gy^{-2} and 2×10^{-1} mm^{-3}, respectively. Due to the large Δ_{max}, the investigated volume is quite large. The investigated volume is therefore divided into 300 volume shells. The large volume also means that a relatively high energy constraint constant C of 0.8 is necessary to allow enough dose for tumor control. This was determined by increasing the constant from 0.5 in steps of 0.1, until high tumor control probabilities were obtained.

Breast parameters

We focus on breast tumors that are treated with a radiation boost after breast conserving therapy (BCT) was performed. These are the types of tumors for which the histopathologic MDE data was examined in Appendix A. A tumor radius of 10 mm is assumed, based on findings from such histopathologic

Table 4.2: Tumor and model parameters for the four tumor sites

Parameter	Brain	Breast	Lung	Prostate
Tumor radius R (mm)	22	10	22	30
Constant L (mm)	17.4	17.2	6.15	1.75
Max. CTV thickness Δ_{max} (mm)	80.2	79.2	28.3	8.04
Maximum dose D_{max} (Gy)	74.8	50.0	54.0	60.0
Number of treatment fractions N_f	34	25	3	4
α (Gy^{-1})	0.12	0.30	0.70	0.15
β (Gy^{-2})	0.015	0.030	0.05	0.058
Minimum tumor cell density ρ_0 (mm^{-3})	1×10^{-4}	1×10^{-1}	1×10^1	1×10^{-1}
Maximum tumor cell density ρ_1 (mm^{-3})	2×10^{-1}	1×10^2	1×10^4	4×10^2
Energy constant C	0.8	0.8	0.3	0.5
Number of shells S	300	300	225	150
Number of quadrature points N_{quad}	50	50	50	50
Objective scaling factor $scale\_fac$	1×10^6	1×10^6	1×10^6	1×10^6

studies [26, 27]. A fractionation scheme of 25 fractions to administer a maximum of 50.0 Gy is assumed [28]. The used tumor parameters $\alpha = 0.30$ Gy^{-1} and $\beta = 0.030$ Gy^{-2} are taken from Guerrero et al. [29]. No studies were found where a tumor cell density was reported for breast tumors, so a maximum tumor cell density of 1×10^2 mm^{-3} was chosen as it yields a realistic tumor control probability together with α and β. Just as for brain tumors, the Δ_{max} is large, so the number of volume shells S is set to 300 and an energy constraint constant C of 0.8 is used.

Lung parameters
For lung tumors, we focus on tumors that are treated with Stereotactic Body Radiation Therapy (SBRT) as the MDE data in Appendix A is also focused on such tumors. A typical tumor size is 45 cm^3 [30], which corresponds to a tumor radius R of 22 mm. A fractionation scheme of 3 fractions for a maximum of 54.0 Gy is used [31]. The values for α, β and ρ_1 are 0.70 Gy^{-1}, 0.05 Gy^{-2} and 1×10^4 mm^{-3}, respectively and are taken from the study by Alaswad et al. [30]. The number of volume shells S is set to 225 as Δ_{max} is smaller than for brain and breast tumors. An energy constraint constant C of 0.3 is applied as it was found that sufficient tumor control could be achieved with this value of the constant.

Prostate parameters
For treatment of prostate tumors, the whole prostate is irradiated, as prostate tumors are often multifocal with a primary tumor and secondary satellite lesions [32]. The typical volume of an entire prostate is about 25 cm^3 [33], which corresponds to a tumor radius of 30 mm for a spherical tumor. The used treatment scheme is a maximum dose D_{max} of 60.0 Gy given in 4 fractions [34]. The used tumor parameters are taken from a study by Pedicini et al. [34] and are 0.15 Gy^{-1}, 0.058 Gy^{-2} and 4×10^2 mm^{-3} for α, β and ρ_1, respectively. Finally, the number of volume shells S is set to 150, as Δ_{max} for prostate is the smallest among the four tumor sites and an energy constraint constant C of 0.5 is used.

4.6. Karhunen-Loève expansion to describe tumor density field

4.6.1. Random field parametrization

For the Karhunen-Loève expansion method, we assume that the uncertainty of the CTV is the tumor cell density field. We define the tumor cell density as a random field $\rho(r, \theta)$, where $r \in D, D \subset \mathbb{R}$ the radii that define the volume for which we want to optimize the dose distribution (the CTV surrounding the GTV) and $\theta \in \Theta$ a random event belonging to the sample space Θ. We assume the tumor cell density field $\rho(r, \theta)$ to be a Gaussian random field, with a mean $\mu^\rho(r)$ and a standard deviation $\sigma^\rho(r)$. Furthermore, we assume a Gaussian autocorrelation coefficient function of

$$\text{corr}_{\rho\rho}(|r - r'|) = \exp\left[-\left(\frac{|r - r'|}{b}\right)^2\right], \tag{4.24}$$

where b is the correlation length and $|r - r'|$ is the distance between r and r'. The autocovariance kernel is then defined by

$$\text{Cov}_{\rho\rho}(r, r') = \sigma^\rho(r)\sigma^\rho(r') \exp\left[-\left(\frac{|r - r'|}{b}\right)^2\right]. \tag{4.25}$$

We use a Karhunen-Loève expansion (KL expansion) to approximate $\rho(r, \theta)$. A Karhunen-Loève expansion is a series expansion method that can be used to represent a random field as follows:

$$H(r, \theta) = \mu(r) + \sum_{i=1}^{\infty} \sqrt{\lambda_i} \phi_i(r) \xi_i(\theta), \tag{4.26}$$

where $\mu(r)$ is the mean of the random field, $\xi_i(\theta)$ are normal, standard, uncorrelated random variables and λ_i, ϕ_i are the eigenvalues and eigenfunctions of the autocovariance kernel. These are obtained by solving the homogeneous Fredholm integral of the second kind:

$$\int_D \text{Cov}_{\rho\rho}(r, r') \phi_i(r') \, dr' = \lambda_i \phi_i(r). \tag{4.27}$$

The eigenfunctions must be orthonormal to each other, following: $\int_D \phi_i(r)\phi_j(r) \, dr = \delta_{i,j}$, where $\delta_{i,j}$ is the Kronecker delta.

To approximate the random field $\rho(r, \theta)$, we use a truncated KL expansion, with M modes:

$$\rho(r, \theta) \approx \hat{\rho}(r, \theta) = \mu^\rho(r) + \sum_{i=1}^{M} \sqrt{\lambda_i} \phi_i(r) \xi_i(\theta). \tag{4.28}$$

To solve the eigenvalue problem of Equation 4.27, we use the Nyström method, which approximates the eigenvalue problem as following:

$$\sum_{j=1}^{N_{quad}} w_j \text{Cov}_{\rho\rho}(r, r_j) \phi_i(r_j) = \lambda_i \phi_i(r), \qquad \forall i = 1, ..., M, \tag{4.29}$$

where r_j with $j = 1, ..., N_{quad} \in D$ are Gauss-Legendre quadrature integration points and w_j the corresponding integration weights.

Equation 4.29 is then solved at the integration points:

$$\sum_{j=1}^{N_{quad}} w_j \text{Cov}_{\rho\rho}(r_n, r_j) \hat{\phi}_i(r_j) = \lambda_i, \phi_i(r_n), \qquad \forall r_n, n = 1, ..., N_{quad}. \tag{4.30}$$

This can be written in matrix form:

$$CWy_i = \lambda_i y_i, \tag{4.31}$$

where C is a N_{quad} x N_{quad} matrix with $C_{nj} = \text{Cov}_{\rho\rho}(r_n, r_j)$, W is a diagonal matrix of the weights w_j and y_i is a vector where $y_{i,n} = \phi_i(r_n)$. This matrix eigenvalue problem can be reformulated into the following matrix eigenvalue problem:

$$\text{B}y_i^* = \lambda_i y_i^*, \tag{4.32}$$

where $\text{B} = \text{W}^{\frac{1}{2}}\text{CW}^{\frac{1}{2}}$. The eigenvalues λ_i and eigenvectors y_i^* are obtained by solving this matrix eigenvalue problem. The eigenvectors y_i can then be computed as $y_i = \text{W}^{-\frac{1}{2}}y_i^*$.

Finally, Equation 4.29 is solved to obtain the eigenfunctions $\phi_i(r)$:

$$\phi_i(r) = \frac{1}{\lambda_i} \sum_{j=1}^{N_{quad}} \sqrt{w_j} y_{i,j}^* \text{Cov}_{\rho\rho}(r, r_j). \tag{4.33}$$

4.6.2. Objective function derivation

The tumor control probability is defined by

$$TCP(D, \theta) = \exp\left[-\int_V \rho(r, \theta) \exp\left\{\left(-\left(\alpha D(r) + \frac{\beta D(r)^2}{N_f}\right)\right)\right\} dr\right], \tag{4.34}$$

where $\rho(r, \theta)$ is a Gaussian random field.

We are interested in the uncertainty in the tumor cell density field of the CTV. To simplify the problem, we investigate a 1D, spherically symmetric model with a spherical GTV with a radius R surrounded by a spherical shell CTV, which is defined from the tumor edge R to a maximum distance r_{max}. We assume this distance to be constant. Then,

$$TCP(D, \theta) = \exp\left[-\int_R^{r_{max}} \rho(r, \theta) 4\pi r^2 \exp\left\{\left(-\left(\alpha D(r) + \frac{\beta D(r)^2}{N_f}\right)\right)\right\} dr\right]. \tag{4.35}$$

The random field $\rho(r, \theta)$ is approximated by the truncated KL expansion $\hat{\rho}(r, \theta)$ (Equation 4.28). To deal with the uncertainty in the tumor cell density field in the CTV, we aim to maximize the expected value of the TCP:

$$\mathbb{E}(TCP(D, \theta)) = \int_\Xi TCP(D, \theta) P_\xi(\xi) \, d\xi, \tag{4.36}$$

where $\xi = (\xi_1(\theta), ..., \xi_M(\theta))^T \in \Xi \subseteq \mathbb{R}^M$ and $P_\xi(\xi)$ is the joint probability density function of the uncorrelated random variables ξ_i of $\hat{\rho}(r, \theta)$:

$$P_\xi(\xi) = \prod_{i=1}^{M} P_{\xi_i}(\xi_i). \tag{4.37}$$

The expected value of the TCP is approximated using K realizations of $\hat{\rho}(r, \theta)$. A more robust way to approximate the expected TCP would be to use Gaussian quadratures to approximate the multidimensional integral in Equation 4.36. Time limitations on this research prevented us from implementing such an approximation. For the demonstration of the applicability of the KL-expansion, using K realizations of $\hat{\rho}(r, \theta)$ is however sufficient to approximate the expected TCP.

The same discretization of the spatial integral as in Section 4.2 is used. The investigated volume is divided into S concentric spherical shells of equal volume $V_s = \frac{4}{3}\pi(r_{s+1}^3 - r_s^3)$ with radii r_s, $s = 1, ..., s+1$. The dose within a shell is a constant D_s. This yields the following approximation of the expected TCP:

$$\mathbb{E}(TCP(D, \theta)) \approx ETCP(D, \hat{\rho}) = \frac{1}{K} \sum_{k=1}^{K} \exp\left[-\sum_{s=1}^{S} \hat{\rho}_{s,k} V_s \exp\left(-\left(\alpha D_s + \frac{\beta D_s^2}{N_f}\right)\right)\right], \tag{4.38}$$

where $\hat{\rho}_{s,k}$ is the discretization of the k-th realization of the KL-approximation $\hat{\rho}(r, \theta)$ (Eq. 4.28):

$$\hat{\rho}_{s,k} = \mu_s^\rho + \sum_i^M \sqrt{\lambda_i} \phi_{i,s} \xi_{i,k}. \tag{4.39}$$

For the optimization, we also need the gradient and Hessian of the ETCP. For the gradient, we have

$$
\frac{\mathrm{d}ETCP(D,\hat{\rho})}{\mathrm{d}D_l} = \frac{1}{K} \sum_{k=1}^{K} \exp\left[-\sum_{s=1}^{S} \hat{\rho}_{s,k} V_s \exp\left(-\left(\alpha D_s + \frac{\beta D_s^2}{N_f}\right)\right)\right] \cdot
$$
$$
\left[\hat{\rho}_{l,k} V_l \exp\left(-\left(\alpha D_l + \frac{\beta D_l^2}{N_f}\right)\right)\right]\left(\alpha + \frac{2\beta D_l}{N_f}\right) \tag{4.40}
$$

and for the Hessian

$$
\frac{\mathrm{d}^2 ETCP(D,\hat{\rho})}{\mathrm{d}D_l\,\mathrm{d}D_m} = \frac{1}{K} \sum_{k=1}^{K} \exp\left[-\sum_{s=1}^{S} \hat{\rho}_{s,k} V_s \exp\left(-\left(\alpha D_s + \frac{\beta D_s^2}{N_f}\right)\right)\right] \cdot
$$
$$
\left\{\left[\hat{\rho}_{l,k} V_l \exp\left(-\left(\alpha D_l + \frac{\beta D_l^2}{N_f}\right)\right)\right]\left(\alpha + \frac{2\beta D_l}{N_f}\right)\left[\hat{\rho}_{m,k} V_m \exp\left(-\left(\alpha D_m + \frac{\beta D_m^2}{N_f}\right)\right)\right]\left(\alpha + \frac{2\beta D_m}{N_f}\right) +\right.
$$
$$
\left.\delta_{l,m}\left[\hat{\rho}_{l,k} V_l \exp\left(-\left(\alpha D_l + \frac{\beta D_l^2}{N_f}\right)\right)\right]\left[-\left(\alpha + \frac{2\beta D_l}{N_f}\right)^2 + \frac{2\beta}{N_f}\right]\right\}. \tag{4.41}
$$

Apart from directly optimizing the ETC as an objective, we are also interested in a penalized objective for the KL-based optimization. The same penalized objective as was derived in Section 4.3 is used, but with $ETCP(D,\hat{\rho})$ instead of $ETCP(D)$:

$$
\mathrm{pen\_obj} = (2 - w_{pen}) \cdot ETCP(D,\hat{\rho}) - w_{pen} \cdot \frac{\sum_s D_s^2 \cdot V_s}{\sum_s D_{max}^2 \cdot V_s}, \tag{4.42}
$$

where $V_s = 4/3\pi\left(\mathrm{r}_{s+1}^3 - \mathrm{r}_s^3\right)$. The gradient is given by

$$
\frac{\mathrm{d}(\mathrm{pen\_obj})}{\mathrm{d}D_l} = (2 - w_{pen}) \cdot \frac{\mathrm{d}ETCP(D,\hat{\rho})}{\mathrm{d}D_l} - w_{pen} \cdot \frac{2D_l \cdot V_l}{\sum_s D_{max}^2 \cdot V_s} \tag{4.43}
$$

and the Hessian is given by

$$
\frac{\mathrm{d}^2(\mathrm{pen\_obj})}{\mathrm{d}D_l\,\mathrm{d}D_m} = (2 - w_{pen}) \cdot \frac{\mathrm{d}^2 ETCP(D,\hat{\rho})}{\mathrm{d}D_l\,\mathrm{d}D_m} - \delta_{l,m} \cdot w_{pen} \cdot \frac{2V_l}{\sum_s D_{max}^2 \cdot V_s}. \tag{4.44}
$$

4.6.3. Demonstration of Karhunen-Loève expansion for CTV optimization

To demonstrate the use of the Karhunen-Loève expansion in treatment plan optimization for uncertainties in the CTV, we use four different mean tumor cell density fields μ^ρ to create four KL models for the tumor cell density $\hat\rho$.

First, we investigate a volume with a constant mean tumor cell density

$$\mu_s^\rho = \mu_{in}^\rho \tag{4.45}$$

and a volume with a mean tumor cell density that follows a Gaussian decrease over the distance

$$\mu_s^\rho = \mu_{in}^\rho \cdot \exp\left(-\frac{(r_s - R)^2}{2\sigma_{\mu^\rho}^2}\right), \tag{4.46}$$

where μ_{in}^ρ is the input mean tumor cell density and $\sigma_{\mu^\rho}^2$ is the variance of the Gaussian. The standard deviation of the Gaussian random field $\sigma^\rho(r_s)$ (Equation 4.25) is set to be a constant σ^ρ throughout the volume.

Secondly, we investigate two volumes with a simulated physical barrier. We assume that tumor cells cannot grow beyond this physical barrier, which we place at $r_s = r_{barr}$. Again a volume with a constant mean tumor cell density is investigated, but now we set $\mu_s^\rho = 0$ from a distance $r_s = r_{barr}$. Furthermore, the standard deviation of the Gaussian random field $\sigma^\rho(r_s)$ is set to be a constant σ^ρ up to $r_s = r_{barr}$ and 0 beyond r_{barr}:

$$\mu_s^\rho = \begin{cases} 0 \\ \mu_{in}^\rho \end{cases} \quad \text{and} \quad \sigma^\rho(r_s) = \begin{cases} 0 & \text{if } r_s > r_{barr} \\ \sigma^\rho & \text{if } r_s \le r_{barr} \end{cases}. \tag{4.47}$$

The same barrier is also imposed on a volume with a Gaussian decreasing mean tumor cell density.

$$\mu_s^\rho = \begin{cases} 0 \\ \mu_{in}^\rho \cdot \exp\left(-\frac{(r_s-R)^2}{2\sigma_{\mu^\rho}^2}\right) \end{cases} \quad \text{and} \quad \sigma^\rho(r_s) = \begin{cases} 0 & \text{if } r_s > r_{barr} \\ \sigma^\rho & \text{if } r_s \le r_{barr} \end{cases}. \tag{4.48}$$
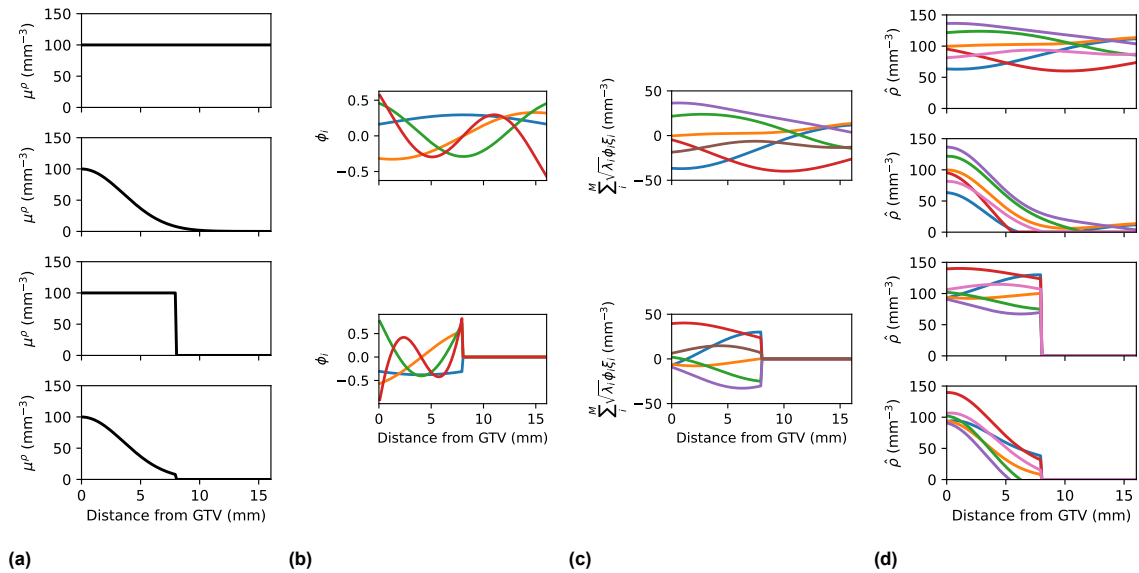
Figure 4.2: Visualization of the construction of several tumor cell density field realizations $\hat\rho_{s,k}$. **(a)** Inputs for the mean tumor cell density field μ_ρ. From top to bottom: constant μ_ρ, Gaussian decreasing μ_ρ, constant μ_ρ with a physical barrier and Gaussian decreasing μ_ρ with a physical barrier. **b** The 4 eigenfunctions ϕ_i for volumes without (top) and with (bottom) a physical barrier. **(c)** Examples of the series expansions $\sum_i^M \sqrt{\lambda}_i \phi_{i,s} \xi_{i,k}$ of the tumor cell density field for volumes without (top) and with (bottom) a physical barrier. **(d)** Examples of output realizations for the tumor cell density field $\hat\rho_{s,k}$.

These mean tumor cell density fields are plotted in Figure 4.2a from top to bottom, respectively. In Figure 4.2b, the first 4 eigenfunctions are plotted for the volumes without and with a physical barrier.

Furthermore, the corresponding series expansions $\sum_i^M \sqrt{\lambda_i}\phi_{i,s}\xi_{i,k}$ are plotted in Figure 4.2c for 6 random realizations of $\xi_{i,k}$. The two plots correspond to the volumes without and with a physical barrier, respectively. Finally, the 6 simulated random tumor cell density fields that correspond to the inputs in Figure 4.2a-4.2c are plotted in Figure 4.2d.

For the demonstration of probabilistic treatment plan optimization using the KL expansion, the parameters detailed in Table 4.3 are used as well as the optimization constraints that were introduced in Section 4.4.

Table 4.3: Parameters for the Karhunen-Loève expansion of the tumor cell density field

Parameter	Value
Standard deviation σ^ρ of $\rho(r, \theta)$ (mm^{-3})	10
Correlation length b of the autocorrelation function (mm)	8.0
Number of modes for KL expansion M	4
Number of quadrature points N_{quad}	30
Number of shells S	150
Input mean tumor cell density μ_{in}^ρ (mm^{-3})	100
Variance of the Gaussian decreasing mean $\sigma_{\mu\rho}^2$ (mm^2)	12.5
Distance of the physical barrier r_{barr} (mm)	8.0
Number of realizations K	5000
Tumor radius R (mm)	30
Maximum dose D_{max} (Gy)	60.0
Number of treatment fractions N_f	4
α (Gy^{-1})	0.15
β (Gy^{-2})	0.058
Energy constant C	[0.5, 0.6]

5

Results

In this chapter, we will discuss the results of the investigation into probabilistic treatment planning for CTV uncertainties. In Section 5.1, the current results will be compared to a previous investigation into the problem. Subsequently, the results of the probabilistic optimization for different tumor sites will be discussed in Section 5.2 and finally in Section 5.3, a novel approach will be demonstrated using a Karhunen-Loève expansion to simulate the tumor cell density field.

5.1. Comparison to previous results

In this section, the results of the conceptual ETCP model will be compared to the previous results of Briggeman [8]. For this comparison, similar parameters were used as in [8]. The reader is referred to [8] for the exact models used in that study.

Figure 5.1 shows the results for the parameters that were provided in Subsection 4.5.1 for 2 different optimization options, without (Figure 5.1a) and with scaling (Figure 5.1b) of the objective function, for L = 1.1 mm, L = 1.7 mm and L = 2.6 mm. The corresponding ETCP values and used energy as a percentage of the maximum allowed energy are provided in Table 5.1.

Without scaling, the optimized dose distributions all follow a similar pattern where they slightly decrease up until a drop-off at a certain distance from the GTV, after which the dose is constant at a much lower level. This drop-off is at ≈ 5.1 mm, 6.5 mm, and 9.6 mm for L = 1.1 mm, 1.7 mm and 2.6 mm, respectively. The corresponding ETCP values are 0.995, 0.986 and 0.986. Furthermore, 99.7% of the maximum allowed energy is used when L = 1.1 mm, 99.5% when L = 1.7 mm and 99.4% when L = 2.6 mm.

With scaling, the optimized dose distributions follow the maximum dose up until a drop-off at a

(a)   (b)
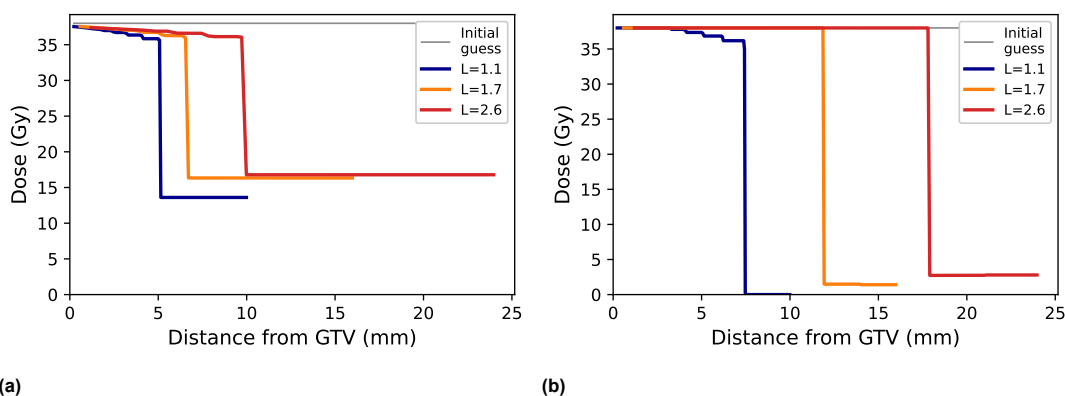
Figure 5.1: Optimized dose distributions as a function of the radius for three different ETCP models with three different constants L = 1.1 mm (Δ_{max} = 5 mm), L = 1.7 mm (Δ_{max} = 8 mm) and L = 2.6 mm (Δ_{max} = 12 mm). **(a)** Dose distributions optimized without scaling the objective, **(b)** Dose distributions optimized using a scaling factor of 1x10^6 for L = 1.1 mm and L = 1.7 mm and 1x10^8 for L = 2.6 mm.

Table 5.1: Optimized ETCP values and used energy as a percentage of the maximum allowed energy for the models with Δ_{max} = 5 mm, Δ_{max} = 8 mm and Δ_{max} = 12 mm for an unscaled and a scaled objective.

Maximum (mm)	L (mm)	Scale factor	ETCP	Energy (%)
Δ_{max} = 5	1.1	1	0.995	99.7
		1×10^6	0.999	100
Δ_{max} = 8	1.7	1	0.986	99.5
		1×10^6	0.999	100
Δ_{max} = 12	2.6	1	0.986	99.4
		1×10^8	0.999	99.9

certain distance from the GTV. The dose distribution for L = 1.1 decreases slowly from the maximum dose up until the drop-off. In all three dose distributions, the dose drops to (almost) 0 Gy after the drop-off. This drop-off is at ≈ 7.5 mm, 12 mm, and 18 mm for L = 1.1 mm, L = 1.7 mm and L = 2.6 mm, respectively. After scaling, the ETCP value has increased to 0.999 for all three values of L and the used energy has increased to 100%, 100% and 99.9% of the maximum allowed energy for L = 1.1 mm, L = 1.7 mm and L = 2.6 mm, respectively.

In Figure 5.2, the previous results from Briggeman [8] are shown. These are the results for an energy constraint constant C_{Br} = 1, which corresponds to C ≈ 0.2 in the current model, as the linear total energy constraint was computed differently. Briggeman [8] defined the constraint as follows:

$$\sum_s V_s D_s \leq C_{Br} \sum_s V_{MDE} D_{max},$$

where $V_{MDE} = 4/3\pi \left((R + \Delta_{max})^3 - R^3 \right)$ is the volume that corresponds to a CTV shell with outer radius Δ_{max}. In the current model the energy constraint is defined as

$$\sum_s V_s D_s \leq C \sum_s V_s D_{max}. \tag{5.1}$$
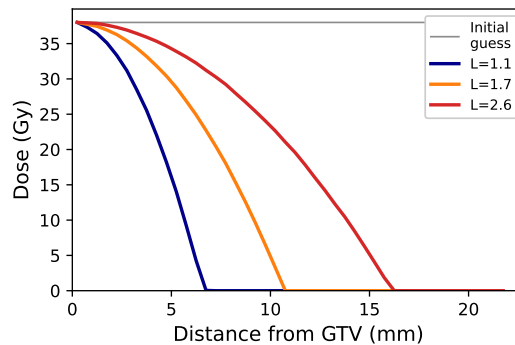
Figure 5.2: Optimized dose distributions from Briggeman [8] for the three different constants L = 1.1 mm (Δ_{max} = 5 mm), L = 1.7 mm (Δ_{max} = 8 mm) and L = 2.6 mm (Δ_{max} = 12 mm).

These optimized dose distributions follow a slowly decreasing curve, until they reach 0 Gy. The corresponding ETCP values were 0.984, 0.985 and 0.976 and 84.1%, 90.0% and 93.0% of the energy was used for L = 1.1 mm, L = 1.7 mm and L = 2.6 mm, respectively. Intuitively, these results seem correct as a decreasing probability density function $P_\Delta(\Delta)$ is used, which indicates that the probability for tumor cells to be present is high close to the GTV and decreases as the distance to the GTV increases. Therefore, it is expected that the highest dose is needed close to the GTV and the needed dose then decreases as the distance from the GTV increases. However, some mistakes were found in the used model and after correctly implementing the volume shell computation the results from [8] could not be replicated. Instead, the results as shown in Figure 5.1 were obtained. If the ETCP of the dose

distributions in Figure 5.2 is recomputed using the current model, the ETCP values were found to be 0.984, 0.983 and 0.980 for L = 1.1 mm, L = 1.7 mm and L = 2.6 mm, respectively. These values are still high, but they are not optimal, as shown by the higher ETCP values that were obtained for the scaled objectives (Table 5.1).

Table 5.2: Optimized ETCP values for the dose distributions in Figure 5.2 from [8], the recomputed ETCP values using the current model and used energy as a percentage of the maximum allowed energy for different values of Δ_{max}.

Maximum (mm)	L (mm)	ETCP according to [8]	recomputed ETCP	Energy (%)
Δ_{max} = 5	1.1	0.984	0.984	84.1
Δ_{max} = 8	1.7	0.985	0.983	90.0
Δ_{max} = 12	2.6	0.976	0.980	93.0

Optimization behavior

There are two main explanations for the optimized dose distribution results displayed in Figure 5.1a.

Firstly, the TCP has a multiplicative nature, so if any part of the volume is underdosed, the TCP quickly drops towards 0. This means that to maximize the TCP for a particular Δ, all the parts of the CTV have to be dosed properly to avoid the TCP from dropping towards 0. Intuitively, it is expected that the optimized dose distributions would look more like in Figure 5.2, where most dose is distributed close to the GTV in the high probability areas and the dose declines over the distance until it becomes 0 in the lower probability areas. However, decreasing some dose in the high probability areas would decrease the TCP much more, than increasing the dose in the lower probability regions would increase the TCP. To maximize the TCP, the dose distribution is therefore driven to give the maximum allowed dose to as large a volume as is allowed by the energy constraint. This conclusion is strengthened by the percentage of the maximum energy that is used: in all the models, almost all the allowed energy is used in the distributions if no scaling is used for the ETCP.

Aside from the multiplicative nature of the TCP, there is a second reason for the optimized results. The TCP is a sigmoidal (S-like) function of the dose, as is shown in Figure 5.3. This means that for low and high dose values, the function is almost constant and the gradient values become ≈ 0. This causes numerical inaccuracies and is the reason that the dose after the drop-off does not get pushed to 0 using the unscaled objective. Pushing this dose to 0 would allow for a slightly larger area to obtain the full maximum dose, thus resulting in a higher ETCP. The optimizer is however not able to do this, as the gradient is ≈ 0 after the drop-off due to the low ETC at the lower dose values. The same problem is encountered before the drop-off, where the ETCP becomes ≈ 1 and the gradient again is ≈ 0, which prevents the optimizer from pushing the dose to the maximum dose here. As shown in Figure 5.1b, scaling the objective function helps to increase the values in the gradient to force the optimization to run for longer. The dose before the drop-off is pushed to the maximum for as large an area as allowed by the energy constraint and the dose is also pushed down more towards 0 after the drop-off due to the scaling. This is illustrated further by the fact that 100% of the allowed energy is used when the ETCP objective is scaled by a scale factor.
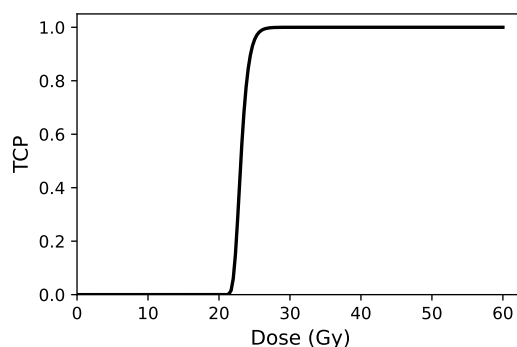
Figure 5.3: TCP as a function of the dose. The TCP follows an S-curve.

5.2. Results for the different tumor sites

In this section, the results of dose optimization using the different objectives that were derived in Section 4.2 and 4.3 will be discussed for the four tumor sites. First, the results for the ETCP and ELTCP models are shown in Subsection 5.2.1, followed by the results for the penalized ETCP models in Subsection 5.2.2.

5.2.1. Optimizing the ETCP/ELTCP for different tumor sites

Figure 5.4 shows the optimal dose distributions for the different tumor sites, for both the ETCP and the ELTCP model. The corresponding ETCP values and used energy as a percentage of the maximum allowed energy are provided in Table 5.3.
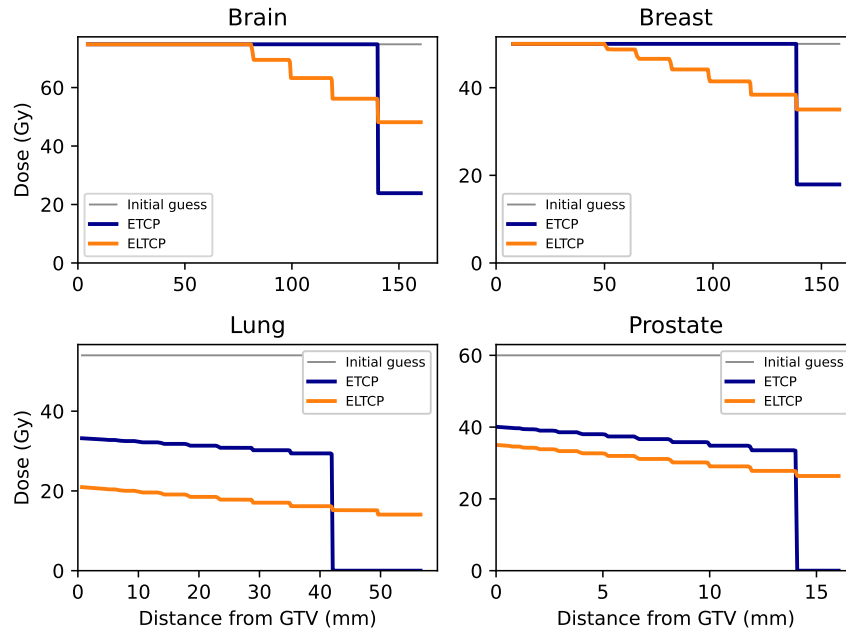
Figure 5.4: Optimized dose distributions for the 4 different tumor sites, for both the ETCP model and the ELTCP model.

Table 5.3: Optimized ETCP values and used energy as a percentage of the maximum allowed energy for the tumor sites for the ETCP and ELTCP models.

Tumor Site	Model	ETCP	Energy (%)
Brain	ETCP	0.790	99.8
	ELTCP	0.790	100
Breast	ETCP	0.900	99.9
	ELTCP	0.897	100
Lung	ETCP	0.999	100
	ELTCP	0.836	100
Prostate	ETCP	1.00	100
	ELTCP	0.996	100

Brain

The dose distribution obtained by optimizing the ETCP objective follows the maximum allowed dose up until the optimized dose drops down at a distance of ≈ 140 mm from the GTV to a lower dose level. The dose is constant after the drop. The corresponding ETCP is 0.790 and almost all of the maximum allowed energy (99.8%) is used. The optimal dose distribution would give the maximum dose to as big an area as allowed by the energy constraint and zero dose elsewhere. As discussed in Section 5.1, the gradient is ≈ 0 after the drop-off, so the optimizer cannot push the dose further towards the optimum.

The resulting dose values from the ELTCP model follow the maximum dose up until ≈ 80 mm from the GTV, after this the dose starts decreasing slowly. The corresponding ETCP is 0.790 as well and all the allowed energy is used up. Clearly, the optimizer is optimizing the ELTCP by giving dose throughout the whole volume. This is due to the nature of the logarithmic TCP: if for any part of the volume the TCP comes close to 0, the ELTCP value becomes very large, which drives the optimization to avoid any cases where this happens. This means that even in the lower probability areas (outer volume shells), a high dose is necessary to yield a satisfying optimization result. The slight decrease is likely due to the influence of the probability distribution of the MDE $P_\Delta(\Delta)$.

Despite the relatively big difference in the dose distributions for both objectives, the obtained ETCP is approximately equal. The ETCP objective gives the maximum dose to as large a volume as possible and then tries to get zero dose elsewhere, whereas the ELTCP objective tries to give dose throughout the volume. This means that with the ELTCP objective, some dose gets redistributed from the inner regions to the outer regions of the volume. Clearly, the redistribution of dose by the ELTCP objective results in a large enough gain of tumor control in the outer regions to make up for the loss in tumor control in the inner regions, thus resulting in similar ETCP values for both models.

Breast
The optimized dose distributions for breast look similar to the optimized dose distributions for brain. The dose distribution resulting from optimizing the ETCP has the maximum allowed dose up to ≈ 140 mm from the GTV after which the dose drops down to a lower dose level. The corresponding ETCP is 0.900 and 99.9% of the maximum allowed energy is used. The optimized dose after the drop-off is not 0 Gy due to the ≈ 0 values in the gradient that prevent the optimizer from pushing the dose values to 0 Gy.

The resulting dose distribution from optimizing the ELTCP follows the maximum dose up until ≈ 50 mm from the GTV after which the dose starts slowly decreasing. The corresponding ETCP is 0.897 and thus slightly lower than the ETCP obtained from optimizing the ETCP itself. Furthermore, 100% of the allowed energy is used in the dose distribution, which is as expected if you take into account that underdosing any part of the volume is avoided in the ELTCP optimization as was just discussed for the brain dose distribution results.

Similar to the results for brain, the obtained ETCP is approximately equal for both the ETCP and the ELTCP model. For breast however, the ETCP value for the ELTCP model is slightly lower than for the ETCP model. The gained tumor control in the outer region from the redistribution of dose thus does not make up entirely for the loss in tumor control in the inner region.

Lung
The dose distribution for lung obtained from optimizing the ETCP, is slowly decreasing until a drop-off at ≈ 40 mm from the GTV. The dose is ≈ 0 Gy after the drop-off. The corresponding ETCP is 0.999 and 100% of the maximum allowed energy is used in the dose distribution. In the case of the lung, a smaller energy constraint constant of 0.3 was used as this already resulted in a very high ETCP. The optimizer was able to push the dose values to 0 Gy after the drop-off, so the scaling factor makes the values of the gradient large enough to help the optimizer push the dose after the drop-off to 0 Gy. The slight decrease in the dose before the drop-off is likely a result of the small influence of the probability distribution of the MDE $P_\Delta(\Delta)$. This effect can likely show up as the dose does not need to be pushed to the maximum dose for a high ETCP value.

The resulting dose distribution from the ELTCP model has much lower dose values than the result from the ETCP model. It slowly decreases throughout the volume, as the ELTCP optimization results in dose necessary in the whole volume for a high ETCP. The corresponding ETCP value is 0.836 and is significantly lower than for the ETCP model. This is to be expected, as the energy constraint forces the dose to be significantly lower than it was in the ETCP model, before the dose drops off to 0 Gy. Accordingly, the maximum allowed energy is used for the dose distribution.

Prostate
The results for prostate look similar to the results for lung. The dose distribution resulting from optimizing the ETCP, decreases slowly over the distance up until a drop-off point at ≈ 14 mm, after which the dose is ≈ 0 Gy. The corresponding ETCP is 1.00 and 100% of the maximum allowed energy is used. Again, the slight decrease over the distance is likely a result of the small influence of the probability distribution of the MDE $P_\Delta(\Delta)$.

When the ELTCP is optimized for prostate, the dose is distributed throughout the volume, but the dose is only slightly lower than for the ETCP optimization. This results in a high ETCP of 0.996, while the maximum allowed energy is used.

Comparison between tumor sites
The optimizations for brain and breast yield similar results for both the ETCP and the ELTCP objectives. Similarly, the results for lung and prostate also resemble each other. The main difference between both groups is that for the first group, the maximum ETCP is nowhere near 1, while for the second group ETCP values of ≈ 1 are obtained. For brain, the maximum ETCP that can be obtained with the used tumor parameters by administering the maximum allowed dose to the full volume is 0.790 and for breast, the maximum obtainable ETCP is 0.900. The optimized dose distributions allow for tumor control that is similar to this maximum possible tumor control, despite not depositing the maximum dose throughout the volume. However, as the ETCP does not approach 1.00, a large part of the volume receives the maximum dose, unlike in the cases of lung and prostate, where no part of the volume receives the maximum dose. Furthermore, the optimization is able to push the dose to 0 Gy for both lung and prostate, while it cannot do this for brain and breast. The investigated volumes for brain and breast are much larger than those for lung and prostate, as the Δ_{max} is much larger as well. The dose optimization is sensitive to the maximum radius of the investigated volume, as a larger volume is more difficult for the optimizer to handle. We use an exponential distribution for the probability distribution of the MDE $P_\Delta(\Delta)$, which is implemented in the model using a Gauss-Laguerre quadrature. For a model with a high maximum radius, many of the quadrature points will be far away and have very low weights. Shells that are far away from the GTV will therefore be difficult to optimize, due to the very small quadrature weights that cause the values of the gradient to approach 0. This effect can also somewhat be observed in Figure 5.1b as well, as the dose distribution for L = 1.1 mm is ≈ 0 Gy after the drop-off, but the dose after the drop-off for both L = 1.7 mm and L = 2.6 mm is progressively further away from 0 Gy. To counter this problem for larger volumes, an explicitly truncated distribution could be used for $P_\Delta(\Delta)$, so that there are less quadrature points at large distances from the GTV with very low weights.

5.2.2. Penalized model for different tumor sites
Figure 5.5 shows the optimal dose distributions for the different tumor sites, for the penalized ETCP model. The used penalty is the squared overdose, which penalizes dose present in the volume. The penalized model is detailed in Section 4.3. The corresponding ETCP values and used energy as a percentage of the maximum allowed energy are provided in Table 5.4.
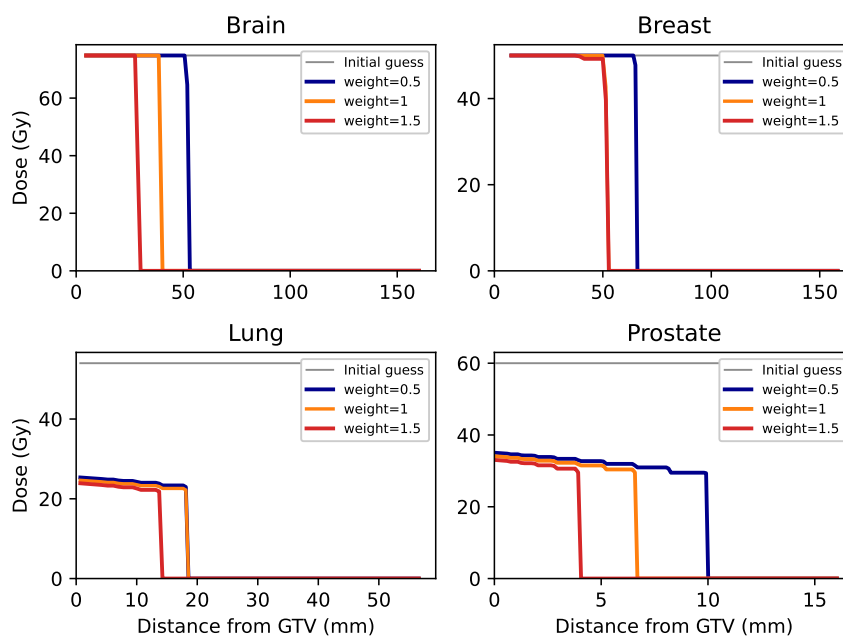
Figure 5.5: Optimized dose distributions for the 4 different tumor sites for the penalized ETCP model. The results are displayed for 3 different weights of the squared overdose penalty: w_{pen} = 0.5, w_{pen} = 1 and w_{pen} = 1.5.

Table 5.4: Optimized ETCP values and used energy as a percentage of the maximum allowed energy for the 4 tumor sites for the penalized ETCP model for three different weights w_{pen}.

Tumor Site	Penalty weight	ETCP	Energy (%)
Brain	w_{pen} = 0.5	0.785	8.31
	w_{pen} = 1.0	0.774	4.60
	w_{pen} = 1.5	0.743	2.50
Breast	w_{pen} = 0.5	0.897	11.2
	w_{pen} = 1.0	0.890	6.19
	w_{pen} = 1.5	0.888	6.12
Lung	w_{pen} = 0.5	0.965	17.2
	w_{pen} = 1.0	0.964	16.7
	w_{pen} = 1.5	0.923	10.7
Prostate	w_{pen} = 0.5	0.995	55.5
	w_{pen} = 1.0	0.980	33.4
	w_{pen} = 1.5	0.917	18.3

Brain

The optimized dose distributions for brain for the different penalty weights all follow the maximum dose up until a certain distance from the GTV and then the dose drops down to 0 Gy. The dose distributions drop off at ≈ 52 mm, 40 mm and 30 mm, for a penalty weight w_{pen} of 0.5, 1.0 and 1.5, respectively. The corresponding ETCP values are 0.785, 0.774 and 0.743 and only 8.31%, 4.60% and 2.40% of the allowed energy was used. The penalized dose distributions drop off much earlier within the volume than was the case for the optimized dose distribution from the unpenalized ETCP objective which dropped off at ≈ 140 mm (Figure 5.4). In the unpenalized ETCP model the optimizer had trouble pushing the dose to 0 Gy as the gradient values of the ETCP objective were ≈ 0. In the penalized model, this problem is not present, as the gradient values of the penalized objective are driven by both the ETCP and the squared overdose. When the gradient of the ETCP becomes ≈ 0, the gradient of the squared overdose pushes the optimization further and drops the dose to 0 Gy. Additionally, dose in the low probability areas of the volume is pushed towards 0 Gy as well by the penalty. The volume that receives dose decreases, by increasing w_{pen}. The squared overdose pushes the dose to 0 Gy, until the contribution of the ETCP to the optimization objective becomes big enough to overcome the penalty and push the dose to the maximum. The ETCP obtained by the unpenalized ETCP was 0.790, which is only slightly higher than the ETCP values obtained from the penalized model. A large reduction in deposited energy was thus obtained using the penalized model, while the ETCP values only decreased slightly.

Breast

For breast, the optimized dose distributions for the different penalty weights again follow the maximum dose up until a certain distance from the GTV after which the dose drops down. The dose distributions drop off to 0 Gy at ≈ 65 mm, 52 mm and 52 mm from the GTV, for a penalty weight w_{pen} of 0.5, 1.0 and 1.5, respectively. The corresponding ETCP values are 0.897, 0.890 and 0.888 and only 11.2%, 6.19% and 6.12% of the allowed energy was used. Again, the penalized distributions drop off to 0 Gy much closer to the GTV than for the unpenalized ETCP model (at ≈ 140 mm, Figure 5.4).

The ETCP value for the unpenalized model was 0.900. Using a penalized model allowed for a large reduction in deposited energy (from 100% of the maximum allowed energy to 6.12-11.2%), while maintaining a high ETCP of 0.888-0.897.

Contrary to brain, there seems to be only a small difference in the dose distribution for the penalty weights w_{pen} of 1 and 1.5. There is a small decrease in the used energy (6.19% to 6.12%), but the drop-off point is at the same distance of 52 mm from the GTV. Upon close inspection, it is observed that the dose right before the drop-off is slightly lower for w_{pen} = 1.5, than for w_{pen} = 1. The results for brain show a clear decrease in the irradiated volume by increasing the penalty weight from 1 to 1.5. As such a clear decrease is not present for breast, the optimized dose distributions were investigated for more penalty weights. The drop-off points of the dose for breast for penalty weights ranging from 0 to 2 are plotted in Figure 5.6a. Clearly, the drop-off point does not linearly decrease by increasing w_{pen}. Instead, there are only a few distances at which a drop-off point can be found for the different

(a)

(b)
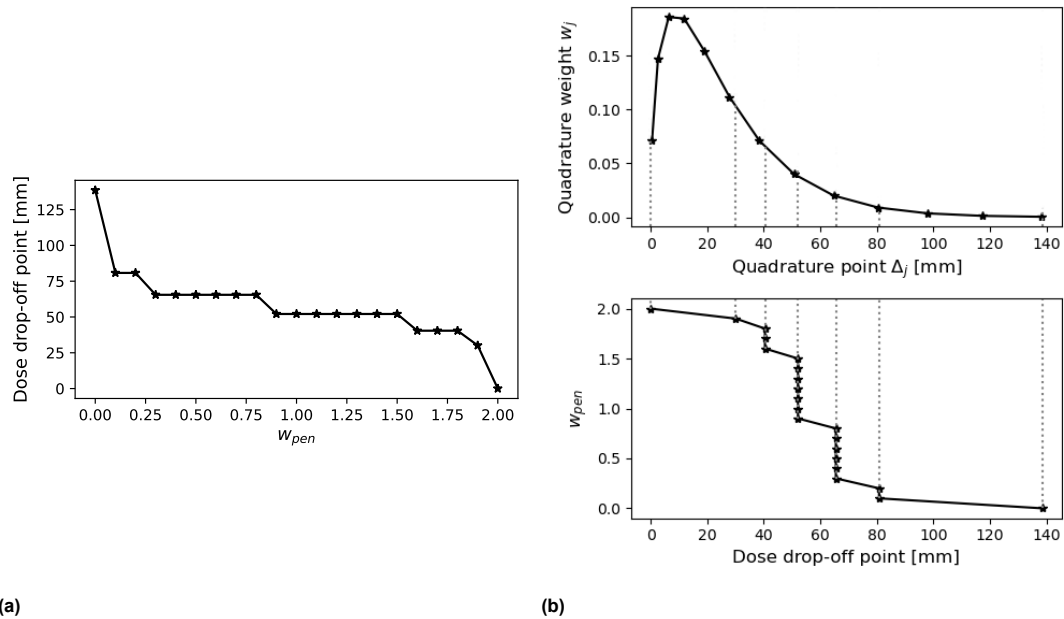
Figure 5.6: **(a)** Drop-off points of the dose as a function of the penalty weight w_{pen} for the breast model. **b** *top*: Gauss-Laguerre quadrature weights w_j^Δ as a function of the corresponding quadrature points Δ_j for the breast model up to a distance of ≈140 mm from the GTV; *bottom*: penalty weight w_{pen} as a function of the drop-off points of the dose for the breast model to show that the drop-off points correspond to the quadrature points.

weight factors. By examining the dose distributions, it is seen that upon increasing w_{pen} by 0.1, there is either a decrease in the distance of the drop-off point or the drop-off point does not move, but there is a decrease in dose in the last few shells before the drop-off. After inspection of dose distributions for different weights for brain, lung and prostate, it can be concluded that this behavior also happens for the other tumor sites. This stepping behavior results from the Gauss-Laguerre quadrature that was used to discretize the integration in Equation 4.9 over Δ. A selection of these quadrature points up to ≈140 mm from the GTV is shown in the top plot in Figure 5.6b. In the bottom plot, the dose drop-off points and corresponding penalty weights w_{pen} are again plotted, but with flipped axes. From these two figures, it is clear that the location of the drop-off points is related to the location of the quadrature points. The drop-off points are located in the nearest volume shell with a larger distance from the GTV than the quadrature points. All shells that correspond to the volume between two quadrature points have the same probability of having microscopic disease. Therefore, in the shells between quadrature points, the ETCP is constant and the only thing driving the optimization is the penalty, which pushes the dose down to 0. Essentially what this means, is that the volume is subdivided into different regions defined by the quadrature points and the drop-off points correspond to these quadrature points. Near which quadrature point the dose drops off, is dependent on the weight of the penalty.

Lung

For lung, the optimized dose distributions slowly decrease up until a certain distance from the GTV after which the dose drops down. The maximum dose close to the GTV is ≈ 24-25 Gy for all 3 penalty weights w_{pen}, which is significantly lower than the maximum dose that was obtained using the unpenalized ETCP model (≈ 33 Gy). The dose distributions drop off to 0 Gy at ≈ 19 mm, 19 mm and 14 mm, for a penalty weight w_{pen} of 0.5, 1.0 and 1.5, respectively. The corresponding ETCP values are 0.965, 0.964 and 0.923 and 17.2%, 16.7% and 10.7% of the allowed energy was used.

For the unpenalized ETCP model, the ETCP value was 0.999, 100% of the allowed energy was used and the dose dropped to 0 Gy at ≈ 40 mm from the GTV. Clearly, a large reduction in deposited energy is obtained using a penalized model, while high tumor control is maintained.

Prostate

The optimized dose distributions for prostate for the different penalty weights slowly decrease until a drop-off after which the dose is ≈ 0 Gy. The maximum dose close to the GTV is ≈ 33-35 Gy for the different w_{pen}, while the maximum dose was 40 Gy for the unpenalized ETCP model. The dose

distributions drop off to 0 Gy at ≈ 10 mm, 6.7 mm and 4.2 mm, for a penalty weight w_{pen} of 0.5, 1.0 and 1.5, respectively. The corresponding ETCP values are 0.995, 0.980 and 0.917 and 55.5%, 33.4% and 18.3% of the allowed energy was used. For the unpenalized ETCP model, an ETCP of 1.00 was obtained, 100% of the allowed energy was used and the dose dropped to 0 Gy at ≈ 14 mm.

Penalized ETCP objective
Clearly, using a penalized ETCP objective can help to avoid giving large amounts of dose to the healthy tissue, while still achieving high tumor control. The balance between a high ETCP value and sparing healthy tissue can be adjusted by varying the penalty weight w_{pen} that is used. As discussed, the drop-off points of the dose are related to the used quadrature points. The results are therefore dependent on the discretization that was used for the integration and the dose only drops off at certain locations, despite the use of a large number of volume shells to discretize the microscopic disease area.

In Figure 5.7 the ETCP is shown as a function of the integral organ dose that is deposited into the investigated volume, for the different tumor sites. For both brain and breast, the ETCP value quickly rises to almost the maximum achieved ETCP for a relatively small integral organ dose. This corresponds to the fact that only small percentages of the maximum allowed energy were used in the penalized ETCP models for both these tumor sites (Table 5.4). For lung and prostate, the ETCP value increases more slowly to the maximum achieved ETCP and accordingly, indeed larger percentages of the maximum allowed energy were used in the penalized ETCP models for these two tumor sites (Table 5.4). It must be kept in mind that the investigated volumes for brain and breast are much larger than those for lung and prostate, which likely has a large influence on the dependence of the ETCP on the integral organ dose. Especially for brain and breast, the penalized objective results in a massive decrease in dosage to the low MDE probability areas, while still maintaining a high tumor control. As is evidenced for all the tumor sites, using the overdose penalty allows for organ sparing, with minimal loss to the tumor control and thus effectiveness of the treatment plan. The balance between maximizing tumor control and sparing of normal tissue can be adjusted to preference by varying the weight of the penalty. It must be decided what is most important to achieve the desired balance. Maximizing tumor control in the CTV will result in the need to accept extra dose to normal tissue and sparing the normal tissue will result in a loss of tumor control.
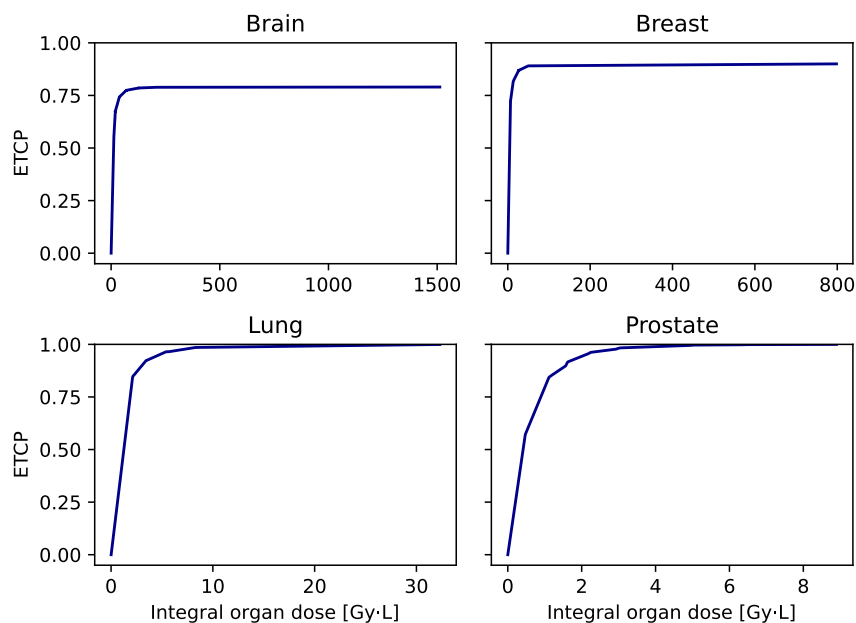
Figure 5.7: ETCP as a function of the integral organ dose.

5.3. Demonstration of the KL-expansion model

In this section, the optimization of the dose distribution using the KL-expansion to simulate random tumor cell density fields in the CTV area will be discussed.
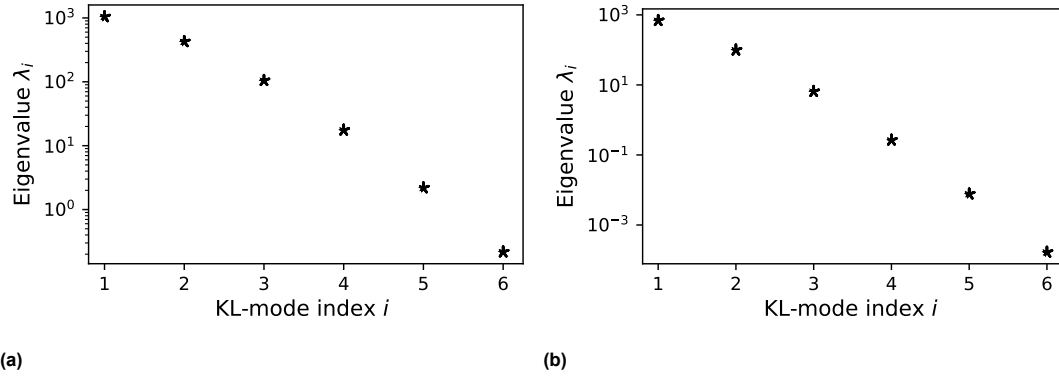
Figure 5.8: Eigenvalues λ of the KL expansions of the tumor cell density field, **(a)** without physical barrier and **(b)** with physical barrier.

To create tumor cell density field realizations, the Karhunen-Loève expansion is truncated. The first 6 eigenvalues are shown in Figure 5.8a for the tumor cell density field without physical barrier and in Figure 5.8b for the field with physical barrier. These figures suggest that using the first 4 modes will result in a sufficiently accurate approximation of the covariance in both KL-expansions. Additionally, the retained energy in the first 4 modes as a fraction of the total energy $E_{frac} = \sum_i^M \lambda_i^2 / \sum_i^{Nquad} \lambda_i^2$ is computed to check if this truncation indeed gives an accurate approximation. For the field without physical barrier, E_{frac} is found to be 0.997, so $> 99\%$ of the total energy is retained in the first 4 modes. For the field with physical barrier $\approx 100\%$ of the total energy is retained in the first 4 modes ($E_{frac} = 0.99998$). This strengthens the assumption that the use of the first 4 modes will give a sufficiently accurate approximation of the covariance in both KL-expansions.
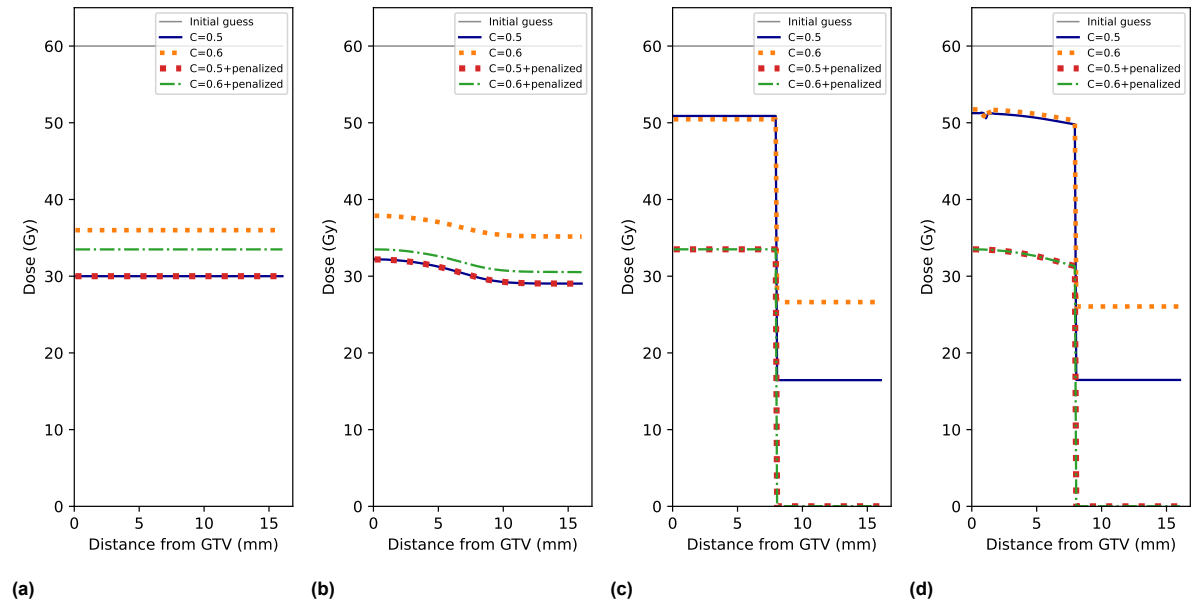
Figure 5.9: Optimized dose distributions as a function of the radius for the ETCP model using 5000 realizations of the tumor cell density field $\hat{\rho}$. The different figures correspond to the different input mean tumor cell density fields μ_ρ (Figure 4.2) for energy constraint $C = 0.5$ and $C = 0.6$ for the unpenalized model and $C = 0.5$ for the penalized model. **(a)** Tumor cell density field with a constant mean, **(b)** Tumor cell density field with a Gaussian decreasing mean, **(c)** Tumor cell density field with a constant mean and a physical barrier, **(d)** Tumor cell density field with a Gaussian decreasing mean and a physical barrier.

Figure 5.9 shows the optimized dose distributions for the different KL-models. The first two plots correspond to the volumes where no physical barrier was present and the last two plots correspond

to the volumes where a physical barrier was simulated after which no tumor cells can be found. For each volume, the results are plotted for 2 different energy constants (C = 0.5 and C = 0.6) for both the unpenalized model and the penalized model.

5.3.1. Volumes without physical barrier

Constant mean

Figure 5.9a shows the optimized dose distributions for a volume for which a constant mean tumor cell density was assumed to create the KL-expansion model of the random tumor cell density field. The corresponding ETCP values and the used energy (percentage of the maximum allowed energy) are tabulated in Table 5.5. As can be expected for a field with a constant mean tumor cell density, the optimized dose distributions are constant throughout the volume.

For the unpenalized model, it is clear that the dose increases if the energy constant is increased. The maximum allowed energy is used by the dose distribution for both energy constraints. By increasing the energy constraint from 0.5 to 0.6, the ETCP value increases vastly from 0.493 to 0.999. For the lower energy constraint, the allowed maximum energy is clearly not enough to obtain a satisfying tumor control, but by increasing the energy constraint slightly, almost full tumor control is achieved.

For the penalized model, the ETCP and organ overdose were weighted equally. The resulting penalized dose distribution for C = 0.5 is equal to that of the unpenalized model: the dose distributions overlap and the yielded ETCP values are equal. This is to be expected as the ETCP value for the unpenalized model was already quite low and therefore penalizing organ overdose can not push the dose further down without yielding a low ETCP value. For the slightly higher energy constant C = 0.6 the penalized dose distribution is lower than for the unpenalized model and 93.4% of the allowed energy is used in the penalized distribution. The ETCP value is 0.985. The penalty thus allows for a drop in the deposited energy, while maintaining a high tumor control.

Table 5.5: Optimized ETCP values and used energy as a percentage of the maximum allowed energy for two energy constraints C = 0.5 and C = 0.6 for both the penalized and the unpenalized KL model with a constant μ_ρ.

Energy constraint	Penalized	ETCP	Energy (%)
C = 0.5	No	0.493	100
	Yes	0.493	100
C = 0.6	No	0.999	100
	Yes	0.985	93.4

Gaussian decreasing mean

In Figure 5.9b the results for the KL-model where the tumor cell density field in the volume was assumed to have a Gaussian decreasing mean are shown. The corresponding ETCP values and used energy can be found in Table 5.6. The optimized dose distributions all follow a similar pattern where the dose decreases over the distance up to a certain point, after which the dose appears to stay constant throughout the rest of the volume. This is consistent with the shape of the tumor cell density field realizations, as the input mean of the field decreases to 0 mm^{-3}, but for many realizations, the tumor cell density in the volume at a distance of 10-16 mm from the GTV is > 0 mm^{-3}. Furthermore, in all the field realizations the tumor cell density was set to 0 mm^{-3} where the simulated tumor cell density was negative. This slightly skews the mean of the realizations away from 0 mm^{-3}. To gain proper tumor control in this area, the optimization pushes the dose distribution to a constant dose, that is slightly lower than the optimized dose values for the constant μ_ρ.

By optimizing the ETCP objective based on the uncertainty of Δ (Section 5.1), the dose got pushed to the maximum in as large a volume as possible. This behavior is explained by the fact that giving up dose in the high probability areas would result in a much larger decrease in the ETCP, than giving dose to the low probability areas would result in a gain in ETCP. This effect of pushing the dose to the maximum for as large a volume as possible is not present here. As evidenced by the example realizations of the tumor cell density field in Figure 4.2d (second plot from the top), a significant number of these tumor cell density fields have a tumor cell density > 0 mm^{-3}. Specifically, the tumor cell density in this area can range from 0 up to $\approx$ 40 mm^{-3}. In this case, giving more dose to the area with a higher mean tumor cell density (before $\approx$ 10 mm) and decreasing the dose after $\approx$ 10 mm results in a large

decrease in the ETCP, as any underdosage in that area severely decreases the ETCP.

For the unpenalized model, the dose distribution at the lower energy constraint C = 0.5 has a good tumor control with an ETCP of 0.930.The dose distribution again shifts up as the energy constraint is increased to 0.6 and the corresponding ETCP increases from 0.930 to 1.00. For both energy constraints, the optimized dose distribution uses the maximum allowed energy.

Table 5.6: Optimized ETCP values and used energy as a percentage of the maximum allowed energy for two energy constraints C = 0.5 and C = 0.6 for both the penalized and the unpenalized KL model with a Gaussian decreasing μ_ρ.

Energy constraint	Penalized	ETCP	Energy (%)
C = 0.5	No	0.930	100
	Yes	0.930	100
C = 0.6	No	1.00	100
	Yes	0.986	87.7

Just like for the constant mean KL model, for C = 0.5, the optimized dose distributions of the penalized model and the unpenalized model overlap and both have an ETCP of 0.930. For C = 0.6, the dose distribution of the penalized model drops almost to the dose distribution of C = 0.5 and has an ETCP value of 0.986. It uses 87.7% of the maximum allowed energy. The dose values are only slightly higher than the dose values for C = 0.5, so the deposited energy is slightly higher, while the ETCP is increased from 0.930 to 0.986. In comparison to the unpenalized model with C = 0.6 the penalty maintains a high tumor control, while allowing a decrease in deposited energy.

5.3.2. Volumes with physical barrier

Constant mean

The results for the KL-model with a constant mean tumor cell density and an imposed physical barrier after which the tumor cell density is 0 are shown in Figure 5.9c. The corresponding ETCP values and energy as a percentage of the maximum allowed energy are shown in Table 5.7. As is expected for a tumor cell density field with a physical barrier after which the tumor cell density drops to 0 mm^{-3}, the optimized dose distributions all follow the same pattern of a constant dose up until a drop-off point and again a constant dose after that drop-off. The drop-off point is located at 8 mm, which is the distance at which the physical barrier was placed.

For the unpenalized model, the dose distributions for both energy constraint constants have similar dose values up to the drop-off point. After the drop-off point, the dose is constant and it is higher for C = 0.6, than for C = 0.5. This is a direct effect of the higher maximum allowed energy, as for both results, 100% of the allowed energy is used. Both dose distributions have a ETCP value of 1.00. It must be noted that the dose before the drop-off is much higher than the optimized dose in Figure 5.9a, even though the tumor cell density is equal in this area for both the constant mean model and the constant mean with physical barrier model. Furthermore, the dose does not drop to 0 Gy after the drop-off even though it would be expected that no dose is necessary in this area due to a tumor cell density of 0 mm^{-3}. This can both be explained by the fact that the gradient is ≈ 0 in both the area before and after the drop-off, blocking the optimizer to push the dose down further.

Using the penalized model, the dose distributions for both energy constraint constants are equal and constant up to the physical barrier. The dose values drop down to 0 Gy after the physical barrier. The corresponding ETCP values are 0.993 for both energy constraint constants, which is only slightly lower than for the unpenalized model. As the dose distributions are equal, the same amount of energy is deposited in either case. This corresponds to 43.9% of the maximum allowed energy for an energy constraint constant C = 0.5 and 36.6% of the allowed energy for C = 0.6. The penalty allows the optimizer to push the dose values down to a much lower dose level before the physical barrier and to 0 Gy after the drop-off, without a significant loss in the ETCP value.

Gaussian decreasing mean

The results for the KL-model with a Gaussian decreasing mean tumor cell density and an imposed physical barrier after which the tumor cell density is 0 are shown in Figure 5.9d. The corresponding ETCP values and energy as a percentage of maximum allowed energy are shown in Table 5.8.Just like for the constant mean model, the dose drops off at 8 mm, where the physical barrier was placed.

Table 5.7: Optimized ETCP values and used energy as a percentage of the maximum allowed energy for two energy constraints $C = 0.5$ and $C = 0.6$ for both the penalized and the unpenalized KL model with a constant μ_ρ and an imposed physical barrier.

Energy constraint	Penalized	ETCP	Energy (%)
$C = 0.5$	No	1.00	100
	Yes	0.993	43.9
$C = 0.6$	No	1.00	100
	Yes	0.993	36.6

Furthermore, before the drop-off, the dose distributions follow the same decreasing pattern as the results for the model with a Gaussian decreasing mean without physical barrier.

Using the unpenalized model to optimize the ETCP, the dose values for both energy constraint constants are approximately the same before the drop-off. After the drop-off the dose distributions are similar to the results for the constant mean with physical barrier (Figure 5.9c). Again the dose is constant beyond the physical barrier and the dose is higher with $C = 0.6$ than with $C = 0.5$ due to more energy being allowed to be deposited in the volume (in both cases almost all of the allowed energy is used). The corresponding ETCP is 1.00 for both energy constraints. The dose before the drop-off is much higher than in Figure 5.9b, despite the tumor cell density being the same in this area for the model with and without physical barrier. The dose after the drop-off is not 0 Gy, although this would be expected as the tumor cell density is 0 mm^{-3} in this area. These problems are equal to those for the model with constant mean and a physical barrier and are caused by the gradient values being ≈ 0 throughout the volume.

When the penalized model is optimized, the dose distributions for both energy constraints are equal and slowly decrease up until the drop-off. After the drop-off the dose is 0 Gy, as is expected as the tumor cell density in this area is also 0 mm^{-3}. The corresponding ETCP values are 0.994 for both energy constraint values. This is only slightly lower than for the unpenalized model. However, the amount of used energy is significantly decreased, from 99.8% to 42.8% and 35.7%, for $C = 0.5$ and $C = 0.6$, respectively. The actual amount of used energy is the same for both energy constraint constants, as the dose distributions are equal. Due to the penalty on the ETCP objective, the optimizer is thus able to push the dose values down to a lower dose level before the drop-off and to 0 Gy after the drop-off, without a significant loss in the ETCP value.

Table 5.8: Optimized ETCP values and used energy as a percentage of the maximum allowed energy for two energy constraints $C = 0.5$ and $C = 0.6$ for both the penalized and the unpenalized KL model with a Gaussian decreasing μ_ρ and an imposed physical barrier.

Energy constraint	Penalized	ETCP	Energy (%)
$C = 0.5$	No	1.00	99.8
	Yes	0.994	42.8
$C = 0.6$	No	1.00	99.8
	Yes	0.994	35.7

KL-model for CTV optimization

In this section, the results of optimizing the objective based on the Karhunen-Loève model as derived in Section 4.6 were discussed. It was shown that realistic optimized dose distributions can be obtained for different types of tumor cell density fields. The optimized dose distribution for fields where there are tumor cells throughout the volume (without physical barrier), show that dose is necessary throughout the volume, as is expected. If the input mean μ^ρ follows a Gaussian decreasing function, the resulting dose distribution also follows a decreasing pattern up until a point from where the dose is constant. The results for the fields where a physical barrier was imposed in the volume, resemble the results that were obtained for the normal ETCP objective as discussed in Section 5.2, with a drop-off at a certain point. The location of this drop-off is steerable when the KL model is used to simulate the tumor cell density field, while this is not the case for the normal ETCP objective.

<div style="text-align: right; font-size: 3em;">6</div>

Conclusions

6.1. Comparison to previous results

In Section 5.1, it was shown that the optimal dose distribution obtained by optimizing the ETCP is the maximum dose for as large a volume as is allowed by the energy constraint and a dose of 0 Gy in the rest of the volume. This is due to the multiplicative nature of the TCP. If any part of the volume does not receive enough dose, the ETCP quickly drops towards 0. By giving the maximum dose to as large a volume as possible, the optimizer avoids such a scenario. The optimizer however has a hard time reaching this optimal dose distribution as the gradient values in the volume become very small. This is the case both if the TCP in a shell approaches 1 and if it approaches 0 and is a result of the fact that the TCP is a sigmoidal function of the dose. It is shown that by scaling the optimization objective, the optimization can be pushed further towards the optimal dose distribution. The results from a previous study were also shown, which display a slowly decreasing curve for the dose distribution with the highest dose close to the GTV. A mistake was found in the model that was used in this study and these results could not be replicated after this mistake was fixed. Although the dose distributions from the previous study did obtain a high ETCP (of around 0.98) and therefore can yield proper tumor control, the dose distributions are not optimal.

6.2. Results for the different tumor sites

In Section 5.2, the expected TCP and expected LTCP were investigated as optimization objectives for four different tumor sites with different tumor parameters and different maximum distances for the MDE Δ_{max}. Different results were obtained for the four tumor sites, where both brain and breast had similar results and similarly, lung and prostate also yielded similar optimized dose distributions. When the ETCP is used as an objective, the optimized dose distribution has a drop-off point in the volume after which the dose dropped significantly for all 4 tumor sites. This drop-off point is related to the energy constraint as the volume that receives the maximum dose is determined by the maximum energy that is allowed to be deposited ($\approx$ 100% of this allowed energy is used for all the tumor sites). When the ELTCP is used as an objective, the optimizer gives dose throughout the whole volume. This is due to the logarithmic TCP, which becomes very large if the TCP comes close to 0. Such situations are thus avoided by the optimizer, by giving as much dose as possible even to the low MDE probability regions of the investigated volume. A slight decrease is present in the optimized dose distributions, which is credited to the small effect of the probability distribution $P_\Delta(\Delta)$ on the optimization. The ETCP optimization is sensitive to the maximum radius of the investigated volume. The larger the investigated volume, the more difficult it is to optimize the dose in the shells far away from the GTV.

A penalized version of the expected TCP was also investigated for the different tumor volumes. This penalized model uses the squared overdose as a penalty in the irradiated volume, which also contains healthy tissue. A penalty weight can be assigned to balance the maximization of the ETCP and minimization of the squared overdose. The optimized dose distributions resulting from the penalized ETCP objective have dose in a much smaller part of the volume than for the unpenalized ETCP objective. Furthermore, the dose is pushed to 0 Gy beyond the drop-off, as the gradient of the penalty helps push the dose down to 0 Gy when the gradients from the ETCP are too small to drive the optimization. The

ETCP values that correspond to these dose distributions still show that proper tumor control can be achieved even when the dose is 0 Gy in most of the volume. Using different weight factors allows for steering of the balance between maximizing the tumor control and minimizing the damage to the healthy tissue in the volume surrounding a tumor. However, as described in Subsection 5.2.2, the penalized model is dependent on the location of the quadrature points used for the discretization of the integral over Δ. By varying the penalty weight, drop-off points were only found at certain shells, related to the location of the quadrature points in the investigated volume. Ideally, a drop-off point could be located at any shell in the volume so that there is a direct linear relation between the assigned penalty weight and the distance of the drop-off point. The limited number of quadrature points in the investigated volume is what currently prevents this direct linear relation.

6.3. KL-expansion model

In Section 5.3, a novel approach to probabilistic treatment planning for CTV uncertainties is investigated. A new ETCP based objective was derived, where the uncertainty of the CTV is assumed to be the tumor cell density field. This tumor cell density field is simulated using a Karhunen-Loève expansion. For the demonstration, 4 different CTV models were created, with a constant mean or a Gaussian decreasing mean and either a physical barrier or no physical barrier present. Optimizing the ETCP for 5000 realizations of these 4 different models resulted in realistic dose distributions. It was shown that by slightly increasing the energy constraint constant, high ETCP values could be obtained for all models. Furthermore, when a penalized ETCP objective was used, high tumor control was maintained while the used energy was decreased. The different models give an example of the variety of tumor cell density fields that can be simulated using the KL-expansion method and the realistic dose distributions are a promising outcome for the applicability of the KL-expansion method for the probabilistic treatment planning to deal with CTV uncertainties.

6.4. Future research

6.4.1. Different tumor sites

ETCP-based and ELTCP-based optimization was investigated for four tumor sites, namely brain, breast, lung and prostate. It was shown that for different tumor parameters and different maximum distances of the MDE, different optimized dose distributions are obtained. However, only a single set of tumor parameters was investigated for each tumor site and for future research it is recommended to zoom in on each tumor site separately to investigate different values for α and β. In a previous study [9], uncertainties in α and β were included in the ETCP-model similarly to how the uncertainty in ρ is included in the current model. There it was found that these uncertainties had little influence on the results, but the model from [8] was used for the study. As we now know that this model was incorrect, the influence of the uncertainties in α and β on the optimization should be investigated again.

Furthermore, a penalized ETCP objective was investigated for the different tumor sites as well. Future research should focus on this penalized objective as it allows for control over the balance between tumor control and normal tissue sparing. Further investigations into the optimal weight factors for the penalty should be performed based on advice from radiologists and treating clinicians. Additionally, to solve the problem related to the limited number of drop-off points, two different approaches can be used. Firstly, one could increase the number of quadrature points to approximate the integral over Δ. This will lead to an increase in the number of possible drop-off points. However, a large downside of increasing the number of quadrature points is that it will lead to a significant increase in the required time for the ETCP computation. Using an explicitly truncated distribution for $P(\Delta)$ could help to avoid a large increase in computation time. Secondly, another numerical integrator could be used, where one has more control over both the number and location of quadrature points in the investigated volume. In the current method, the Gauss-Laguerre quadrature, a large number of quadrature points is located outside the investigated volume, and therefore it is inefficient when the investigated volume is relatively small.

6.4.2. KL-expansion model

The results for the optimization of the KL-expansion model were promising, but there are some limitations to the results that can be addressed in future research.

For the demonstration of the KL-expansion model, only a single value for the standard deviation of the tumor cell density field was used. Furthermore, only a single correlation length of the autocorrelation function was investigated. The effect of these values on the simulated tumor cell density field and subsequent optimized dose distributions should be investigated.

Currently, the ETCP in the KL-model is computed using 5000 realizations of the tumor cell density field. A more robust way to compute the ETCP would be to use cubatures to perform multidimensional integration over all the random variables ξ_i that are used to compute $\hat{\rho}(,\theta)$, the KL-approximation of the tumor cell density field (Equation 4.36). Cubatures are the multidimensional equivalent of the quadratures that were used in this study. It is recommended to use this approach for future investigations into the KL-model to improve the accuracy of the model and potentially speed up calculation time.

The KL-expansion can be used to create different models of the microscopic disease area. As shown in this thesis, such a model can have a physical barrier present in the volume. Other shapes of the mean tumor cell density $\mu^\rho(r)$, such as a tumor cell density field that decreases linearly over the distance, can be designed and investigated as well.

Furthermore, more explicit data on the distribution of microscopic disease groups in the microscopic disease area could help to improve the KL-model. Such data can be used to improve the inputs of the model such as the shape of the mean tumor cell density $\mu^\rho(r)$ and the standard deviation $\sigma^\rho(r)$ of the tumor cell density field $\rho(r,\theta)$. The histopathological studies that were found and discussed in Appendix A only reported the maximum distance where microscopic disease was found. To create accurate models of the microscopic disease, more explicit data on the location and size of the microscopic disease groups would be helpful. For this, new histopathological studies need to be performed or the explicit data from already performed studies should be made available.

Finally, we investigated a 1D version of the KL- model, but the KL-model is well-suited to be extended into a three-dimensional model to simulate more complex tumor cell density fields. An example of a more complex three-dimensional field is a CTV where the tumor cell density might be high in one direction over a large distance from the GTV, while in another direction there is a physical barrier present and the tumor cell density field therefore extends only slightly from the GTV. For this, a three-dimensional model of the tumor and the surrounding microscopic disease area build up out of voxels will need to be created to replace the one-dimensional model based on volume shells. With a 3D-model, the four different tumor sites and their differences in microscopic disease can be investigated in more detail. Different spatial data on the extension of microscopic disease was identified in Appendix A for the different tumor sites. This data could be used to model the input mean tumor cell density field to reflect the differences in the tumor cell density field in the different directions outwards from the GTV.

6.4.3. Use of the probabilistic models in practice

In this thesis, conceptual 1D-models incorporating the uncertainties in the microscopic disease area were investigated with the goal of probabilistic treatment planning to replace the CTV margin. To apply these models in practice, the investigated objective functions need to be implemented into treatment planning systems. As treatment planning systems typically allow for multi-criteria optimization, a probabilistic objective can be implemented as a cost function alongside cost functions on for example the OARs. It is possible to use the 1D-models in a treatment planning system, despite the fact that the TPS creates dose distributions on three-dimensional patients scans. The volume domain here is divided into voxels and the distance of each voxel can be calculated to the edge of the PTV. This distance can then be used as r for the probabilistic model. The treatment planning system will optimize the dose per voxel, instead of per volume shell. In this manner, the investigated models could already be used to investigate probabilistic treatment planning in real patient plans. When a three-dimensional model is created, the implementation of such a model could be even more straight-forward as it is already a voxel-based model. To gain optimal insight in the use of these probabilistic models in practice, it is important to involve clinicians and radiologists to gain a clinical perspective on the used parameters, such as the penalty weight for balance between tumor control and normal tissue sparing and on the resulting optimized dose distributions.

Both the model based on the uncertainty in the extension of the microscopic disease and the KL-model based on the uncertainty in the tumor cell density field have been shown to allow for achieving good tumor control in the microscopic disease area, and therefore probabilistic treatment planning shows to be a promising alternative to the binary CTV margins that are currently in practice. Further investigation of the KL-model using conceptual geometries will improve the probabilistic optimization,

but it is recommended to simultaneously investigate the use of the probabilistic objective functions in actual real patient plans. This will allow for direct feedback on the clinical applicability of the objective functions.

Probabilistic treatment planning was investigated for four tumor sites. These four tumor sites were chosen as the most histopathological data was present for these sites. In future research, the use of the probabilistic objective functions can be investigated for other tumor sites as well.

A
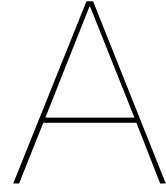
Literature study

A.1. Histopathological and radiological MDE studies for different tumor sites

As discussed in Chapter 1, there is a possibility of microscopic disease in the area surrounding a tumor. Due to limitations in the imaging modalities, this microscopic disease is not visible on CT or MRI scans [4, 5]. To assess the microscopic disease extensions, histopathological examinations of surgical specimens are thus essential to obtain information about the distance up to which MDE can be found, to be able to determine appropriate CTV margins.

In the search for literature on the distance of microscopic disease extensions , studies on MDE were identified for different tumor sites: brain, breast, lung and prostate. The results of the literature search will be presented here.

For MDE studies to be useful for probabilistic treatment planning (Chapter 3), it is important to have an idea of which data is reported in the literature and how this data was acquired. For some tumors, the microscopic disease might be more prevalent in a certain direction from the tumor than others. For example, a large percentage of the MDE might be found in the posterolateral direction from the Gross Tumor Volume. Such a preference for a certain direction could be included into probabilistic treatment planning. Furthermore, there is a potential for shrinkage of the tumor between freshly excised tumor specimens and tumor specimens after fixation [35–40]. It is therefore important to check if a correction is used for the tumor shrinkage, when the microscopic disease distance is measured. Finally, to be able to properly compare the MDE distance data from different studies, it is also important to keep in mind how big the specimens were that were investigated. If one study uses a surgical margin of 1 cm, while in another study whole-organ specimens were investigated, there could be a difference in the range of the MDE distance that is found. The former study might have a smaller maximum MDE distance than the latter study, which could be due to a smaller area being investigated.

A.2. Brain cancer

The main treatment for primary brain cancer is surgery followed by radiotherapy to a volume surrounding the original tumor bed and often additional chemotherapy is also given to the patient [41–43]. To determine the clinical target volume for irradiation of the tumor bed and surrounding tissue, studies on microscopic disease extension are essential.

Two types of studies on microscopic disease in brain cancer were found in the literature, a histopathologic brain autopsy study and recurrence pattern studies. In histopathologic brain autopsy studies, the microscopic disease extensions are measured in microscopic slices of brain tissue [44]. In recurrence pattern studies, CT or MRI scans of patients with recurrent brain cancer are studied and it is assumed that the recurrent tumors are the result of microscopic disease left behind after the treatment of the original tumor by surgery and radiation therapy [45–47]. The MDE distance is then evaluated by measuring the distance from the original tumor to the recurrent tumor.

A.2.1. Histopathologic study

In 1988, microscopic disease extension was studied by Burger et al. [44]. In this study, the brains of 15 adults that were diagnosed with glioblastoma multiforme (the most common form of primary brain cancer [44, 48]) were obtained through autopsy. The authors determined the maximum distance from the edge of the original tumor where tumor cells could be identified. This was done in a 1.0-2.0 cm thick two-dimensional section of the brain. The maximum reported MDE was 5.0 cm. Furthermore, MDE could be found at a distance larger than 2 cm from the tumor visible on CT in 3/15 patients (20%) and in 2/15 patients (13%) the MDE was larger than 3 cm, this distribution is plotted in Figure A.1.
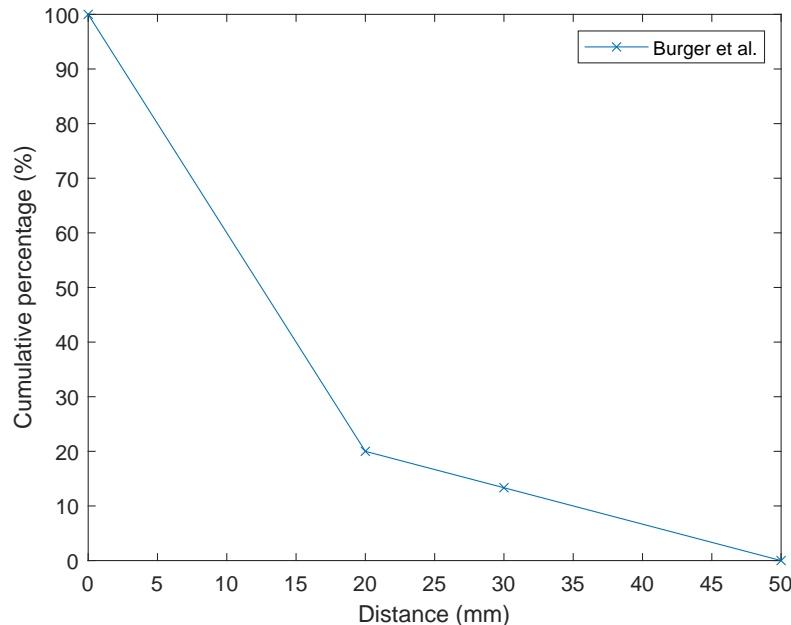
Figure A.1: Probability of finding microscopic disease beyond a certain distance from the macroscopic tumor visible in CT scans in patients with glioblastoma; the maximum microscopic disease distance was measured in brain autopsy sections [44].

A.2.2. Recurrence pattern studies

Wallner et al. [45] studied recurrence patterns in 34 patients using CT scans of the initial and recurrent tumor. All patients underwent surgery to remove their primary tumor and received subsequent whole-brain radiation. Twenty-seven patients also received chemotherapy. Twenty-five patients received an additional radiation boost to the tumor bed. Of the 34 patients, 2 patients initially had multiple tumors. The authors reported the results from these patients separately from the other 32 patients. Of the patient with only a single tumor, 16% recurred within the tumor bed of the original tumor, 65% recurred within 1.0 cm from the original tumor and 78% recurred within 2.0 cm. The maximum observed distance between original and recurrent tumor was 9.2 cm. This patient recurred in the opposite side of the brain. Of the two patients with multiple tumors, one patient recurred within 1.0 cm from the original tumor volume and the other recurred more than 2.0 cm from the initial tumor volume. The exact maximum distance is provided for each of the 34 patients in a figure showing their recurrence patterns and a cumulative distribution of this data is plotted in Figure A.2.

In a study by Gaspar et al. [46], recurrence patterns were investigated using CT scans of 70 patients. All patients had surgery to remove the tumor and subsequent whole-brain radiation in combination with an additional radiation boost in the area surrounding residual tumor visible on the postoperative CT scan. In 51/70 (73%) patients, a recurrent tumor was found in the brain at follow-up (at least 18 months after radiation therapy). The maximum distance between the original tumor visible on the preoperative scan and the recurrent tumor was found to be 4 cm. 96% (49/51) of the tumors recurred within 2 cm from the original tumor, 98% (50/51) recurred within 3 cm and all 51 of the recurrences within the brain recurred within 4 cm from the original tumor. This data has been plotted in Figure A.2 in adapted form.

Aydin et al. [47] investigated recurrence patterns in 46 patients using CT or MRI scans. In all

patients, the tumor was removed surgically and subsequent local radiotherapy was given to a clinical target volume with a margin of 2 to 3 cm beyond the original tumor visible on the preoperative CT scan. The maximum distance between the original tumor on the preoperative CT scan and the recurrent tumor was ≤ 2 cm in 73.9% of the patients (this value is incorrect, see Subsection A.2.3) and ≤ 3 cm for 93.5% of the patients. The exact maximum distance for each of the 46 patients was given by the authors in a figure containing the 46 recurrence patterns and a cumulative distribution of this data is plotted in Figure A.2.
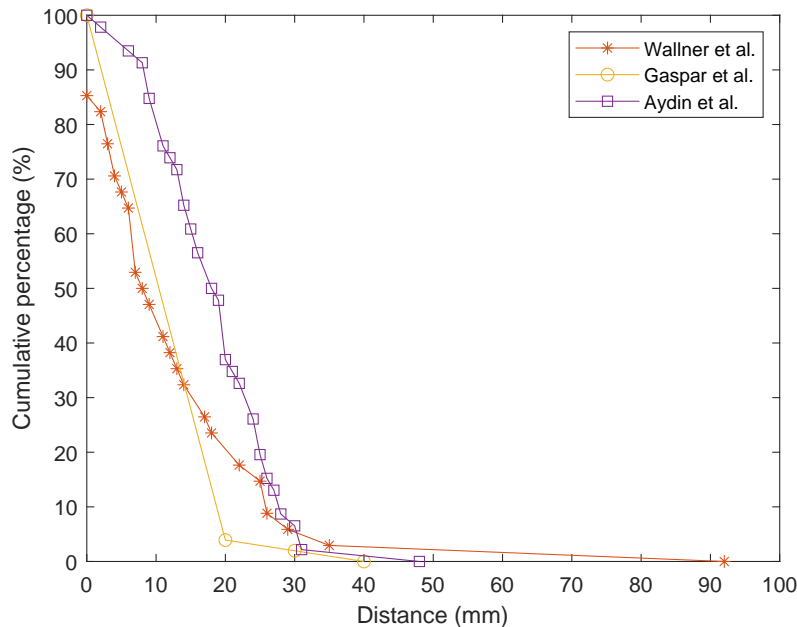
Figure A.2: Probability of finding microscopic disease beyond a certain distance from the macroscopic tumor in patients with brain cancer, determined from recurrence studies [45–47]. In these studies, the maximum microscopic disease distance was assumed to be equal to the maximum distance of a tumor recurrence from the original tumor.

A.2.3. Brain MDE data

An overview of the literature findings for microscopic disease extension in brain cancer is summarized in Table A.1 and a plot of the cumulative distributions obtained from the different studies is presented in Figure A.3.

Table A.1: Overview of the literature findings on MDE in brain cancer: the number of patients with MDE vs. the total number of studied patients, the mean/median MDE distance, the range of MDE, whether any spatial information was provided and whether a shrinkage factor was used. - indicates that this variable is not provided by the authors; * indicates that the variable was computed from data provided by the authors; † indicates that here 'MDE patients' is set equal to patients with recurrences that occured at least partly outside of the original tumor bed and 'total patients' equals the amount of patients with a recurrences; / indicates that this variable is irrelevant (no histopathological study).

	Burger et al. [44]	Wallner et al. [45]	Gaspar et al. [46]	Aydin et al. [47]
MDE patients/total patients (%)	15/15 (100)	29/34 (85) †	-/51 (-) †	46/46 (100) †
MDE distance (mm)	-	-	-	-
		Mean: 15.9 *		Mean: 17.9 *
MDE range (mm)	Maximum: 50	0-92	0-40	2-48
Spatial information provided	Yes (transverse plane)	Yes (transverse plane)	No	Yes (transverse plane)
Shrinkage factor	Yes	/	/	/

In Table A.1 it is noted that none of these studies reported a mean or median value of the MDE

distance. From the exact data that was provided by Wallner et al. [45] and Aydin et al. [47], the mean MDE distance was computed to be 15.9 mm and 17.9 mm, respectively. As the maximum MDE distance reported in these studies was 92 and 48 mm, respectively, these mean values seem to be in reasonable agreement with each other and the maximum MDE distance of 92 mm could be seen as an outlier.

The investigated area in both the histopathological study and the recurrence studies is mainly in the transverse plane. In Burger et al. [44], whole-brain sections in the transverse plane were investigated. This means that it is likely that the entire extent of the microscopic disease was found in the transverse plane. A limitation of this study is that these whole-brain sections were obtained from a 1.0 to 2.0 cm thick brain section through the tumor, so microscopic disease in the cranio-caudal direction outside this brain slab might have been missed. In the recurrence studies [45–47], CT slices were used to measure the MDE. Such slices are in the transverse plane. The pre-operative CT slices with the maximum initial tumor size were superimposed with anatomically comparable CT slices from the recurrent tumor. From this the maximum distance between the border of the recurrent tumor and the initial tumor was measured. This means that the maximum distance was measured in the transverse plane, but the distance in the cranio-caudal direction was not evaluated. To conclude, both the histopathological study and the recurrence studies did not investigate the MDE in the cranio-caudal direction and therefore it is possible that the maximum distance of microscopic disease is underestimated.

In the histopathological study from Burger et al. [44] the authors corrected for tissue shrinkage, as they had found in a previous study [35] that tissue shrinkage ranged from 10% to 17%.

In three of the studies (Burger et al. [44], Wallner et al. and Aydin et al.) maps were drawn for all the patients, indicating the extent of the MDE in the transverse plane. These maps could be used to infer spatial information about the MDE. From visual inspection of these maps, it can be concluded that in the transverse plane there is no preference for microscopic disease to extend in a specific direction.
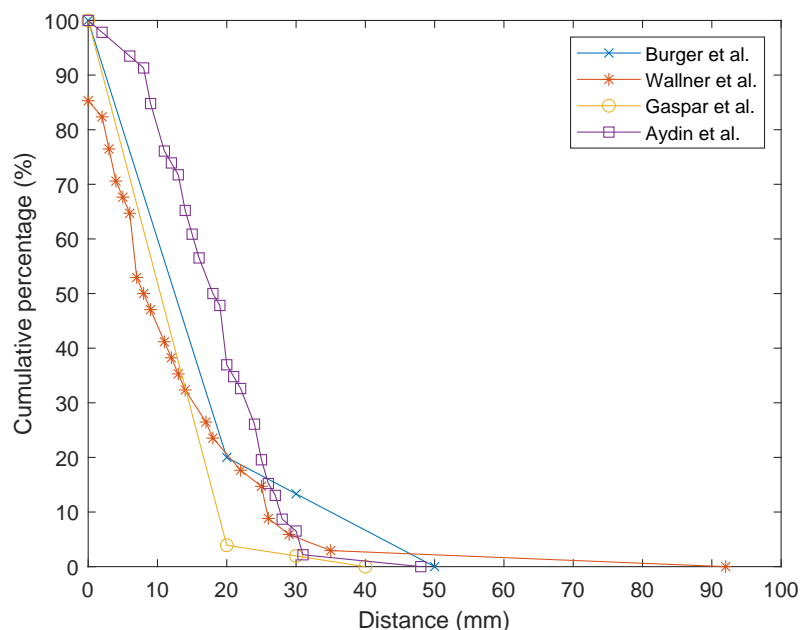
Figure A.3: Probability of finding microscopic disease beyond a certain distance from the macroscopic tumor in patients with brain cancer, determined from brain autopsy sections [44] or from recurrence studies [45–47]. In the recurrence studies, this distance was assumed to be equal to the maximum distance of a tumor recurrence from the original tumor.

It is important to note that the recurrence studies might be biased towards patients that are more sensitive for recurrence. All of the patients included in these studies were treated with radiotherapy after the surgery. Aydin et al. [47] and Wallner et al. [45] only included patients that had a recurrence, despite their treatment. No information was provided on how many patients did not have a recurrence over the course of the study. It is possible that in all these excluded patients, the microscopic disease was either not present or so close to the GTV, that it was treated by the radiotherapy. Gaspar et al. [46] did include information on how many patients did not have a recurrence. The MDE distance information

that was provided by the authors however is not very extensive. Furthermore, it is not disclosed how many of the recurrent tumors recurred within the original tumor bed, only how many of the tumors recurred within 2, 3 and 4 cm from the original tumor.

Finally, the cumulative distributions for the different studies are plotted in Figure A.3. A general trend is visible in the decrease of the probability of finding microscopic disease beyond a certain distance from the macroscopic tumor. The data from the histopathological study is relatively well in agreement with the recurrence studies. The cumulative distribution from Aydin et al. indicates a probability of 37% to find MDE beyond 20 mm from the macroscopic tumor. This corresponds to 63.0% of the patients having a recurrence within 2 cm from the original tumor, contradicting the 73.9% the authors reported (Subsection A.2.2). As the cumulative distribution was computed from the raw distance data provided by Aydin et al. it is clear that the authors reported an incorrect value in their study and further investigation of the raw data leads to the conclusion that the reported value of 73.9% is the percentage of patients within 2 cm after the raw distance data is rounded to whole centimeters. The reported value for patients with a recurrence within 3 cm (93.5%), however is based on the unrounded values and corresponds to the probability of finding MDE beyond 3 cm of 6.5%, as in Figure A.3. Finally, caution is warranted when combining the MDE data from the histopathological study with the data from the recurrence studies, as these are retrieved in a completely different way and therefore are not directly comparable.

A.3. Breast cancer

For patients with early-stage breast cancer, there are two common therapies: mastectomy, where the whole breast is removed [49] and breast-conserving therapy (BCT). Breast-conserving therapy consists of surgery to excise the tumor, known as lumpectomy or wide local excision, and subsequent whole-breast irradiation (WBI) [26, 27, 49]. Typically, a surgical margin of at least 1 cm is used during lumpectomy [26, 27, 50]. After surgery, the whole breast is irradiated with 50 Gy and an additional radiation boost of 10 to 26 Gy is given to the excision site and the surrounding tissue to account for microscopic disease extension [27, 51, 52]. The radiation boost has an impact on the cosmetic outcome [53], therefore it is important to optimize the size of the boost that allows adequate MDE coverage without compromising the cosmetic outcome. To assess the extension of microscopic disease, histopathological studies have been carried out on mastectomy and lumpectomy specimens to determine the optimum clinical target volume for the boost.

A.3.1. Histopathological studies

In 1985, Holland et al. [54] studied the presence of microscopic disease in 282 mastectomy specimens. Of these, 177 (63%) specimens displayed microscopic disease in the tissue surrounding the macroscopic tumor. In 56/282 (20%) the MDE did not extend further than 2 cm from the macroscopic tumor, whereas in 121/28 (43%) the maximum MDE was larger than 2 cm from the macroscopic tumor. The range of microscopic tumor spread was reported to be 0-10 cm. More specific distance data up to 10 cm for macroscopic tumors with a size of maximum 4 cm (tumors larger than 4 cm are not admissable for BCT [50, 54]) was provided in a plot, and has been reproduced in Figure A.4.

Faverly et al. [50] studied tumor spread in 135 mastectomy specimens of patients who might have been eligible for BCT. They measured the distance between the edge of the macroscopic tumor and the identified MDEs. They simulated surgical margins of 1, 2 and 3 cm and reported the percentage of specimens that would have residual microscopic disease after BCT with these surgical margins. It was reported that 47% of the breasts had microscopic disease beyond 1 cm from the macroscopic tumor, 39% had residual MDE beyond 2 cm and 22% of the specimens had residual disease beyond 3 cm from the macroscopic tumor. This distribution is plotted in Figure A.4.

A large study on 333 reexcision specimens by Vicini et al. in 2004 [55] studied the maximum disease extension from the edge of the original lumpectomy specimens into the reexcision specimen of patients receiving BCT. A reexcision is performed when microscopic disease is found on the edges of the initial excision specimen. Of the 333 specimens, 214 (64.3%) had residual microscopic disease in the reexcision specimen. The mean and median distance of MDE was 7.9 and 6.0 mm, respectively. The reported range was 1.0-29.0 mm. A more specific distribution of the MDE was reported in the text and is plotted in Figure A.4.

Stroom et al [27] investigated the extension of microscopic disease in patients receiving BCT. They
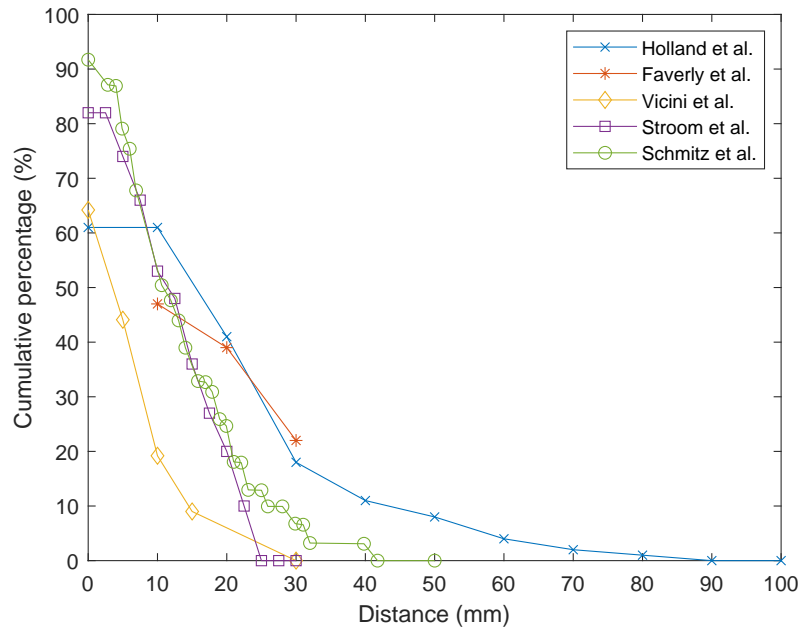
Figure A.4: Cumulative distribution of the probability of finding microscopic disease beyond a certain distance from the macroscopic tumor in patients with breast cancer for different histopathological studies [26, 27, 50, 54, 55].

studied 38 lumpectomy specimens from BCT patients and found microscopic spread in 31 of the 38 specimens. The authors measured the distance from the macroscopic tumor to the microscopic disease and noted the orientation of the microscopic finding relative to the macroscopic tumor in the breast. They found that the distribution of microscopic spread is isotropic in the three main directions (nipple-lateral, left-right, skin-thorax). The mean microscopic extension was found to be 1 cm and the range was reported to be 3-25 mm. The maximum measured MDE distribution was reported in a plot and has been reproduced in Figure A.4.

Finally, Schmitz et al. [26] examined 64 lumpectomy specimens from 62 patients to determine the distance of microscopic disease from the GTV on MRI. MDE was present in 53 of the 64 (83%) specimens. In 3 specimens the macroscopic tumor was not visible on MRI, these were excluded from the MDE analysis. The mean distance from the tumor on MRI scans to microscopic disease found in the specimens was 5.0 mm. The authors provided the probability of microscopic disease for distances up to 50 mm in a plot, this data is plotted in Figure A.4.

A.3.2. Breast MDE data

An overview of the literature findings is summarized in Table A.2 and the cumulative distribution and a plot of the cumulative distributions obtained from the different studies is presented in Figure A.4.

To compare the MDE data between the different studies in Table A.2, it is important to first note the size of the specimen that was studied. Holland et al. [54] and Faverly et al. [50] studied mastectomy specimens and therefore investigated all of the breast tissue for the presence of MDEs. Vicini et al. [55] investigated reexcision specimens and it must be kept in mind that their distance data does not include the surgical margin of the original lumpectomy specimen. The used surgical margin is not reported in the study, it is only noted that along with the macroscopic tumor, a rim of normal breast tissue was excised. As the typical used surgical margin is at least 1 cm [26, 27, 50], it is safe to assume we need to add at least 10 mm to the measured MDE distance from Vicini et al. Finally, Stroom et al. [27] and Schmitz et al. [26] only studied initial lumpectomy specimens and therefore examined a smaller tissue volume than the studies by Holland et al. Faverly et al. and Vicini et al. investigated. In the study by Stroom et al. it is noted that in three of the specimens tumor was found at the resection margin, but after further investigation it was concluded that it is unlikely there would be further microscopic disease in 2 of the patients. The third patient was reexcised, but no residual microscopic disease was found in this reexcision specimen. Schmitz et al. report that in 21 specimens tumor was found at the resection

Table A.2: Overview of the literature findings on MDE in breast cancer: the number of patients with MDE vs. the total number of studied patients, the mean/median MDE distance, the range of MDE, whether any spatial information was provided and whether a shrinkage factor was used. - indicates that this variable is not provided by the authors.

	Holland et al. [54]	Faverly et al. [50]	Vicini et al. [55]	Stroom et al. [27]	Schmitz et al. [26]
MDE patients/total patients (%)	177/282 (63)	-/135(-)	214/333 (64.3)	31/38 (82)	53/61 (87)
MDE distance (mm)	-	-	Mean: 7.9 Median: 6.0	Mean: 10	Mean: 5
MDE range (mm)	0-100	-	1.0-29.0	3-25	0-42
Spatial information provided	No	No	No	Yes	No
Shrinkage factor	No	No	No	No	No

margin. No further information is reported on these specimens. It is possible that the MDE data from Stroom et al. and Schmitz et al. underestimates the actual distribution of microscopic disease, as there might be microscopic disease further from the original tumor that was not removed during surgery and could therefore not be identified.

In three of the studies, a mean value is reported for the maximum MDE distance: Vicini et al. [55], Stroom et al. [27] and Schmitz et al. [26] reported a mean MDE distance of 7.9 mm, 10 mm and 5 mm, respectively. Keeping in mind that the value for the MDE distance from Vicini et al. is likely underestimated, the differences between the maximum MDE distance in these studies is quite big. The range of the maximum extent is reported in Holland et al. [54], Vicini et al. [55], Stroom et al. [27] and Schmitz et al. [26]. The range of MDE reported in Holland et al. is 0-100 mm, which is much larger than the reported ranges from the other studies (1-29 mm, 3-25 mm and 0-42 mm for Vicini et al. Stroom et al. and Schmitz et al. respectively). This is because Holland et al. investigated a much larger tissue volume. Furthermore, it is unknown if patients included in the investigation by Holland et al. would be eligible for BCT if the modern standards for BCT eligibility as used in Vicini et al. Stroom et al. and Schmitz et al. would be applied. It is therefore possible that the MDE data found by Holland et al. is not representative for BCT eligible patients, but shows an overestimation of the extent of microscopic disease for such patients.

Next, it is important to note whether a study compensated for tumor shrinkage. As is noted in Table A.2, none of the studies used a shrinkage factor. This will therefore not introduce differences between them. However, studies investigating tumor shrinkage in breast tissue suggest that size changes for the tumor and the surrounding tissue can occur. In Pritt et al. [36], a decrease ranging from 0-7 mm in tumor size was noted in 40% of the investigated specimens. In another study no significant change in tumor size was found, but a 15%-20% decrease was found in the distance from the gross tumor to the excision margin [40]. This suggests that although the tumor tissue did not change in size, the surrounding normal breast tissue did shrink. As MDE studies for breast tissue investigate the surrounding normal breast tissue, it is possible that the measured maximum distance in the studies underestimates the actual extent of microscopic disease.

Only Stroom et al. [27] reported an investigation of the spatial distribution of the macroscopic disease extension. They concluded that there was no significant difference in the microscopic extension in the different investigated directions.

Lastly, the cumulative distributions of the probability of finding microscopic disease beyond a certain distance from Figure A.4 are discussed. Clearly, the distribution of Holland et al. suggests higher probabilities for larger distances and is quite similar to the trend suggested by the data from Faverly et al. for a distance beyond 20 mm from the macroscopic tumor. The cumulative distributions from the most recent studies by Stroom et al. and Schmitz et al. are very similar to each other. The cumulative distribution from Vicini et al. suggests much lower probabilities for disease up to 30 mm than the other studies. However, as discussed earlier, it is safe to assume that at least 10 mm should be added to the MDE data from Vicini et al. to account for the surgical margin of the initial excision specimen. In Figure A.5, the data from Vicini et al. is adjusted for a surgical margin of 10 mm. Clearly, the distribution from Vicini et al. has become much more similar to that from Stroom et al. and Schmitz et al.
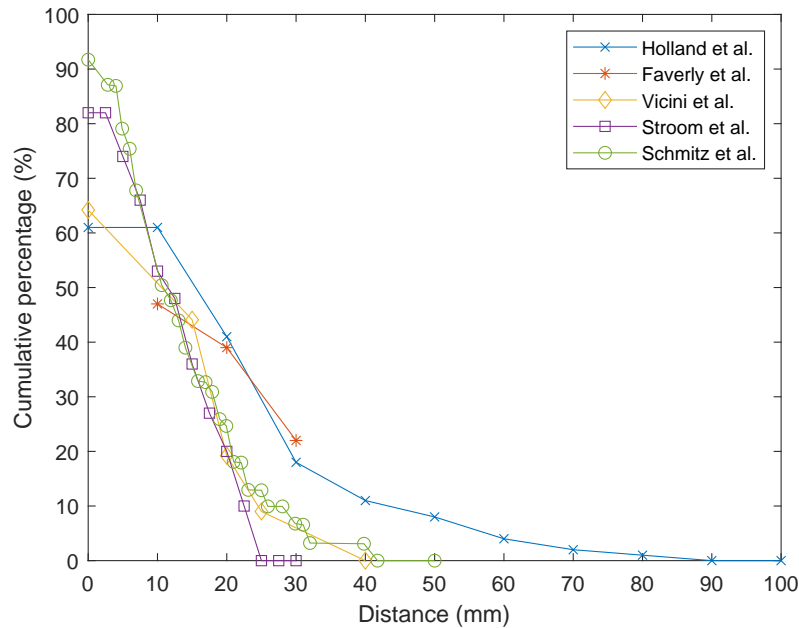
Figure A.5: Cumulative distribution of the probability of finding microscopic disease beyond a certain distance from the macroscopic tumor in patients with breast cancer for different histopathological studies, with the data from Vicini et al. adjusted for an assumed surgical margin from the original excision specimen [26, 27, 50, 54, 55].

A.4. Non-small cell lung cancer

Non-small cell lung cancer (NSCLC) is the most prevalent type of lung cancer, approximately 84% of lung cancer patients are diagnosed with NSCLC [56]. Surgery (lobectomy, removal of the lobe containing the tumor from the lung) is the main treatment method for early-stage NSCLC [57]. However, for patients who are not eligible for surgery, stereotactic body radiation (SBRT) is the treatment of choice [57]. To properly define the CTV for a high-precision radiation treatment, such as SBRT, it is important to know the microscopic extent of the tumor.

A.4.1. Histopathological studies

Giraud et al. [58] investigated the microscopic disease extension for the two most prevalent types of non-small cell lung cancer, adenocarcinoma (ADC) and squamous cell carcinoma (SCC). The authors measured the MDE from 70 lobectomy or pneumonectomy (removal of an entire lung) specimens (32 ADC and 38 SCC specimens). 28 of these specimens (9 ADC and 19 SCC) were excluded from the analysis, as the lung cells in these specimens displayed an insufficient degree of insufflation. Unlike in most histopathological studies, the authors measured the maximum MDE distance on each of the slides that were obtained from these specimens and analysed the MDE for all of the slides instead of for only the maximum MDE per specimen. A total of 222 slides were obtained from the included specimens. The reported mean MDE for ADC was 2.69 mm and for SCC 1.48 mm. These averages include the slides for which no tumor extension was found. The authors reported the exact maximum MDE distributions for adenocarcinoma and squamous cell carcinoma in tables. This data can be used to compute the overall mean of the MDE for both cancer types combined, which is 2.16 mm. The overall cumulative distribution of MDE was also computed using the distributions for ADC and SCC and is plotted in Figure A.6.

In 2003, Goldstein et al. [59] studied the MDE in 31 wedge resection specimens from adenocarcinoma patients. They reported the mean and median of the maximum microscopic disease to be 7.4 and 7 mm, respectively. The range of MDE is reported to be 3.0-14.0 mm. No further specific distance data is given for the MDE.

In a study by Grills et al. [60], the microscopic disease extension was investigated in 35 adenocarcinoma lobectomy specimens. The mean microscopic extension was 7.2 mm and the range was 2-16 mm. The authors provided a plot of the cumulative percentage of cases at maximum microscopic

extension distances up to 15 mm. This data is plotted in Figure A.6.

Loon et al. [61] studied the microscopic disease extension in three directions in lobectomy specimens from 34 patients. MDE was found in 17 patients (50%) and the authors reported that in 90% of the patients MDE does not extend beyond 26 mm. The authors also examined the distribution of the MDE in the transverse plane and conclude that it is isotropic in the transverse plane (medial of GTV in 26%, lateral 29%, dorsal 23% and ventral 22% of patients). No MDE was found in the cranial and caudal direction, which is likely due to undersampling in the cranio-caudal directions with slices at 1 cm from each other. The cumulative distribution of the maximum MDE distance is reported by the authors in a plot and is plotted in Figure A.6.

Finally, Meng et al. [62] studied MDE in 39 lobectomy specimens from ADC and SCC patients. MDE was present in 38/39 (97%) patients. The reported mean MDE is 3.38 mm. The exact MDE of each patient was provided in a table and was used to compute the cumulative distribution plotted in Figure A.6.
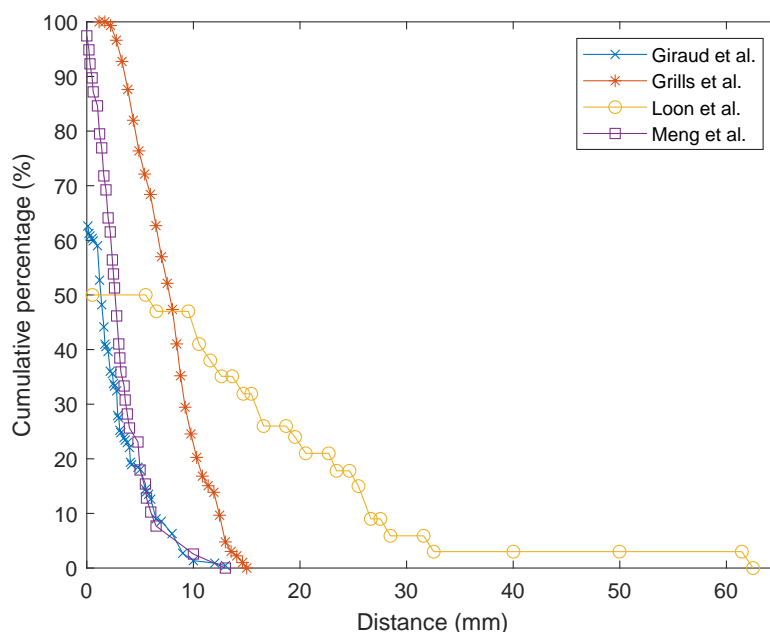
Figure A.6: Cumulative distribution of the probability of finding microscopic disease beyond a certain distance from the macroscopic tumor in patients with non-small cell lung cancer for different histopathological studies [58, 60–62].

A.4.2. Lung MDE data

An overview of the literature findings is summarized in Table A.3 and a plot of the cumulative distributions obtained from the different studies is presented in Figure A.6.

First, we take a look at the investigated area in the different studies. In the study by Giraud et al. [58], lobectomy and pneumonectomy specimens were studied and in Grills et al. [60], Van Loon et al. [61] and Meng et al. [62] lobectomy specimens were included. Giraud et al. Grills et al. and Meng et al. only investigated the microscopic slides that contained some part of the macroscopic tumor from the obtained lobectomy and pneumonectomy specimens. This means that slides from tissue directly adjacent to the tumor are excluded. This method might therefore miss some microscopic disease that is present in the direction perpendicular to the slides, leading to a possible underestimation of the microscopic disease extent. Van Loon et al. investigated all microscopic slides with lung tissue at a minimal margin of 2 cm from the tumor, allowing for an adequate three-dimensional analysis of microscopic disease. Goldstein et al. [59] investigated the MDE in wedge resection specimens. These are the smallest type of resection specimens that can be used to excise tumor from lung patients. Goldstein et al. state that an "ample" rim of healthy tissue was present surrounding the excised macroscopic tumor, but the exact surgical margin that was used is not provided. The authors did report the mean, median and range of the minimal distance between microscopic disease and the edge of the specimen. The mean and

Table A.3: Overview of the literature findings on MDE in lung cancer: the number of patients with MDE vs. the total number of studied patients, the mean/median MDE distance, the range of MDE, whether any spatial information was provided and whether a shrinkage factor was used. - indicates that this variable is not provided by the authors; *indicates that the variable was computed from data provided by the authors.

	Giraud et al. [58]	Goldstein et al. [59]	Grills et al. [60]	Van Loon et al. [61]	Meng et al. [62]
MDE patients/total patients (%)	-/70(-)	31/31 (100)	35/35 (100)	17/34 (50)	38/39 (97)
MDE distance (mm)	Mean: 2.69 (ADC) 1.48 (SCC) Mean*: 2.16	Mean: 7.4 Median: 7	Mean: 7.2	-	Mean: 3.38
MDE range (mm)	0-12 (ADC) 0-13 (SCC)	3.0-14.0	2-16	0-60	0-13
Patients without MDE included in mean/median	Yes	No	No	-	Yes
Spatial information provided	No	No	No	Yes	No
Shrinkage factor	No	No	No	Yes	No

median were 2.3 and 2.0 mm and the range was 0-4.0 mm. As the minimum distance reported was 0 mm, it is likely that microscopic disease was missed in this study. The reported extent of the MDE from Goldstein et al. is therefore likely underestimated.

As noted in Table A.3, a mean value of the maximum MDE was reported or could be computed from data provided by the authors in four of the five studies. The mean value for the data from Giraud et al. was computed to be 2.16 mm. This is smaller than the measured mean MDE from Goldstein et al. (7.4 mm), Grills et al. (7.2 mm) and Meng et al. (3.38 mm). The measured mean of Goldstein et al. and Grills et al. are in good agreement with each other. The range of the MDE was reported by all studies, and is similar in Giraud et al. Goldstein et al. Grills et al. and Meng et al. (0-13, 3-14, 2-16 and 0-13 mm, respectively). Van Loon et al. reported a range of 0-60 mm and therefore found a much larger MDE distance than the other studies. From the mean MDE and the range of the MDE, it can be concluded that a large variation exists in the measured extent of microscopic disease from the macroscopic tumor.

There is one main factor that can explain the large discrepancy of the range of microscopic disease that was reported in Van Loon et al. compared to the other studies. This study was the only study that attempted to account for tumor deformation after surgery. In a previous study [39], the authors had determined that the lung tissue surrounding the macroscopic tumor had decreased in size by 57% on average. Van Loon et al. therefore used the methodology described in that study to account for post-surgical tissue shrinkage. Given the large decrease in size of the healthy lung tissue that was found by Siedschlag et al. [39], the reported maximum MDE distance from the other four studies is probably a large underestimation of the actual MDE distance. Meng et al. [62] note that in a previous study [63] they found that tumor volume reduced to 82% ±10% of the original tumor volume, but despite this knowledge they did not attempt account for tumor shrinkage.

Only Van Loon et al. reported a spatial distribution of the location of microscopic disease, relative to the macroscopic tumor. In the transverse plane, the distribution was found to be isotropic. No MDE was found in the cranio-caudal directions from the tumor, due to undersampling in these directions. Microscopic slices were cut perpendicular to the cranio-caudal directions at 1 cm from each other. Therefore, microscopic disease present between two slices was missed. The authors assumed that the microscopic disease is also distributed isotropically in the cranio-caudal direction.

To conclude, there is also a large difference between the cumulative distributions of the probability of finding microscopic disease beyond a certain distance from the different studies (Figure A.6. The distributions from [58] and [62] show quite a similar trend for the probability of finding microscopic disease beyond a certain distance. The main difference is in the probability of finding microscopic disease beyond the tumor edge: in Meng et al. this percentage was 97%, whereas in Giraud et al. this percent-
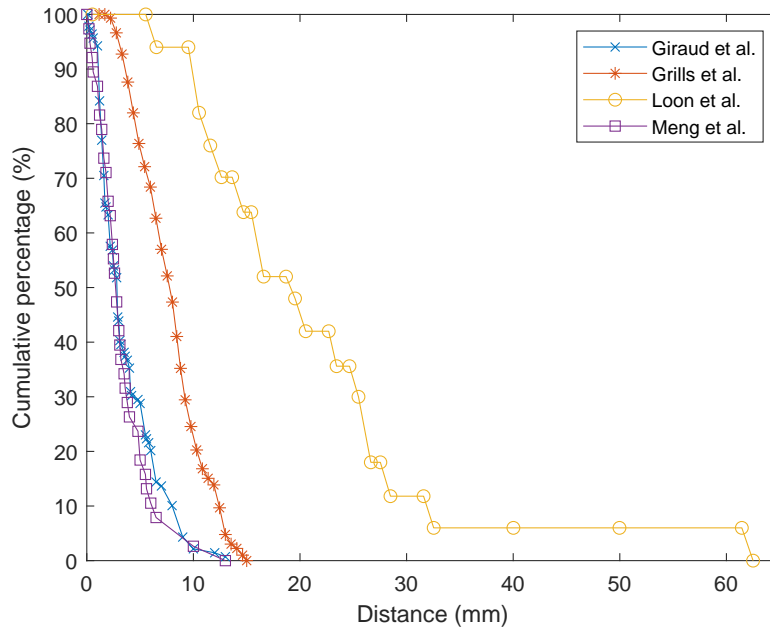
Figure A.7: Cumulative distribution of the probability of finding microscopic disease beyond a certain distance from the macroscopic tumor in patients with MDE with non-small cell lung cancer for different histopathological studies [58, 60–62].

age was 63%. This difference also explains the large difference in the mean MDE distance reported for both studies in Table A.3 (2.16 mm and 3.38 mm for Giraud et al. and Meng et al. respectively). The similarity between the distributions can be better assessed by excluding the samples where no MDE was found from the cumulative distributions. Such a plot is provided for all four cumulative distributions in Figure A.7). In this plot, it is clear that the cumulative distributions from Giraud et al. and Meng et al. are very similar. The mean MDE after exclusion of samples without MDE is also very similar, 3.44 mm and 3.47 mm for Giraud et al. and Meng et al. respectively. The cumulative distribution obtained from Van Loon et al. is significantly different from the other distributions, this is probably largely due to the fact that Van Loon et al. accounted for tissue deformations, unlike the other studies.

A.5. Prostate cancer

Prostate cancer is known as an often multifocal disease with an index lesion and multiple satellite lesions spread throughout the prostate and therefore it is common practice to treat the entire prostate [32]; prostate cancer is predominantly treated by radiotherapy or surgery (prostatectomy) [64]. In patients with prostate cancer a type of microscopic extension, called extracapsular extension (ECE) or extraprostatic extension (EPE), can occur. This ECE or EPE is defined as the extension of prostate cancer beyond the prostate boundaries[65]. Several histopathological studies were carried out to determine the radial extent of ECE beyond the prostate boundaries, to allow for determination of an appropriate CTV margin [66–70]. In all these studies, the ECE was defined as the distance that the tumor extends from the outer margin of the prostate capsule, measured perpendicularly to the surface. In specimens with multiple sites of ECE, the distance at the site with the largest extension was recorded.

A.5.1. Histopathological studies

Davis et al. [66] studied ECE in 376 prostatectomy specimens and measured the radial distance of ECE. In 105/376 (28%) a total of 248 ECE sites were found. The authors reported a mean and median maximum radial distance of 0.8 mm and 0.5 mm, respectively. The range of ECE distance was 0.04-4.4 mm. The distribution of the radial distance of ECE was provided in a table and is plotted in Figure A.8. The authors also recorded the location of the ECE sites with respect to the craniocaudal direction (bladder base, superior, middle prostate or inferior), lateral direction (right or left) and anteroposterior direction (anterior, later or posterior). The spatial distribution was reported as following: laterally, the ECE sites

Table A.4: Extent of extrapcapsular extension for different locations.

Location	Median ECE (mm)	Range of ECE (mm)	90th percentile (mm)
Posterolateral	1.1	0.1-7.0	2.9
Posterior	0.5	0.1-3.5	3.3
Lateral	0.6	0.1-10.0	3.9
Base	1.5	0.1-10.0	9.4

were evenly distributed between the left (52%) and right (48%) sides of the prostate; craniocaudally, 57% of the sites was located in the midprostate, 38% in superior locations, 5% in inferior locations and <1% at the bladder base; anteroposteriorly, 56% of the ECE sites was located in the posterior prostate, 28% in lateral locations and 15% in anterior locations.

In 2000, Sohayda et al. [67] studied ECE in 256 prostatectomy specimens. ECE was identified in 92 (35%) specimens, but measurements were only performed in 79 of these 92 cases. A total of 98 ECE sites were found. The mean and median maximum radial distance was 1.7 and 1.1 mm, respectively. The range of ECE was 0.1-10.0 mm and the 90th percentile was at 3.8 mm. A more specific distribution of the maximum ECE was reported in the text and is provided in the plot in Figure A.8; in this plot the 13 cases for which the ECE was not measured, are omitted from the distribution. The authors also recorded the spatial locations of the ECE sites: the location of the ECE sites was posterolateral in 53% of the ECE sites, lateral in 24%, posterior in 13% and at the bladder base in 10% . Additionally, the median ECE, range of ECE and 90th percentile for each location were tabulated, this data can be found in Table A.4.

Teh et al. [68] analysed the ECE in a large population of 712 prostatectomy specimens. ECE was identified in 299/712 (42%) of the specimens, but measurable extension was present in only 185 specimens. The mean, median and range of ECE were 2.93, 2.00 mm and 0.5-12.00 mm, respectively. The distribution of the radial distance of ECE was provided in a table and is plotted in Figure A.8.

In 2006, the radial distance of ECE was studied by Chao et al. [69] in 371 prostatectomy specimens. ECE was found in 121/371 (33%) specimens. The authors reported the mean, median and range of ECE to be 2.4 mm, 2.3 mm and 0.05-7 mm; the 90th percentile of ECE was 5.0 mm. More specific distance information of the extent of ECE is provided in a dot density plot and this information was used to plot the cumulative distribution in Figure A.8. Most of the identifiable ECE was found in the posterolateral region of the prostate and all of the ECE sites with a distance ≥2 mm from the prostate were found in this region.

Finally, Schwartz et al. [70] investigated the radial distance of ECE in 2007; 404 prostatectomy specimens were analysed of which 121 (30%) contained ECE. The mean, median and range of the ECE were 0.9 mm, 0.6 mm and 0.0-5.7 mm, respectively. It is furthermore indicated how many patients there where with an ECE smaller than the median (59 (15%)) and bigger than the median (62 (15%)). Further specific distance information is not reported by the authors, so this course distribution is plotted in Figure A.8.

A.5.2. Prostate MDE data
An overview of the literature findings is summarized in Table A.5 and a plot of the cumulative distributions obtained from the different studies is presented in Figure A.8.

In all the studies, the entire prostatectomy specimen was investigated for extracapsular extensions. It can therefore be assumed that all the present ECEs were identified. In some cases an ECE extends to the edge of the surgical specimen. In Davis et al. [66], it is indicated that if an ECE site extended to the edge of the specimen and had the maximum measured distance from all ECE sites in the specimen, the maximum ECE distance was recorded as the distance from the prostatic capsule to the edge of the specimen. This was the case in 27 of the 105 specimens with ECE, for these cases the actual maximum ECE distance is therefore underestimated. This could be an explanation In Sohayda et al. [67], 38 of the 79 specimens with ECE had at least one ECE site that extended to the edge of the specimens. It was however not indicated if the maximum measured ECE distance in these specimens corresponded to an ECE that extended to the edge of the surgical specimen. Teh et al. [68] reported a total of 48 of the 185 specimens with ECE to have at least once ECE site that extended to the edge of the specimens. Again, it was not noted whether the maximum measured ECE distance corresponded to an ECE that
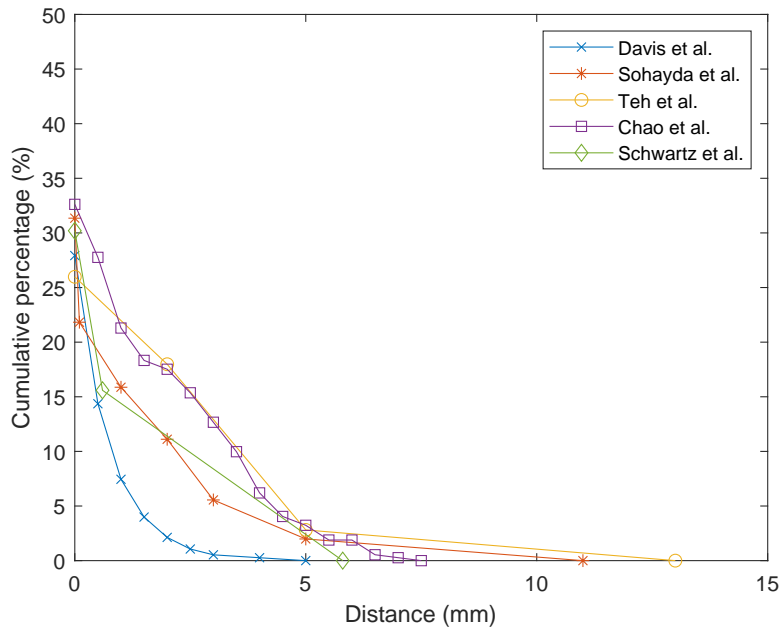
Figure A.8: Cumulative distribution of the probability of finding extracapsular extension beyond a certain distance from the macroscopic tumor in patients with prostate cancer for different histopathological studies [66–70].

extended to the edge of the specimen. Chao et al. [69] reported that in 62% of the specimens displaying ECE, tumor was found on the edge of the specimen. It is however not clear whether this was tumor from an ECE site or tumor located inside the prostate due to an inadequate surgical excision of the entire prostate volume. Schwartz et al. [70] does not report how many specimens had a positive margin. They do mention in their method that it was noted if an ECE site was measured to have the maximum ECE distance of a specimen, but do not report if and for how many specimens this was the case. To conclude in all the studies there is a chance at an underestimation of the extent of ECEs due to ECE extending beyond the edge of the surgical specimen. With the information provided by the authors, it is however difficult to estimate for how many specimens this was the case and it is unknown how far the ECE might have extended beyond the surgical edge.

A median value of the maximum ECE distance was reported in all studies and a mean value was reported in Davis et al. Chao et al. and Schwartz et al. (Table A.5). The mean and median values from Davis et al. and Schwartz et al. are similar, as are the median values from Teh et al. and Chao et al. The median value reported by Sohayda et al. is in between the values from the other studies. The reported range of the maximum ECE distance differs between all the studies: the largest reported

Table A.5: Overview of the literature findings on ECE: the number of patients with measurable ECE vs. the total number of studied patients, the mean/median ECE distance, the range of ECE, whether any spatial information was provided and whether a shrinkage factor was used.

	Davis et al. [66]	Sohayda et al. [67]	Teh et al. [68]	Chao et al. [69]	Schwartz et al. [70]
ECE patients/ (%) total patients	105/376 (28)	79/265 (35)	185/712 (26)	121/371 (33)	121/404 (30)
ECE distance (mm)	Mean: 0.8 Median: 0.5	Median: 1.1	Median: 2.0	Mean: 2.3 Median: 2.4	Mean: 0.9 Median: 0.6
ECE range (mm)	0.04-4.4	0.1-10.0	0.5-12.0	0.05-7	0.0-5.7
Spatial information provided	Yes	Yes	No	Yes	No
Shrinkage factor	No	No	Yes	No	No

maximum ECE distance ranges from 4.4 mm in Davis et al. to 12.0 mm in Teh et al. Tumor shrinkage was only adjusted for with a shrinkage factor in the study by Teh et al. They used a linear shrinkage factor of 1.14, which was reported in Schned et al. [71].

Information on the spatial distribution of the ECE sites was provided by Davis et al. Sohayda et al. and Chao et al. Both Sohayda et al. and Chao et al. report a high incidence of ECE sites in the posterolateral prostate (53% and 'most of the ECE' according to Sohadya et al. and Chao et al. respectively). Davis et al. uses a different manner of reporting the spatial distribution, but is in agreement that the posterior prostate had the highest incidence of ECE sites (56%), if the anteroposterior direction is regarded.

The cumulative distributions from Sohayda et al. Teh et al. Chao et al. and Schwartz et al. (Figure A.8 show somewhat similar trends, but the exact probabilities of finding extracapsular extension beyond certain distances vary quite a bit. The cumulative distribution from Davis et al. shows a much steeper decrease in the probability of finding ECE beyond a certain distance than the other four studies. Although the median values of the maximum ECE distance were similar for Davis et al. and Schwartz et al. this is not true for their cumulative distributions. The cumulative distribution from Schwartz et al. is more comparable to the cumulative distribution found by Sohayda et al. than to the distribution found by Davis et al. The distributions from Teh et al. and Chao et al. are also similar. It is interesting to note that Teh et al. accounted for tumor shrinkage, whereas Chao et al. did not. The maximum ECE distance is clearly much larger in the data from Teh et al. than for Chao et al. but in the range between 1 and 6 mm the probability for finding microscopic disease is quite similar for both cumulative distributions. This implicates that if Chao et al. would also have corrected for tumor shrinkage, the cumulative distribution of finding disease would probably shift slightly to the right, resulting in higher probabilities of microscopic disease at larger distances from the macroscopic tumor.

A.6. Comparing reported data between tumor sites

As could be concluded from the previous sections, a range of different types of data is reported in histopathological and radiological studies on microscopic disease extension. In this section the differences and similarities in reported data between the different tumor sites will be investigated.

There are two types of studies that have been discussed in this chapter, namely histopathological studies and radiological recurrence studies. Five histopathological studies were identified through the literature search for breast, lung and prostate cancer. For brain, 4 studies were found, but only one of these was a histopathological study and the other three were recurrence studies. Histopathological studies will always provide a more accurate assessment of the extent of microscopic disease, so the found data for MDE in brain tumor is not as reliable as the data for the other tumor sites.

The size of the investigated area varies among the tumor sites. Regarding the brain cancer studies, 1-2 cm thick transverse whole-brain sections were studied in the histopathological brain study [44] and the recurrence studies [45–47] studied CT slices in the transverse plane at the height of the maximum original tumor size. In all these studies, any microscopic disease in the cranio-caudal direction could have been missed and the extent of microscopic disease could therefore be underestimated. In the breast cancer studies, different sizes of specimens were investigated. Two studies [50, 54] studied mastectomy specimens. For these studies it can be assumed that all MDE was found, as the entire breast was studied for presence of microscopic disease. One study investigated reexcision specimens [55], which means that their data underestimates the range of microscopic disease by at least 1 cm from the initial excision specimen. The last two studies [26, 27] studied initial lumpectomy specimens. The data from these studies potentially underestimates the actual extent of microscopic disease as the investigated area was smaller in these studies than in the other three. From the lung cancer studies, one study [58] investigated both lobectomy and pneumonectomy specimens, three studies [60–62] investigated lobectomy specimens and the fifth study [59] investigated wedge resection specimens. Both lobectomy and pneumonectomy specimens contain a rather large area of tissue surrounding the tumor, so it can be assumed that all tissue containing microscopic disease was available for investigation. Three of the studies using lobectomy or pneumonectomy specimens [58, 60, 62] only investigated transverse slides that contained some part of macroscopic tumor, so any microscopic disease present in the direction perpendicular to the slides could have been missed. The other study [61] investigated all slides at a minimal margin of 2 cm from the tumor, also in the direction perpendicular to the slides. It can therefore be assumed that this study provides a more accurate MDE distribution than the former

three studies. Wedge resection specimens are the smallest type of resection specimens. In the study investigating wedge resection specimens [59], it was reported that for some specimens microscopic disease was found at the edge of the specimen. It is thus likely that microscopic disease further away from the macroscopic tumor was missed. All of the prostate cancer studies investigated entire prostatectomy specimens. It is thus likely that all the present ECEs were identified. In some cases the ECEs extended to the edge of the prostatectomy specimens. If this was the case, the radial distance of the ECE was reported as the distance to the edge of the specimen, which could result in an underestimation of the actual extent of the ECE.

The manner of reporting the microscopic disease extent differs among study type as well. Two of the radiological recurrence studies [45, 47] reported the exact maximum distance between the recurrent tumor and the initial tumor for each patient. The third recurrence study [46] only reported how many of the recurrences were within a certain distance from the original tumor. Histopathological studies measure the distance of the macroscopic tumor to the microscopic disease in microscopical tissue slices. In almost all of the histopathological studies only the maximum identified MDE distance is reported. In one study for lung cancer [58] the complete MDE distance distribution throughout the analyzed specimen was reported. Furthermore, most of the histopathological studies do not even provide the exact maximum microscopic extension for each patient. The only study that reported such patient-specific data, was a study investigating the MDE in lung cancer [62]. Most of the histopathological studies reported probability distributions or cumulative distributions of the maximum MDE distance, some studies reported only the number of patients with a certain maximum MDE distance. The histopathological study from the brain tumor site [44] reported the number of patients in which microscopic disease could be found up to a certain distance. For the breast cancer studies, four of the five studies reported a cumulative distribution of the maximum MDE distance [26, 27, 50, 54] and one study reported a probability distribution [55]. From the lung cancer studies, two studies reported a cumulative distribution [60, 61], one study reported the maximum MDE for each patient [62], one study reported the complete MDE distance distribution [58] and the last study did not report any information on the distribution of the maximum MDE [59]. Two of the prostate cancer studies reported the number of patients in which microscopic disease could be found up to a certain distance, the probability distribution and a cumulative distribution of the maximum MDE [66, 68], two of the studies reported both the number of patients in which microscopic disease could be found up to a certain distance and the probability distribution [67, 70] and the last study only reported the number of patients in which microscopic disease could be found up to a certain distance [69].

Some histopathological studies adjusted for tissue shrinkage. The extent of shrinkage of tissue post-excision depends on the tissue type. Therefore, there are differences in how big this tissue shrinkage is of influence on the measured maximum MDE distance. The histopathological brain cancer study used corrected for tissue shrinkage as they had previously found that brain tissue shrinkage ranged from 10% to 17% of the original volume. None of the breast cancer studies corrected for tissue shrinkage, despite studies suggesting that tumor shrinkage could range up to a decrease of 7 mm in size [36] and shrinkage of the tissue surrounding the tumor could range up to 20% [40]. One of the five lung cancer studies adjusted for tissue shrinkage [61] as in a previous study they had discovered an average decrease of 57% in the size of the lung tissue surrounding the macroscopic tumor. From the prostate cancer studies, only one study [68] corrected for tissue shrinkage. They used a linear shrinkage factor of 1.14, from a study [71] that determined that the overall net linear shrinkage due to fixation is 4.3%. Tissue shrinkage was only corrected for in a maximum of one study per tumor site and furthermore, only 3 of the 16 studies performed such a correction. The extent of tissue shrinkage that was corrected is quite different between tumor sites. In the prostate the effect of shrinkage that was corrected for was a shrinkage of 4.3%, this is relatively small in comparison with shrinkage of 10% to 17% in brain tissue and shrinkage of up to 20% of breast tissue. The largest shrinkage that was corrected for was in lung tissue, where a shrinkage of approximately 57% was reported. Lung tissue is likely extra sensitive to shrinkage, due to its nature. Lung cells can expand and deflate to allow air into the cells for exchange of mainly oxygen and carbon dioxide. These cells are therefore already extra flexible and probably deflated before tissue fixation, which then escalates the tissue deformation even further. Therefore, it is extra important for studies investigating the extent of microscopic disease in lung tissue to account for such tissue shrinkage. Unfortunately, only one of the five studies performed this correction, which is clearly visible by the large discrepancy in the resulting cumulative distributions (Figure A.6).

To conclude, the extent of microscopic disease varies between the different tumor sites, from a

maximum extension of 12 mm for prostate to a maximum extension of 100 mm for breast cancer. For all tumor sites, probability distributions of the extent of microscopic disease were retrieved from the studies. An isotropic spatial distribution of the location of microscopic disease was found for brain, breast and lung cancer. ECE in prostate cancer was found to have a high incidence at the posterolateral side of the prostate. The probability distribution of the radial distance at which microscopic disease can be found, and the spatial distribution can be used in tumor site-specific probabilistic treatment planning. When using the probability distribution for probabilistic treatment planning, it is important to keep in mind the uncertainties in the obtained distributions, e.g. due to the size of the investigated tissue and tumor shrinkage.

B

Fitting of L for each tumor site

For the ETCP/ELTCP models, the parameter L needs to be determined. We use the MDE data that was gathered in Appendix A to obtain L. As discussed in Section 4.1, the cumulative density function $F_\Delta(\Delta)$ is assumed to be as follows:

$$F_\Delta(\Delta) = -e^{-\frac{\Delta}{L}} \tag{B.1}$$

The gathered MDE data consists of cumulative distributions, but the probability of finding MDE in a patient is included in the data that was presented in Appendix A. Therefore, this data was adjusted to represent only the cumulative probability of finding MDE beyond a certain distance, given that a patient has MDE, by removing all patients without MDE from the data sets. Furthermore, the adjusted MDE data sets are all reverse cumulative distributions, with a cumulative probability of 1.0 at a distance of 0 mm from the macroscopic tumor to a cumulative probability of 0.0 at larger distances. Therefore we fit the reverse of Equation B.1 to the data to obtain L:

$$-F_\Delta(\Delta) = e^{-\frac{\Delta}{L}} \tag{B.2}$$

Figures B.1-B.4 show the adjusted MDE data sets with the corresponding fitted curves in black. The found values for L are 17.4 mm, 17.2 mm, 6.15 mm and 1.75 mm for brain, breast, lung and prostate, respectively.
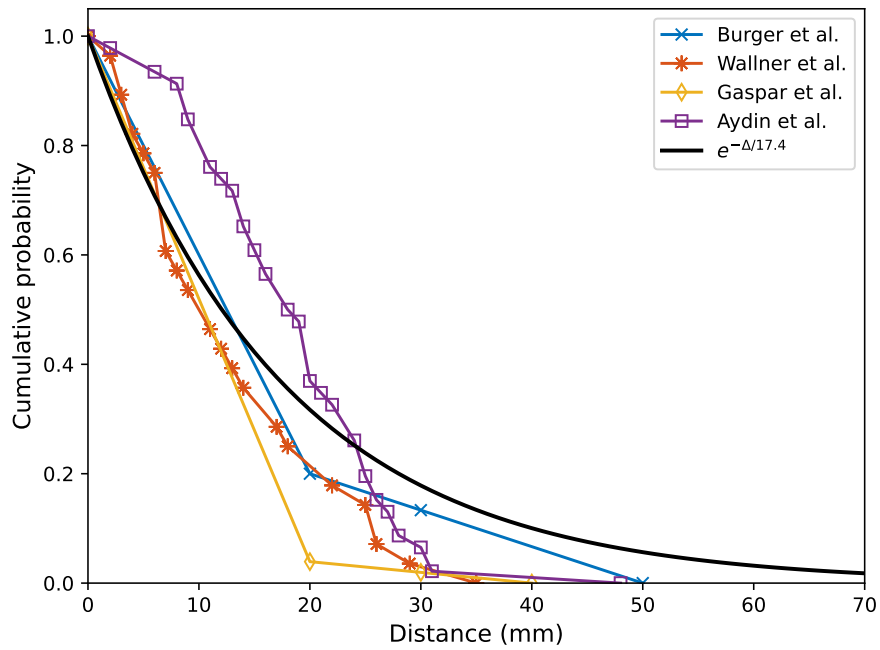
Figure B.1: Cumulative distribution of the probability of finding microscopic disease beyond a certain distance from the macroscopic tumor in patients with brain cancer for different studies [44–47] and the fitted curve in black.
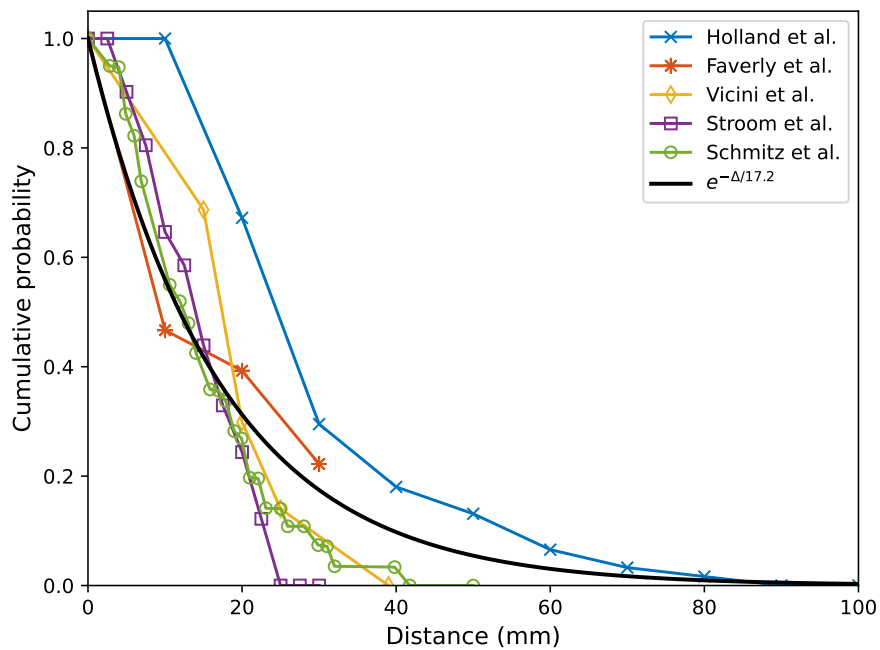
Figure B.2: Cumulative distribution of the probability of finding microscopic disease beyond a certain distance from the macroscopic tumor in patients with breast cancer for different histopathological studies, with the data from Vicini et al. adjusted for an assumed surgical margin from the original excision specimen [26, 27, 50, 54, 55] and the fitted curve in black.
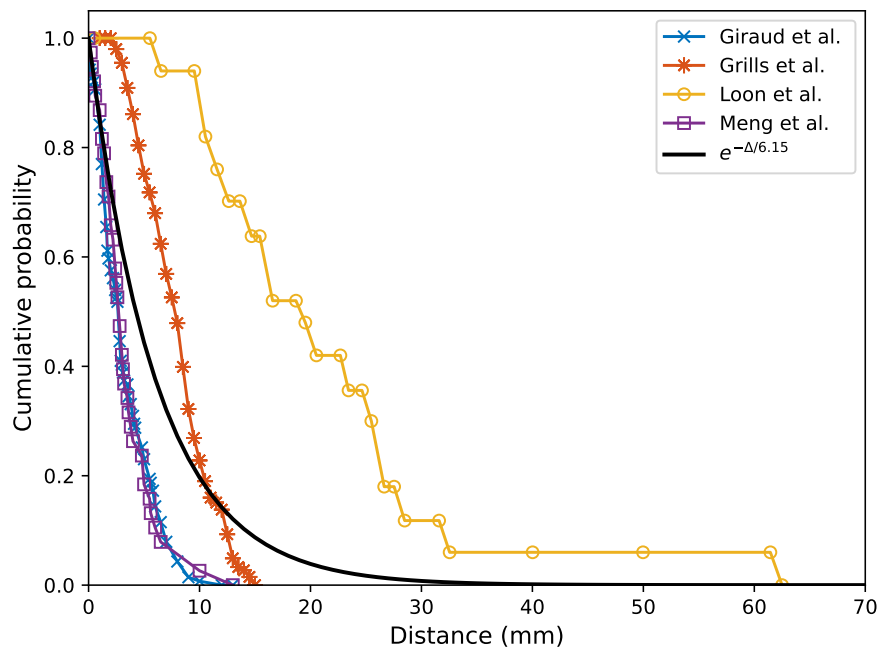
Figure B.3: Cumulative distribution of the probability of finding microscopic disease beyond a certain distance from the macroscopic tumor in patients with MDE with non-small cell lung cancer for different histopathological studies [58, 60–62] and the fitted curve in black.
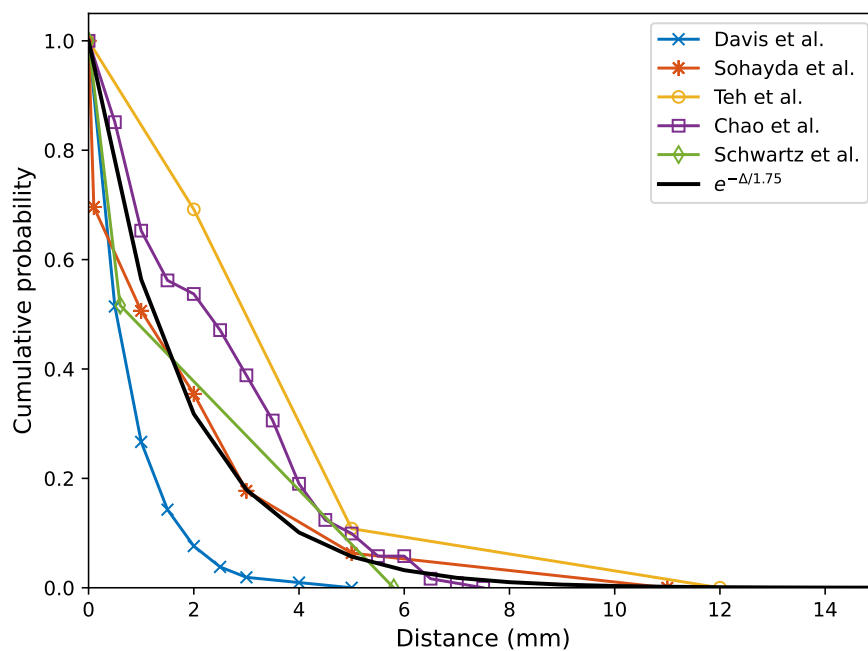
Figure B.4: Cumulative distribution of the probability of finding extracapsular extension beyond a certain distance from the macroscopic tumor in patients with prostate cancer for different histopathological studies [66–70] and the fitted curve in black.

C
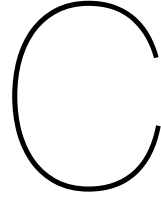
Quadrature Rules

Quadrature rules are used to perform the numerical integration in the basic ETCP and ELTCP models (Section 4.2). The use of the quadrature rules in the model will be explained in more detail in this appendix.

Quadrature rules can be used to integrate any function that resembles a polynomial. Different rules are available to approximate an integral over different intervals. The integral is approximated using a weighted sum of function values at specific points in the domain. The weights used in the summation correspond to the specific points and both the points and weights are dependent on the used quadrature rule. A Gauss-Legendre quadrature is used to compute the integral over the density ρ and a Gauss-Laguerre quadrature is used to compute the integral over the MDE distance Δ.

C.1. Gauss-Legendre quadrature

The Gauss-Legendre quadrature can be used to approximate a function $f(x)$ on the interval $[-1, 1]$:

$$\int_{-1}^{1} f(x)\, \mathrm{d}x \approx \sum_{i=1}^{N_{quad}} w_i f(x_i) \tag{C.1}$$

where N_{quad} is the number of quadrature points, x_i is the ith quadrature point and w_i is the corresponding weight. The Gauss-Legendre quadrature is used to compute the following integral over ρ:

$$\mathbb{E}(TCP) = \int_{\rho} TCP(D, \rho) P_\rho(\rho)\, \mathrm{d}\rho = \int_{\rho_0}^{\rho_1} \frac{TCP(D, \rho)}{\rho_1 - \rho_0}\, \mathrm{d}\rho \tag{C.2}$$

As we are interested in an integral over the interval $[\rho_0, \rho_1]$, a change of interval needs to be performed to the quadrature points from $[-1, 1]$ to $[\rho_0, \rho_1]$. To approximate Equation C.2, we then have

$$\mathbb{E}(TCP) = \int_{\rho_0}^{\rho_1} \frac{TCP(D, \rho)}{\rho_1 - \rho_0}\, \mathrm{d}\rho \approx \sum_{i=1}^{N_{quad}} w_i^\rho TCP(D, \rho_i) \tag{C.3}$$

where $w_i^\rho = \frac{\rho_1 - \rho_0}{2} w_i$ and $\rho_i = \frac{\rho_1 - \rho_0}{2} x_i + \frac{\rho_0 + \rho_1}{2}$.

Similarly, the Gauss-Legendre quadrature is used in the ELTCP model:

$$\mathbb{E}(LTCP) = \int_{\rho_0}^{\rho_1} \frac{LTCP(D, \rho)}{\rho_1 - \rho_0}\, \mathrm{d}\rho \approx \sum_{i=1}^{N_{quad}} w_i^\rho LTCP(D, \rho_i) \tag{C.4}$$

C.2. Gauss-Laguerre quadrature

The Gauss-Laguerre quadrature can be used to approximate a function $f(x)$ on the interval $[0, \infty]$:

$$\int_{0}^{\infty} \mathrm{e}^{-x} f(x)\, \mathrm{d}x \approx \sum_{j=1}^{N_{quad}} w_j f(x_j) \tag{C.5}$$

The Gauss-Legendre quadrature is used to compute the following integral over Δ:

$$\mathbb{E}(TCP) = \int_{\Delta} TCP(D,\Delta)P_{\Delta}(\Delta)\,\mathrm{d}\Delta = \int_0^{\infty} TCP(D,\Delta) \cdot \frac{1}{L}\mathrm{e}^{-\frac{\Delta}{L}}\,\mathrm{d}\Delta \tag{C.6}$$

The Gauss-Laguerre quadrature can only be used for exponents of the form e^{-x}. Therefore, $\frac{\Delta}{L}$ is replaced by $\Delta' = \frac{\Delta}{L}$. The resulting integral is then

$$\mathbb{E}(TCP) = \int_0^{\infty} TCP(D,\Delta'L) \cdot \frac{1}{L}\mathrm{e}^{-\Delta'}\,\mathrm{d}\Delta'L = \int_0^{\infty} TCP(D,\Delta'L) \cdot \mathrm{e}^{-\Delta'}\,\mathrm{d}\Delta' \tag{C.7}$$

This integral can be approximated using the Gauss-Laguerre quadrature as follows:

$$\mathbb{E}(TCP) = \int_0^{\infty} TCP(D,\Delta'L) \cdot \mathrm{e}^{-\Delta'}\,\mathrm{d}\Delta' \approx \sum_{j=1}^{N_{quad}} w_j^{\Delta} TCP(D,\Delta_i) \tag{C.8}$$

where $w_j^{\Delta} = w_j$ and $\Delta_j = x_j L$.

Similarly, the Gauss-Laguerre quadrature is used for the ELTCP model:

$$\mathbb{E}(LTCP) = \int_0^{\infty} LTCP(D,\Delta'L) \cdot \mathrm{e}^{-\Delta'}\,\mathrm{d}\Delta' \approx \sum_{j=1}^{N_{quad}} w_j^{\Delta} LTCP(D,\Delta_i) \tag{C.9}$$

D
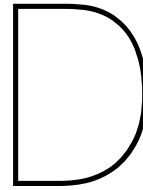
Glossary

Antero-posterior direction	The direction from the front (anterior) to the back (posterior) or vice versa.
Cranio-caudal direction	The direction from head to feet or vice versa, this direction is perpendicular to the **transverse plane**
Initial tumor	Tumor for which the patient was originally diagnosed with cancer
Inferior	Indicates that a structure is located below something, e.g. the mouth is located inferior to the nose
Lateral	Indicates that a structure is located towards the side, e.g. the ears are located lateral to the nose
Lobectomy	Surgical removal of a lung lobe
Lumpectomy	Surgical removal of a tumor in the breast and a rim of healthy tissue surrounding the tumor, also known as **wide local excision**
Mastectomy	Surgical removal of entire breast
Pneumonectomy	Surgical removal of an entire lung
Prostatectomy	Surgical removal of the entire prostate
Reexcision specimen	An additional surgical removal of tissue after an initial surgical tumor removal, such as **lumpectomy**
Recurrent tumor	A new tumor diagnosed in the patient post-treatment of the **initial tumor**
Superior	Indicates that a structure is located above something, e.g. the eyes are located superior to the nose
Transverse plane	Horizontal plane through the body, which divides the body in upper and lower parts
Tumor bed	The tissue that surrounds the tumor site, after surgical tumor removal
Wedge resection	Surgical removal of a small, triangle shaped piece of tissue, to remove a small tumor
Wide local excision	Surgical removal of a tumor in the breast and a rim of healthy tissue surrounding the tumor, also known as **lumpectomy**

E
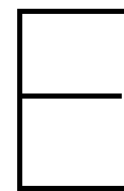
Abbreviations

ADC	Adenocarcinoma
BCT	Breast Conserving Therapy
BED	Biologically Effective Dose
CT	Computed Tomography
CTD	Clinical Target Distribution
CTV	Clinical Target Volume
ECE	Extracapsular Extension
EPE	Extraprostatic Extension
ETCP	Expected Tumor Control Probability
ELTCP	Expected Logarithmic Tumor Control Probability
GTV	Gross Tumor Volume
Gy	Gray
KL	Karhunen-Loève
LQ	Linear Quadratic
LTCP	Logarithmic Tumor Control Probability
MDE	Microscopic Disease Extension
MRI	Magnetic Resonance Imaging
NSCLC	Non-small Cell Lung Cancer
NTCP	Normal Tissue Complication Probability
OAR	Organ at Risk
PTV	Planning Target Volume
SBRT	Stereotactic Body Radiotherapy
SCC	Squamous Cell Carcinoma
SF	Surviving Fraction
TCP	Tumor Control Probability
TPS	Treatment Planning System
WBI	Whole-breast Irradiation

Bibliography

[1] NIH National Cancer Institute. Cancer statistics. URL https://www.cancer.gov/about-cancer/understanding/statistics.

[2] World Health Organization. Key facts on cancer. URL https://www.who.int/news-room/fact-sheets/detail/cancer.

[3] J Ferlay, M Colombet, I Soerjomataram, T Dyba, G Randi, M Bettio, A Gavin, O Visser, and F Bray. Cancer incidence and mortality patterns in Europe: Estimates for 40 countries and 25 major cancers in 2018. *European Journal of Cancer*, 103:356–387, 2018.

[4] Rudi Apolle, Maximilian Rehm, Thomas Bortfeld, Michael Baumann, and Esther G.C. Troost. The clinical target volume in lung, head-and-neck, and esophageal cancer: Lessons from pathological measurement and recurrence analysis. *Clinical and Translational Radiation Oncology*, 3:1–8, 4 2017.

[5] Leyla Moghaddasi, Eva Bezak, and Loredana G. Marcu. Current challenges in clinical target volume definition: Tumour margins and microscopic extensions. *Acta Oncologica*, 51(8):984–995, 2012.

[6] Nadya Shusharina, David Craft, Yen Lin Chen, Helen Shih, and Thomas Bortfeld. The clinical target distribution: A probabilistic alternative to the clinical target volume. *arXiv*, 2018.

[7] Thomas Bortfeld, Nadya Shusharina, and David Craft. Probabilistic definition of the clinical target volume-implications for tumor control probability modeling and optimization. *Physics in Medicine and Biology*, 66(1), 2021. ISSN 13616560. doi: 10.1088/1361-6560/abcad8.

[8] Ilja Briggeman. Novel automated treatment planning approaches to deal with microscopic disease in radiotherapy. Master thesis, Delft University of Technology, 2020.

[9] Jonathan Swart. Conceptual modeling of probabilistic treatment planning to deal with microscopic disease in radiotherapy. Bachelor thesis, Delft University of Technology, 2020.

[10] Leonard L. Gunderson and Joel E. Tepper. *Clinical Radiation Oncology*. 4 edition, 2016.

[11] Christian P Karger. Biological Models in Treatment Planning. In Wolfgang Schlegel, Thomas Bortfeld, and Anca-Ligia Grosu, editors, *New Technologies in Radiation Oncology*, pages 221–235. Springer Berlin Heidelberg, Berlin, Heidelberg, 2006.

[12] John T Lyman. Complication Probability as Assessed from Dose-Volume Histograms. *Radiation Research*, 104(2):S13–S19, 1985.

[13] G J Kutcher, C Burman, L Brewster, M Goitein, and Radhe Mohan. Histogram reduction method for calculating complication probabilities for three-dimensional treatment planning evaluations. *International Journal of Radiation Oncology* Biology* Physics*, 21(1):137–146, 1991.

[14] Gerald J. Kutcher and C. Burman. Calculation of complication probability factors for non-uniform normal tissue irradiation: The effective volume method gerald. *International Journal of Radiation Oncology, Biology, Physics*, 16(6):1623–1630, 6 1989.

[15] C. Burman, G. J. Kutcher, B. Emami, and M. Goitein. Fitting of normal tissue tolerance data to an analytic function. *International Journal of Radiation Oncology, Biology, Physics*, 21(1):123–135, 5 1991.

[16] ICRU. ICRU report 50: Prescribing, recording and reporting photon beam therapy. Technical report, International Commision on Radiation Units and Measurements, Washthington, DC, 1993.

[17] Marcel Van Herk, Peter Remeijer, Coen Rasch, and Joos V. Lebesque. The probability of correct target dosage: Dose-population histograms for deriving treatment margins in radiotherapy. *International Journal of Radiation Oncology Biology Physics*, 47(4):1121–1135, 7 2000.

[18] Jan Unkelbach, Markus Alber, Mark Bangert, Rasmus Bokrantz, Timothy C.Y. Chan, Joseph O. Deasy, Albin Fredriksson, Bram L. Gorissen, Marcel Van Herk, Wei Liu, Houra Mahmoudzadeh, Omid Nohadani, Jeffrey V. Siebers, Marnix Witte, and Huijun Xu. Robust radiotherapy planning. *Physics in Medicine and Biology*, 63(22), 2018.

[19] Marnix G. Witte, Joris Van Der Geer, Christoph Schneider, Joos V. Lebesque, Markus Alber, and Marcel Van Herk. IMRT optimization including random and systematic geometric errors based on the expectation of TCP and NTCP. *Medical Physics*, 34(9):3544–3555, 2007.

[20] Román Bohoslavsky, Marnix G. Witte, Tomas M. Janssen, and Marcel Van Herk. Probabilistic objective functions for margin-less IMRT planning. *Physics in Medicine and Biology*, 58(11):3563–3580, 2013.

[21] David Tilly, Åsa Holm, Erik Grusell, and Anders Ahnesjö. Probabilistic optimization of dose coverage in radiotherapy. *Physics and Imaging in Radiation Oncology*, 10:1–6, 4 2019.

[22] Scipy. scipy.optimize.minimize - SciPy v1.7.0 Manual. URL https://docs.scipy.org/doc/%0Ascipy/reference/generated/scipy.optimize.minimize.html.

[23] Jian-Yue Jin, Feng-Ming Kong, Dezhi Liu, Lei Ren, Haisen Li, Hualiang Zhong, Benjamin Movsas, and Indrin J Chetty. A TCP model incorporating setup uncertainty and tumor cell density variation in microscopic extension to guide treatment planning. *Medical physics*, 38(1):439–448, 1 2011.

[24] Sanjeev Sreenivasan, Venkatesh Madhugiri, Gopalakrishnan Sasidharan, and Roopesh V.R. Kumar. Measuring glioma volumes: A comparison of linear measurement based formulae with the manual image segmentation technique. *Journal of Cancer Research and Therapeutics*, 12(1), 2016. ISSN 19984138. doi: 10.4103/0973-1482.153999.

[25] Piernicola Pedicini, Alba Fiorentino, Vittorio Simeon, Paolo Tini, Costanza Chiumento, Luigi Pirtoli, Marco Salvatore, and Giovanni Storto. Clinical radiobiology of glioblastomamultiforme: estimation of tumor control probability from various radiotherapyfractionation schemes. *Strahlentherapie und Onkologie*, 190(10):925–932, 2014. ISSN 1439099X. doi: 10.1007/s00066-014-0638-9.

[26] Annemarie C. Schmitz, Maurice A.A.J. Van Den Bosch, Claudette E. Loo, Willem P.Th M. Mali, Harry Bartelink, Maria Gertenbach, Roland Holland, Johannes L. Peterse, Emiel J.Th Rutgers, and Kenneth G. Gilhuijs. Precise correlation between MRI and histopathology - Exploring treatment margins for MRI-guided localized breast cancer therapy. *Radiotherapy and Oncology*, 97(2):225–232, 11 2010.

[27] Joep Stroom, Angelique Schlief, Tanja Alderliesten, Hans Peterse, Harry Bartelink, and Kenneth Gilhuijs. Using histopathology breast cancer data to reduce clinical target volume margins at radiotherapy. *International journal of radiation oncology, biology, physics*, 74(3):898–905, 7 2009.

[28] Damián Guirado, Jose M. De La Vega, Rafael Guerrero, and Antonio M. Lallena. Radiobiological parameters for breast cancer: A Monte Carlo analysis of START trial published results. *British Journal of Radiology*, 91(1091), 2018. ISSN 1748880X. doi: 10.1259/bjr.20170979.

[29] M. Guerrero and X. Allen Li. Analysis of a large number of clinical studies for breast cancer radiotherapy: Estimation of radiobiological parameters for treatment planning. *Physics in Medicine and Biology*, 48(20):3307–3326, 2003. ISSN 00319155. doi: 10.1088/0031-9155/48/20/004.

[30] Mohammed Alaswad, Christoph Kleefeld, and Mark Foley. Optimal tumour control for early-stage non-small-cell lung cancer: A radiobiological modelling perspective. *Physica Medica*, 66(July):55–65, 2019. ISSN 1724191X. doi: 10.1016/j.ejmp.2019.09.074. URL https://doi.org/10.1016/j.ejmp.2019.09.074.

[31] Rainer J. Klement, Jan Jakob Sonke, Michael Allgäuer, Nicolaus Andratschke, Steffen Appold, José Belderbos, Claus Belka, Karin Dieckmann, Hans T. Eich, Michael Flentje, Inga Grills, Michael Eble, Andrew Hope, Anca L. Grosu, Sabine Semrau, Reinhart A. Sweeney, Juliane Hörner-Rieber, Maria Werner-Wasik, Rita Engenhart-Cabillic, Hong Ye, and Matthias Guckenberger. Estimation of the α/β ratio of non-small cell lung cancer treated with stereotactic body radiotherapy. *Radiotherapy and Oncology*, 142:210–216, 2020. ISSN 18790887. doi: 10.1016/j.radonc.2019.07.008. URL https://doi.org/10.1016/j.radonc.2019.07.008.

[32] Vladimir Mouraviev, Arnauld Villers, David G. Bostwick, Thomas M. Wheeler, Rodolfo Montironi, and Thomas J. Polascik. Understanding the pathological features of focality, grade and tumour volume of early-stage prostate cancer as a foundation for parenchyma-sparing prostate cancer therapies: Active surveillance and focal targeted therapy. *BJU International*, 108(7):1074–1085, 2011.

[33] Michael Mitterbergera, Wolfgang Horningera, Friedrich Aignerb, Germar M. Pinggeraa, Ilona Steppanb, Peter Rehdera, and Ferdinand Frauscherb. Ultrasound of the prostate. *Cancer Imaging*, 10(1):40–48, 2010. ISSN 14707330. doi: 10.1102/1470-7330.2010.0004.

[34] Piernicola Pedicini, Lidia Strigari, and Marcello Benassi. Estimation of a self-consistent set of radiobiological parameters from hypofractionated versus standard radiation therapy of prostate cancer. *International Journal of Radiation Oncology Biology Physics*, 85(5):e231–e237, 2013. ISSN 03603016. doi: 10.1016/j.ijrobp.2012.11.033. URL http://dx.doi.org/10.1016/j.ijrobp.2012.11.033.

[35] P. C. Burger. Pathologic anatomy and CT correlations in the glioblastoma multiforme. *Applied Neurophysiology*, 46:180–187, 1983.

[36] Bobbi Pritt, Joseph J. Tessitore, Donald L. Weaver, and Hagen Blaszyk. The effect of tissue fixation and processing on breast cancer size. *Human Pathology*, 2005.

[37] Sara Jonmarker, Alexander Valdman, Anna Lindberg, Magnus Hellström, and Lars Egevad. Tissue shrinkage after fixation with formalin injection of prostatectomy specimens. *Virchows Archiv*, 2006.

[38] Po Kuei Hsu, Hsu Chih Huang, Chih Cheng Hsieh, Han Shui Hsu, Yu Chung Wu, Min Hsiung Huang, and Wen Hu Hsu. Effect of Formalin Fixation on Tumor Size Determination in Stage I Non-Small Cell Lung Cancer. *Annals of Thoracic Surgery*, 2007.

[39] Ch Siedschlag, J. Van Loon, A. Van Baardwijk, M. M.G. Rossi, R. Van Pel, J. L.G. Blaauwgeers, R. J. Van Suylen, L. Boersma, J. Stroom, and K. G.A. Gilhuijs. Analysis of the relative deformation of lung lobes before and after surgery in patients with NSCLC. *Physics in Medicine and Biology*, 54(18):5483–5492, 2009.

[40] Christopher Horn and Christopher Naugler. Breast specimen shrinkage following formalin fixation. *Pathology and Laboratory Medicine International*, 2014.

[41] Patrick Y. Wen and Santosh Kesari. Malignant Gliomas in Adults. *New England Journal of Medicine*, 2008.

[42] Constantinos Alifieris and Dimitrios T. Trafalis. Glioblastoma multiforme: Pathogenesis and treatment. *Pharmacology and Therapeutics*, 152:63–82, 2015.

[43] Jennifer L. Shah, Gordon Li, Jenny L. Shaffer, Melissa I. Azoulay, Iris C. Gibbs, Seema Nagpal, and Scott G. Soltys. Stereotactic radiosurgery and hypofractionated radiotherapy for glioblastoma. *Neurosurgery*, 82(1):24–34, 2018.

[44] P. C. Burger, E. R. Heinz, T. Shibata, and P. Kleihues. Topographic anatomy and CT correlations in the untreated glioblastoma multiforme. *Journal of Neurosurgery*, 68(5):698–704, 1988.

[45] Kent E. Wallner, Joseph H. Galicich, George Krol, Ehud Arbit, and Mark G. Malkin. Patterns of failure following treatment for glioblastoma multiforme and anaplastic astrocytoma. *International Journal of Radiation Oncology, Biology, Physics*, 16(6):1405–1409, 1989.

[46] Laurie E. Gaspar, Barbara J. Fisher, David R. Macdonald, Deborah V. Leber, Edward C. Halperin, S. Clifford Schold, and J. Gregory Cairncross. Supratentorial malignant glioma: Patterns of recurrence and implications for external beam local treatment. *International Journal of Radiation Oncology, Biology, Physics*, 24(1):55–57, 1992.

[47] Halim Aydin, Ina Sillenberg, and Harald Von Lieven. Patterns of failure following CT-based 3-D irradiation for malignant glioma. *Strahlentherapie und Onkologie*, 177(8):424–431, 2001.

[48] Quinn T. Ostrom, Haley Gittleman, Peter Liao, Toni Vecchione-Koval, Yingli Wolinsky, Carol Kruchko, and Jill S. Barnholtz-Sloan. CBTRUS Statistical Report: Primary brain and other central nervous system tumors diagnosed in the United States in 2010-2014. *Neuro-oncology*, 19(5): v1–v88, 2017.

[49] Tracy Ann Moo, Rachel Sanford, Chau Dang, and Monica Morrow. Overview of Breast Cancer Therapy. *PET Clinics*, 13(3):339–354, 2018.

[50] Daniel R.G. Faverly, Jan H.C.L. Hendriks, and Roland Holland. Breast carcinomas of limited extent: Frequency, radiologic-pathologic characteristics, and surgical margin requirements. *Cancer*, 91(4):647–659, 2001.

[51] P. Romestaing, Y. Lehingue, C. Carrie, R. Coquard, X. Montbarbon, J. M. Ardiet, N. Mamelle, and J. P. Gérard. Role of a 10-Gy boost in the conservative treatment of early breast cancer: Results of a randomized clinical trial in Lyon, France. *Journal of Clinical Oncology*, 15(3):963–968, 1997.

[52] Harry Bartelink, Jean-Claude Horiot, Philip Poortmans, Henk Struikmans, Walter Van den Bogaert, Isabelle Barillot, Alain Fourquet, Jacques Borger, Jos Jager, Willem Hoogenraad, Laurence Collette, and Marianne Pierart. Recurrence Rates after Treatment of Breast Cancer with Standard Radiotherapy with or without Additional Radiation. *New England Journal of Medicine*, 345(19): 1378–1387, 2001.

[53] Jacques H. Borger, Harry Kemperman, Henk Sillevis Smitt, Augustinus Hart, Joop van Dongen, Joos Lebesque, and Harry Bartelink. Dose and volume effects on fibrosis after breast conservation therapy. *International Journal of Radiation Oncology, Biology, Physics*, 30(5):1073–1081, 1994.

[54] Roland Holland, Solke H.J. Veling, Marcel Avunac, and Jan H.C.L. Hendriks. Histologic multifocality of tis, T1–2 breast carcinomas implications for clinical trials of breast–conserving surgery. *Cancer*, 56(5):979–990, 1985.

[55] Frank A. Vicini, Larry L. Kestin, and Neal S. Goldstein. Defining the clinical target volume for patients with early-stage breast cancer treated with lumpectomy and accelerated partial breast irradiation: A pathologic analysis. *International Journal of Radiation Oncology Biology Physics*, 60(3):722–730, 11 2004.

[56] Howlader N, Noone AM, Krapcho M, Miller D, Brest A, Yu M, Ruhl J, Tatalovich Z, Mariotto A, Lewis DR, Chen HS, Feuer EJ, and Cronin KA. SEER Cancer Statistics Review, 1975-2017. 2020.

[57] J. Vansteenkiste, D. De Ruysscher, W. E.E. Eberhardt, E. Lim, S. Senan, E. Felip, and S. Peters. Early and locally advanced non-small-cell lung cancer (NSCLC): ESMO clinical practice guidelines for diagnosis, treatment and follow-up. *Annals of Oncology*, 24(SUPPL.6):vi89–vi98, 2013.

[58] P Giraud, M Antoine, A Larrouy, B Milleron, P Callard, Y De Rycke, M F Carette, J C Rosenwald, J M Cosset, M Housset, and E Touboul. Evaluation of microscopic tumor extension in non-small-cell lung cancer for three-dimensional conformal radiotherapy planning. *International journal of radiation oncology, biology, physics*, 48(4):1015–1024, 11 2000.

[59] Neal S Goldstein, Monica Ferkowicz, Larry Kestin, Gary W Chmielewski, and Robert J Welsh. Wedge resection margin distances and residual adenocarcinoma in lobectomy specimens. *American journal of clinical pathology*, 120(5):720–724, 11 2003.

[60] Inga S. Grills, Dwight L. Fitch, Neal S. Goldstein, Di Yan, Gary W. Chmielewski, Robert J. Welsh, and Larry L. Kestin. Clinicopathologic Analysis of Microscopic Extension in Lung Adenocarcinoma: Defining Clinical Target Volume for Radiotherapy. *International Journal of Radiation Oncology Biology Physics*, 69(2):334–341, 2007.

[61] Judith Van Loon, Christian Siedschlag, Joep Stroom, Hans Blauwgeers, Robert Jan Van Suylen, Joost Knegjens, Maddalena Rossi, Angela Van Baardwijk, Liesbeth Boersma, Houke Klomp, Wouter Vogel, Sjaak Burgers, and Kenneth Gilhuijs. Microscopic disease extension in three dimensions for non-small-cell lung cancer: Development of a prediction model using pathology-validated positron emission tomography and computed tomography features. *International Journal of Radiation Oncology Biology Physics*, 82(1):448–456, 2012.

[62] Xue Meng, Xindong Sun, Dianbin Mu, Ligang Xing, Li Ma, Baijiang Zhang, Shuqiang Zhao, Guoren Yang, Feng Ming Kong, and Jinming Yu. Noninvasive evaluation of microscopic tumor extensions using standardized uptake value and metabolic tumor volume in non-small-cell lung cancer. *International Journal of Radiation Oncology Biology Physics*, 82(2):960–966, 2012.

[63] Jinming Yu, Xinke Li, Ligang Xing, Dianbin Mu, Zheng Fu, Xiaorong Sun, Xiangyu Sun, Guoren Yang, Baijiang Zhang, Xindong Sun, and C. Clifton Ling. Comparison of Tumor Volumes as Determined by Pathologic Examination and FDG-PET/CT Images of Non-Small-Cell Lung Cancer: A Pilot Study. *International Journal of Radiation Oncology Biology Physics*, 75(5):1468–1474, 12 2009.

[64] Karim Chamie, Stephen B. Williams, and Jim C. Hu. Population-based assessment of determining treatments for prostate cancer. *JAMA Oncology*, 1(1):60–67, 2015.

[65] Hanan Goldberg, Abu Hijlih Ramiz, Rachel Glicksman, Noelia S. Salgado, Thenappan Chandrasekar, Zachary Klaassen, Christopher J.D. Wallis, Ali Hosni, Fabio Ynoe Moraes, Sangeet Ghai, Girish S. Kulkarni, Robert J. Hamilton, Nathan Perlis, Ants Toi, Peter Chung, Andrew Evans, Theo van der Kwast, Antonio Finelli, Neil Fleshner, and Alejandro Berlin. Extraprostatic Extension in Core Biopsies Epitomizes High-risk but Locally Treatable Prostate Cancer. *European Urology Oncology*, 2019.

[66] Brian J. Davis, Thomas M. Pisansky, Torrence M. Wilson, Harold J. Rothenberg, Anna Pacelli, David W. Hillman, Daniel J. Sargent, and David G. Bostwick. The radial distance of extraprostatic extension of prostate carcinoma: Implications for prostate brachytherapy. *Cancer*, 85(12):2630–2637, 1999.

[67] Chris Sohayda, Patrick A. Kupelian, Howard S. Levin, and Eric A. Klein. Extent of extracapsular extension in localized prostate cancer. *Urology*, 55(3):382–386, 2000.

[68] Bin S. Teh, Michael D. Bastasch, Thomas M. Wheeler, Wei Yuan Mai, Anna Frolov, Barry M. Uhl, Hsin H. Lu, L. Steven Carpenter, J. Kam Chiu, John McGary, Shiao Y. Woo, Walter H. Grant, and E. Brian Butler. IMRT for prostate cancer: Defining target volume based on correlated pathologic volume of disease. *International Journal of Radiation Oncology Biology Physics*, 56(1):184–191, 2003.

[69] K Kenneth Chao, Neal S Goldstein, Di Yan, Carlos E Vargas, Michel I Ghilezan, Howard J Korman, Kenneth M Kernen, Jay B Hollander, Jose A Gonzalez, Alvaro A Martinez, Frank A Vicini, and Larry L Kestin. Clinicopathologic analysis of extracapsular extension in prostate cancer: should the clinical target volume be expanded posterolaterally to account for microscopic extension? *International journal of radiation oncology, biology, physics*, 65(4):999–1007, 7 2006.

[70] David J. Schwartz, Shomik Sengupta, David W. Hillman, Daniel J. Sargent, John C. Cheville, Torrence M. Wilson, Lance A. Mynderse, Richard Choo, and Brian J. Davis. Prediction of Radial Distance of Extraprostatic Extension From Pretherapy Factors. *International Journal of Radiation Oncology Biology Physics*, 69(2):411–418, 2007.

[71] Alan R. Schned, Karlya J. Wheeler, Christine A. Hodorowski, John A. Heaney, Marc S. Ernstoff, Robert J. Amdur, and Robert D. Harris. Tissue-shrinkage correction factor in the calculation of prostate cancer volume. *American Journal of Surgical Pathology*, 1996.